INTERFERENCE-BASED INVESTIGATION OF MICROSCOPIC OBJECTS NEAR SURFACES: A VIEW FROM BELOW

A Dissertation

by

JOSE CLEMENTE CONTRERAS NARANJO

Submitted to the Office of Graduate and Professional Studies of
Texas A&M University
in partial fulfillment of the requirements for the degree of

DOCTOR OF PHILOSOPHY

Chair of Committee,	Victor M. Ugaz
Committee Members,	Zhengdong Cheng
	Carl Laird
	Andreea Trache
Head of Department,	Nazmul M. Karim

December 2013

Major Subject: Chemical Engineering

ABSTRACT

Phenomena occurring when microscopic objects approach planar surfaces are challenging to probe directly because their dynamics cannot be resolved with a sufficiently high spatial/temporal resolution in a non-invasive way, and suitable techniques/methods involve complex instrumentation/computations of limited accessibility/applicability. Interference-based techniques can overcome these barriers. However, because most set-ups and analysis methods are ideal for planar-like geometries, their accurate application for studying microscopic objects has been difficult. Reflection interference contrast microscopy (RICM) has shown particular promise allowing objects in close proximity to a surface to be observed from below, producing interferograms that inherently embed detailed information about the objects' topography near the substrate. Because precise extraction of this information has been challenging, this study seeks to develop analysis methods applicable to RICM to facilitate its practical implementation for accurate investigation of interfacial phenomena between microscopic objects and surfaces.

The most sophisticated theory of RICM was significantly improved and coupled with a general method to simulate the interference pattern from arbitrary convex geometries. Experimental results revealed that accurate reconstruction of an object's contour is possible by fitting its interferogram; however, this is computationally intensive and of limited applicability, motivating the formulation of a simplified and accurate RICM model. This facilitated a major breakthrough: an innovative analysis of RICM interferograms provides the inclination angles of the geometry under study and a mathematical procedure allows near-instantaneous reconstruction of the contour with nanometer-scale resolution, applicable to arbitrarily shaped convex objects under different experimental conditions.

A method for extracting nanometer-scale topographic information from RICM interferograms has been proposed; in particular, microspheres can be conveniently analyzed to measure surface roughness based on fringe visibility. Also, precise and accurate measurements of microspheres' size were performed by means of optimized and robust fringe spacing analysis. Finally, RICM's distinctive "view-from-below" perspective was applied in simple experiments involving the deposition of microspheres on surfaces, directly revealing the existence of different scenarios depending on deposition media and unique femtoliter-scale capillary condensation dynamics underneath micron-sized glass beads. Results show that RICM has a clear potential for

near real-time analysis of ensembles of objects near surfaces so that statistical/probabilistic behavior can be realistically captured.

DEDICATION

To my parents and my brother

ACKNOWLEDGEMENTS

I would like to express my gratitude and appreciation to my advisor and committee chair, Dr. Victor M. Ugaz, for giving me the opportunity of being an active part of his research group, and also for his guidance, patience and encouragement. I would like to thank my committee members, Dr. Zhengdong Cheng, Dr. Carl Laird, and Dr. Andreea Trache, for their time and support.

I would also like to thank my former advisor, Dr. James A. Silas, for introducing me to the world of reflection interference contrast microscopy and the problem of finding "the shape of the vesicle" (as my friends call it). I also thank Dr. Alvaro Ramirez Garcia, my professor in Colombia, who encouraged me to pursue a doctoral degree in Chemical Engineering at Texas A&M University.

I would like to acknowledge that this dissertation was possible thanks to contributions from Jamison Chang, Dr. Yordanos Bisrat, Dr. Asmaa Kassab, Dr. Maria King, and Dr. Yassin Hassan, and financial support from the Texas Engineering Experiment Station and a grant from the US Defense Threat Reduction Agency (DTRA) under project number HDTRA1-10-C-0026.

My gratitude also goes to my friends and current and former lab-mates, all these years would not have been as enjoyable without such great persons from different parts of the world. I also want to thank everyone who directly or indirectly was involved in my career, because they are also part of this achievement.

Finally, I want to deeply thank my parents and my brother, for their love, encouragement, understanding, patience, company, and support. None of this would have been possible without my family and God; He provided me and my family with health during these years away from home and strength during difficult times.

NOMENCLATURE

AFM	Atomic force microscopy
BSA	Bovine serum albumin
CCD	Charged-coupled device
CV	Coefficient of variation
D	Microsphere diameter
$\mathbf{E}$	Local electric field at a position under consideration
$\mathbf{G}$	Map between spherical coordinates
I	Intensity at a position under consideration
I_0	Intensity of a ray directly coming from the illumination source
I_x	Intensity of a ray x collected by the objective
$\mathbf{I_x}$	Vector quantity representing a light beam x
INA	Illumination numerical aperture
J	Jacobian of a change of variables
L	Thickness
LX	Layer X
NA	Numerical aperture
NaCl	Sodium chloride
NIST	National Institute for Standards and Technology
NRL	Normal reflected light
n_x	Refractive index of x
ODE	Ordinary differential equation
OPLD	Optical path length difference
PBd	Polyebutadiene
PBS	Phosphate buffered saline
PDF	Probability distribution function
PEO	Polyethylene oxide
PSL	Polystyrene latex
R	Effective reflection coefficient
R^{sphere}	Radius from spherical fitting

R^{local}	Local radius of curvature
RoR	Radius of rotation
RICM	Reflection interference contrast microscopy
s, *p*	Indicate polarization of light
S	Surface profile of an object
S_0	Minimum separation distance between an object and the substrate
S_0^{sphere}	Minimum separation distance from spherical fitting
*S**	Phase shift height for multi-layer systems
SEM	Scanning electron microscopy
SRM	Standard Reference Material
x, *y*	Position coordinates at the glass-layer 1 interface
Z	Nanometer-scale variations in a surface profile
α_{DA}	Maximum detection angle as measured on glass
α_{IA}	Illumination angle as measured on glass
α_{TIR}	Total internal reflection angle as measured on glass
β	Inclination angle relative to the horizontal plane
β^*	Cutoff inclination angle
δ	Phase shift
δ_C	Empirical correction term
ΔS^{P}	Planar parallel interfaces height increment
$\Delta S^{\text{P}}_{\text{f}}$	Planar parallel interfaces height increment between adjacent fringes
Δx_{f}	Fringe spacing
λ	Wavelength of monochromatic light
Ω	Solid angle
θ, ϕ	Spherical coordinates denoting angles of incidence at a given position
θ_{R}	Angle of reflection
ρ	Radius of curvature
σ	Standard deviation of surface heights or root-mean-square roughness
υ	Visibility
$\langle \text{X} \rangle$	Ensemble average of X

TABLE OF CONTENTS

Page

Page

LIST OF FIGURES

CHAPTER I
INTRODUCTION

1.1 Background and motivation

When a microscopic object approaches a planar substrate, a series of different phenomena might occur (for example, contact, electrostatic repulsion, lateral diffusion, deformation, adhesion, spreading, etc.) depending on the surrounding medium, the nature of their surfaces and interactions, and the presence of external forces. But these phenomena are challenging to probe directly because their dynamics cannot be resolved with a sufficiently high spatial and temporal resolution in a non-invasive way, and the techniques and analysis methods capable of providing accurate quantitative information involve complex instrumentation/computations of limited accessibility/applicability[1-13]. These are even more significant constraints when hundreds of measurements are required for proper statistical characterization of the phenomena under study. Therefore, the implementation of relatively simple techniques and analysis methods capable of providing fast and accurate measurements offers a significant advantage.

Interference-based techniques are known for their set-up simplicity and practical use while offering up to angstrom/microsecond-scale resolution[14-16]. However, the accurate use of interference for the study of microscopic objects has been difficult to achieve because most set-ups and analysis methods are ideal for planar-like geometries[14,17-20]. An experimental set-up that has shown particular promise involves illuminating an object in close proximity to a transparent surface from below using monochromatic light. Interference of light reflected back from different optical interfaces in the system directly reveals the existence of contact phenomena, if any, while the characteristic fringe pattern that emerges inherently embeds detailed information about the object's shape near the substrate at up to microsecond temporal resolution[15]. A particular technique with this characteristic configuration is reflection interference contrast microscopy, RICM, extensively applied in the study of particle, cell, and lipid/polymer vesicle adhesion[21-28].

Although the direct observation and quantification of adhesion phenomena is a well-known capability of RICM, additional information embedded in experimentally obtained interferograms has not been properly exploited because of the lack of appropriate analysis methods. First, fringe spacing in the interference patterns is known to contain precise contour information about the

object under study; however, current applications of RICM focus on analysis of known geometries and sizes using sophisticated models of image formation[29-31], or greatly simplified fringe spacing analysis when the geometry of the object is unknown[24,32-36]. But this simplicity is achieved at the expense of surface profile reconstruction accuracy, particularly when applied to curved microscopic objects, because these methods are strictly valid only for the case of planar parallel interfaces. Second, interference-based measurements have been shown to be sensitive to surface roughness, in particular the visibility of the interference fringes[37]. However, in the context of RICM, relationships between fringe visibility and nanometer scale topography have not been determined.

Therefore, the main efforts of the present work are aimed at improving existing and formulating new methods for accurate quantitative analysis of, in general, arbitrarily shaped convex objects at the microscopic level, see Fig. 1.1, enhancing/facilitating the applicability of RICM in diverse areas. For instance, in contact mechanics applications, RICM observation provides a direct quantification of the contact area, so it has already been implemented to study the deformation of soft particles using conventional deformation models[38]. In this case, an improved analysis offers further verification of the model used (thanks to the nanometer resolution that can be achieved in the accurate shape reconstruction of the deformed microscopic bead) and, as it is pointed out later, the effect of important factors such as deposition medium and capillary condensation can be considered. However, most importantly is the fact that novel systems with tunable mechanical properties (for example, polymer vesicles and other biomimetic systems) have required the recent development of theoretical models for characterization of their deformation behavior[39]. Therefore, the unique non-invasive "view-from-below" perspective and high-resolution capabilities of RICM can play a significant role in the experimental validation of new models, especially when used in combination with other techniques such as atomic force microscopy (AFM)[40].

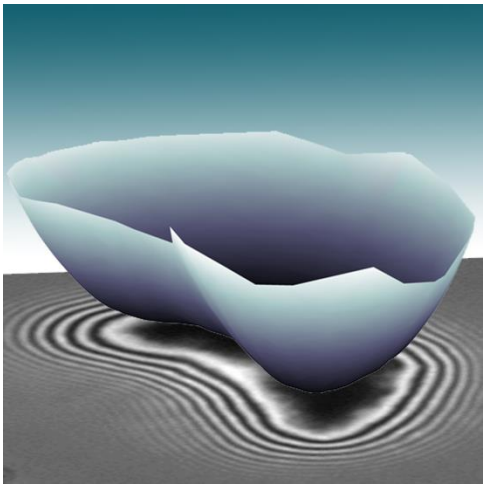

Figure 1.1. Reconstruction of a microscopic arbitrarily shaped convex object by RICM. The system corresponds to a polymer vesicle next to a glass substrate; for details see Chapter IV.

1.2 Research objectives, novelty and significance

This study seeks to develop analysis methods applicable to the RICM technique to facilitate its practical implementation for accurate investigation of interfacial phenomena between microscopic objects and surfaces. The specific aims were:

- Improve the complete non-planar RICM image formation theory by formulating a more precise and general mathematical model for intensity computations.
- Develop a general method to simulate the interference pattern from arbitrary convex geometries with either single or double reflecting layers.
- Formulate a simplified non-planar RICM model by identifying key parameters that precisely capture the behavior observed in experiments and simulations.
- Develop a nanometer-scale resolution method to provide a fast and accurate reconstruction of an arbitrary convex object's contour next to a bounding surface.
- Demonstrate RICM capabilities in non-traditional fields by using its unique view-from-below perspective to directly observe previously unseen contact phenomena.
- Determine relationships between surface roughness of microscopic objects in contact with a substrate and measurable parameters from RICM interference patterns.
- Perform accurate measurements of microspheres' size by optimizing fringe spacing analysis for spherical geometries.

In order to maximize well-known RICM capabilities for surface profile reconstruction, an arbitrarily shaped convex geometry model is considered for the first time, which relaxes assumptions about the configuration of the reflecting surface (typically approximated as wedges or spheres in accurate analysis) while offering exact representation of diverse contours and possible experimental situations. To fully exploit this idea, computational methods based on the most complete theory of RICM are specifically developed for arbitrary convex geometries guaranteeing the best possible simulations of RICM interferograms. At the same time, this provides a valuable tool for the identification of key RICM parameters needed for the formulation of a simplified non-planar model of RICM applicable to all possible conditions where interference occurs in a convex geometry, in contrast with commonly used simple models that are strictly valid for planar parallel interfaces and/or small illumination numerical apertures. As a result, this approach seeks to address the current trade-off between accuracy and generality of the reflecting surface: first, by demonstrating that an accurate reconstruction of an arbitrary convex geometry is possible by fitting its experimental interferogram using the complete theory of RICM; and second, by enabling the development of an innovative analysis of RICM interferograms for fast surface profile reconstruction of arbitrarily shaped convex objects with nanometer-scale resolution.

Here RICM is applied in non-traditional fields with the aim of obtaining valuable new information in the context of particle deposition and resuspension from surfaces, thanks to RICM's high resolution, set-up simplicity and unique non-invasive "view-from-below" perspective. In addition, a novel RICM application for measuring the surface roughness of solid microspheres from fringe visibility analysis is investigated; using a theoretical framework and computational methods, a relationship between these variables is specifically determined for the RICM set-up. This quantitative analysis of intensities is also possible thanks to advancements in protocols to properly compare simulated and experimental intensities.

Novel methods for analysis of RICM interferograms from microscopic curved objects provide greatly enhanced capabilities for the study of their interaction behavior with surfaces. This research is significant because the type of systems suitable for RICM quantitative analysis are of paramount relevance in areas that include contact mechanics; material characterization; biomedicine; immunology; colloid, aerosol, surface, and interface science. Emphasis is made in developing analysis methods of practical implementation that potentially enable accurate real time analysis of dynamic phenomena and/or studies of ensemble of objects that reveal their

statistical/probabilistic behavior. In addition, the insights from the present work represent important progress towards simplified formulations and better understanding of the reflection-interference phenomenon in more complex systems and geometries.

1.3 Reflection interference contrast microscopy

In 1964, the study of the mechanism of cell adhesion to glass by Curtis[41] constituted the first application of the interference reflection microscopy technique; Ploem[42], in 1975, improved the method by the development of reflection contrast, and due to the work of Gingell, Todd and Heavens[43,44], in 1979 and 1982, RICM became a quantitative technique to determine cell-substrate separation. In the past decades, more experimental and theoretical improvements have been achieved[29,45-47], showing that this is an area which undergoes continuous development. A recent review by Limozin and Sengupta has provided a useful tool for understanding diverse aspects of RICM going from the set-up to applications in soft matter and cell adhesion[48].

1.3.1 RICM set-up

In the present work, a standard RICM experimental set-up was used as described in the following and presented in Fig. 1.2. It consists of an inverted microscope that facilitates the observation from below samples that can be simply deposited on a cover glass in air, or samples that, provided a density difference in solution, naturally sediment to the bottom thanks to gravity. The light source is coherent and has been manually aligned; an interference filter in the light path allows obtaining green monochromatic light of wavelength λ. Next, two aperture diaphragms facilitate controlling the illumination cone and field of view on the sample and their positioning with respect to the sample and objective enable Köhler illumination[48]. Then, components are in place to introduce a series of light polarization changes corresponding to the antiflex technique[29,42]. First, a polarizer generates linearly polarized light that is transformed to circular polarized light by the $\lambda/4$ plate located inside the objective; second, light reflected back from the sample passes the quarter-wave plate for a second time so it goes from circular to linear polarization but it has a phase shift of 90°; and third, the polarization direction of the analyzer guaranties that only light from outside the microscope is collected by the camera, suppressing stray light resulting from internal reflections that would obscure RICM images. More specific

information about the main components of the set-up and parameters used can be found in Chapter II.

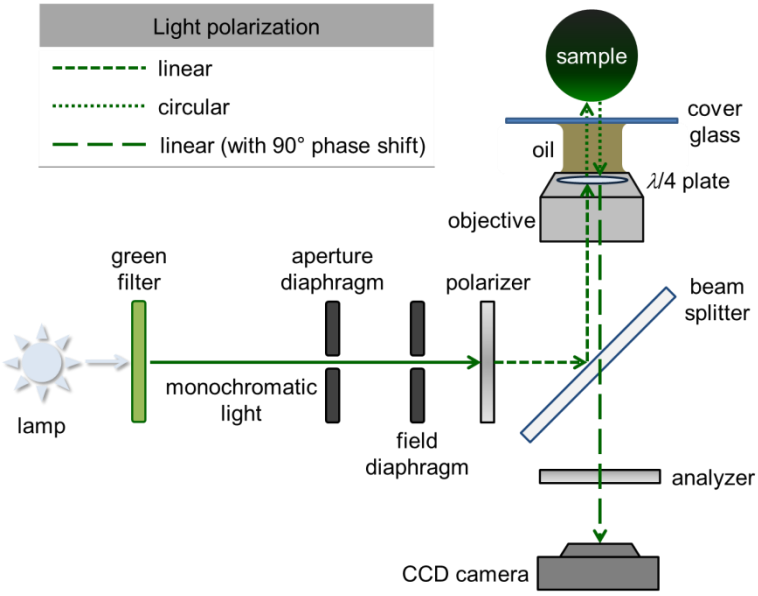

Figure 1.2. RICM experimental set-up and optical path. Schematic representation of the main components involved including light polarization.

1.3.2 Image formation theories of RICM

Across the years, different theoretical models of various degrees of complexity have been formulated to describe the RICM image formation process. In the simple theory, the illumination cone has a zero aperture angle and the interfaces from which reflections occur are approximated as parallel to the glass substrate (that is, the curvature of the object is neglected); as a result, only incident and reflected light beams parallel to the optical axis are taken into account and the intensity becomes an algebraic function of height[45,49]. The finite aperture theory differs from the simple theory in that it considers the effect of a finite aperture angle of illumination; therefore, its mathematical form is that of an integral or summation over angles in space[43,44]. An analytical solution for this formulation can be obtained after assuming a rectangular illumination profile and neglecting the angular dependence of the reflection coefficients, providing an important improvement with respect to the simple theory[45]. In addition, the finite aperture theory was

recently enhanced to include polarization effects, shown to be relevant when high illumination numerical apertures were used[46].

A better approach was the non-local theory, which takes into account the finite aperture angle of illumination and detection and the effect of curved interfaces; however, it still presents some deviations with respect to the experimental data due to assumptions, such as the non-angle dependence of the reflection coefficients, intended to simplify the complex calculations[50]. Finally, the non-planar interface image formation theory of RICM incorporated the basic ideas of the non-local theory but offered a more refined approach with less simplifications and a systematic way of evaluating the intensity contributions in three dimensions[29]. This formulation was carefully reviewed and improved in the present work, see Chapter III.

1.3.3 RICM and surface profile reconstruction applications

The simple theory of RICM image formation is commonly used to obtain a fast and approximated reconstruction of the surface profile in single- and double-layer systems. From this theory, it can be shown that the intensity is a cosine transform of the local height; therefore, the contour can be obtained by inverse cosine transform once the maximum and minimum intensities in the interference pattern have been determined[45,49]. For double-layer systems, an additional phase-shift factor has to be considered, in a slightly modified approach called the refractive index method[48,51]. The non-local theory has been used in the context of spherical particles for determining their separation distance with the substrate[50], and based on the non-planar theory an explicit single-layer model for the geometries of wedges and spheres was published by Sackmann, including correction factors from these known geometries to improve the calculation of inclination angles and radii of curvature[29]. Surface profiles of various systems have also been obtained using correction factors based on non-planar theory[52] and calibration methods[53]. However, to the best of our knowledge, neither has there been an attempt to calculate accurate intensity patterns from arbitrary convex geometries with single and double reflecting layers, nor to reconstruct this type of surface profiles by using the complete non-planar interface image formation theory, as done here in Chapter III.

Traditionally, RICM has been used to study the adhesion of cells and lipid vesicles, where the reconstructed contour by inverse cosine transform is used to get geometric parameters that allow adhesion strength calculation[24,32-34]. The recent use of versatile materials such as amphiphilic block copolymers that self-assemble in aqueous solutions forming vesicles[54,55] (one

of our experimental systems of study), opens the possibility of using accurate surface profile reconstruction by RICM to analyze their adhesion properties, something mainly done by micropipette aspiration technique[56-58]. Another potential application is the study of the behavior of polymer vesicles close to a wall under shear flow, which will make possible the determination of desirable mechanical properties for the vesicles in vascular flow. Some experimental studies in giant lipid vesicles under shear flow have been performed using side view[59] and side view combined with RICM[60], and also theoretical approaches to the problem have been done[61,62]. Leukocyte adhesion to endothelium, the natural model for this system, has been analyzed using microspheres[63] and simulation techniques[64]. However, these dynamic phenomena require the implementation of fast and accurate methods, where the computationally intensive non-planar theory represents an important limitation. Therefore, these issues are addressed in Chapter IV with the formulation of a simplified non-planar model of RICM and the development of a near-instantaneous surface profile reconstruction method with nanometer-scale resolution.

1.3.4 Direct observation of contact phenomena by RICM

This represents the most exploited capability of RICM thanks to its unique "view-from-below" perspective and the simplicity of the analysis required; as mentioned earlier, it has been extensively applied in the study of particle, cell, and lipid/polymer vesicle adhesion[21-28]. In recent years, this exceptional capability has been used in immunology applications where RICM proved useful in describing a variant of a leukocyte adhesion deficiency type III[65] and in the formulation of immunology methods for quantifying lymphocyte activation[66]. More fundamental studies of cell adhesion on adhesive surfaces have also been performed[67] and other effects such as cell membrane undulations or "roughness" have been monitored[23,68-70], further demonstrating RICM capabilities in the characterization of the adhesion phenomena of blood cells on surfaces. In addition, RICM was recently used in pancreatic cancer studies intended to establish a possible gene expression role in processes required for metastasis[71]. Although these are exciting RICM applications they still follow the traditional line established decades earlier in cell adhesion studies. In contrast, in Chapter IV we have demonstrated the importance of RICM distinctive capabilities for the direct observation of different deposition scenarios of microspheres on surfaces and femtoliter-scale capillary condensation dynamics underneath micron-sized glass beads (believed to be unique). Both of these findings are in the context of particle deposition and resuspension from surfaces.

1.3.5 RICM measurements on microspheres

The spherical geometry has been widely used in experiments involving RICM, both as an experimental system and as a geometric model to extract useful information. Typically, the separation between the particle and the substrate is measured[30,31,50] while taking advantage of the concentric and symmetric interferogram to determine its center with sub-pixel resolution, thus offering a three-dimensional tracking tool[30,72]. This implies that the microsphere is assumed to be perfectly spherical, even down to the nanometer scale, although experimental evidence indicates otherwise, typically in the form of a finite separation distance with the substrate when in physical contact[40]. However, the only known direct attempt to quantify roughness using RICM has been in the measurement of cell membrane undulations[23,68-70]. Chapter V presents a novel effort to measure nanometer-scale surface variations on microspheres using relationships specifically derived for the RICM set-up.

RICM capabilities for particle size measurements have long been appreciated, in particular using analysis of limited applicability[40,48] and with more practical measurements only possible by means of correction factors derived from full non-planar RICM[29]. The method presented in Chapter V is quite robust and easy to implement because it is based on a direct and optimized analysis of multiple interference fringes, resulting in relative errors less than 1% for microspheres with diameters between 7 to 60 μm. This accuracy is comparable to measurements from scanning electron microscopy (SEM) and significantly better than those from conventional optical microscopy (relative error $\geq$ 10%)[73,74].

Microspheres also play an important role when RICM is used in combination with other experimental techniques. For instance, when colloidal beads are used as force probes, the reconstruction of the bead/surface interaction potential is possible if the height distribution functions of the fluctuating beads can be measured. In this case, RICM can be used either as an optical "passive" technique to observe the Brownian motion of the spherical particle close to the wall[30,50,75,76] or combined with optical tweezers to control the position of the bead[77,78]. Even more significant is the relevance of microspheres in the colloidal probe technique[21,40], where RICM and atomic force microscopy are combined for accurate measurements of force interactions that require determination of size, local curvature and roughness of the microsphere acting as a probe, all of these measurements considered in Chapter V using RICM.

CHAPTER II
METHODS

2.1 Image acquisition

The microscope set-up employed in our experiments was a Zeiss Axiovert 200M Inverted microscope. Monochromatic green light, 546.1 nm, was obtained from a 103W HBO mercury lamp using a 5 nm band-pass filter. The microscope was equipped with a Zeiss Antiflex EC Plan-Neofluar 63x/1.25 Oil Ph3 objective and images were recorded with a Zeiss AxioCam MRm camera. Scanning electron microscopy (SEM) images were taken by Dr. Yordanos Bisrat at the Materials Characterization Facility at Texas A&M University using an ultra-high resolution field emission scanning electron microscope (FE-SEM), the JEOL JSM-7500F. A 5 nm coating of platinum/palladium was applied on the sample when necessary for SEM observation.

2.2 Sample selection and preparation

The experimental systems chosen in the present work are microscopic objects, such as polymer vesicles, polystyrene latex (PSL) and glass particles, close to a glass substrate. There are several reasons for this sample choice. First, these systems typically adopt an overall spherical shape (as determined from bright field, the circular symmetry in the RICM images and SEM observation) covering a wide range of sizes in the micrometer scale where curvature effects become important in the interference pattern to be analyzed. Polymer vesicles, especially when non-symmetric RICM images are observed, also offer the possibility of studying arbitrary convex geometries. The second one is the objects' geometry at their bottom. Polymer vesicles (which are perfectly spherical when free in solution) are expected to experience deformation when close to or in contact with a planar surface. Glass and PSL microspheres, although hard to deform despite being in contact with the substrate, offer other interesting effects such as surface roughness, a close look to its assumed spherical shape, and the possibility to directly observe contact phenomena between the particles and the substrate. The third aspect is the objects' surfaces, where the vesicles represent added complexity for RICM analysis because of the presence of the smooth polymer membrane (double-layer system), when compared with glass and PSL surfaces

of different topographies (single-layer systems). Also, PSL particles of uniform surface topography are expected to reveal the effects of strong capillary forces acting during drying. Finally, although the polymer vesicles are in aqueous surroundings, the other microspheres can be studied both in air and aqueous medium, verifying the applicability of the methods of analysis developed under different experimental conditions.

2.2.1 Polymer vesicles

Block copolymer vesicles spontaneously form in water when the copolymer has one hydrophobic and one hydrophilic block, called amphiphilic di-block copolymers.[54,55] Polyethylene oxide-block-polybutadiene (PEO_{89}-PBd_{120}, molecular mass 10,400 g mol^{-1}) purchased from Polymer Source Inc. (Canada) has been used. For vesicle preparation, a polymer film containing 250 μg of the block copolymer is formed by evaporation (8 hours) at the bottom of a 5 mL glass scintillation vial and the film is rehydrated during 24 hours at 60ºC with 1-2 mL of a 300 mOsm kg^{-1} sucrose solution (Osmometer model 3320, Advanced Instruments, Inc., Norwood, MA). To obtain shell polymerized vesicles, the resulting solutions were exposed for 1-3 hours to 200 μL of 20 % ammonium persulfate (99%) and 30 μL of 1,2-bis(dimethylamino)ethane (99%). Then, the vesicles are placed in phosphate buffered saline (PBS) solution of equal osmotic pressure than their interior. Ammonium persulfate and 1,2-bis(dimethylamino)ethane were obtained from Acros Organics (Morris Plains, NJ), whereas PBS and sucrose (ACS reagent) were purchased from Fisher Scientific (Pittsburgh, PA).

A small volume (typically 200 μL) of the previously prepared vesicle solution is placed in a sealed chamber on top of an optical borosilicate cover glass (0.16 to 0.19 mm thickness); a coating of bovine serum albumin (BSA) is applied on the glass surface if adhesion and spreading of the vesicles onto the substrate is not desired. The gravitational force determined by the density difference between the sucrose and PBS solutions pushes the vesicles towards the substrate and allows them to settle, while the BSA coating and possible electrostatic repulsion due to impurity charges on the vesicles and the highly negatively charged glass surface keep them from getting in contact with the substrate[75]. As a result, the vesicles float above the glass surface in a slightly deformed configuration with respect to their spherical shape when they are free in solution.

2.2.2 Microspheres

Diverse samples of microspheres have been considered, both monodisperse and polydisperse, as follows. The Standard Reference Material (SRM) 1961 is a suspension of nominal 30-μm diameter polystyrene spheres in water obtained from the National Institute of Standards and Technology (NIST, USA); SRM 1961 has a certified particle diameter of 29.64 ± 0.06 μm and a Gaussian size distribution with a coefficient of variation (CV) of 0.8%. Monodisperse fluorescent green PSL particles of 15 μm in diameter (14% CV) with a refractive index of 1.59 were manufactured by Thermo Fisher Scientific Inc. (USA), come in powder form and are denoted as PSL15. The 15 μm diameter monodisperse glass beads used in the experiments (Glass15) were provided in powder form by the Aerosol Technology Lab at Texas A&M University. The polydisperse glass beads of 30-50 μm diameter (Glass30-50) were manufactured by Polysciences Inc. (USA), come in powder form, are made of soda lime glass and have a refractive index of 1.51.

Different experimental conditions were considered for the microspheres. SRM 1961 was studied in a diluted solution where the particles are hovering next to the substrate. In dry deposition experiments, Glass30-50 and PSL15 particles were directly placed on top of a cover glass and observed within minutes; Glass30-50 was also monitored during larger time scales (a couple of weeks) where some particles were exposed to ambient conditions while others were kept in sealed chambers and/or vacuum. In wet deposition experiments, Glass30-50 and PSL15 microspheres were directly deposited on the cover glass and a droplet of ultra-pure de-ionized water was added on top of the particles; drying under ambient conditions and vacuum was performed. A medium of 0.1 M NaCl solution was used in experiments where particles are required to be in contact with the glass substrate so that the electrostatic repulsion barrier is overcome.

2.3 RICM experiments and image analysis

Processing of RICM images was performed with the software ImageJ 1.41o (public domain, National Institutes of Health, USA) and MATLAB R2010a, and the experimental and computational procedures implemented to extract quantitative information are described in the following.

2.3.1 Measurement of RICM set-up parameters

Light coming through the objective illuminates the focal area with a cone of light, α_{IA} (as measured on the glass side), given by the size of the aperture stop in the microscope; this determines the illumination numerical aperture (INA) in the set-up by means of the relationship INA = $n_{glass}\sin(\alpha_{IA})$. Here, α_{IA} measurements are based on the determination of the normalized irradiance profile, $I_0(\theta)/I_{0max}$, for a given aperture, according to the description by Gingell and Todd[43], see Fig. 2.1. When the aperture stop is increased up to the point where no changes are observed, a maximum INA of 1.25 is reached that actually corresponds to the numerical aperture (NA) of the objective. At this maximum, $I_0(\theta)/I_{0max}$ closely follows the cosine-fourth law of illumination up to 0.5 radians, with a drop in the intensity observed between 0.24 and 0.45 radians due to the presence of a phase plate inside the objective. The profile for the minimum aperture available, 0.74 mm diameter, breaks away from the INA_{max} curve and follows a sigmoid which does not instantly drop to zero, making the choice of a specific α_{IA} value somewhat arbitrary but necessary, because its value is a key parameter in simulations and image analysis. All images in the present work were taken using the smallest INA available, estimated to be 0.48 as measured from the value of theta (0.32 radians) where $I_0(\theta)/I_{0max}$ drops to about 2% its maximum, and NA = 1.25 for the objective.

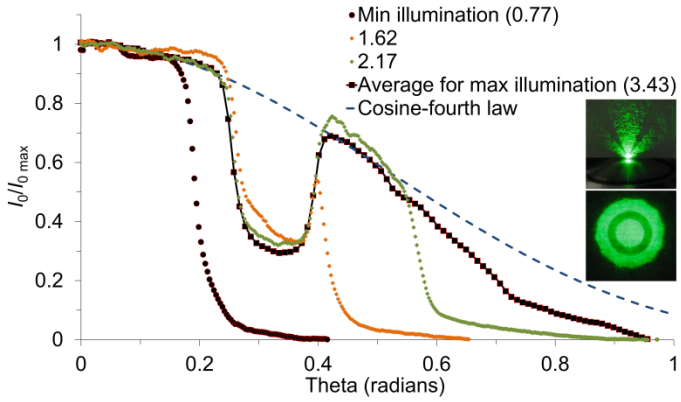

Figure 2.1. Irradiance profiles for different apertures. Normalized irradiance profiles are shown for four different aperture stop diameters (indicated in mm). They are measured from the circular conic section of illumination projected on the surface of a glass block positioned on top of the objective (bottom inset); a radial average is performed over the projection generated, the background is subtracted and the results are normalized by the maximum intensity. The insets correspond to a 2.17 aperture where the top inset shows the illumination cone as seen in air.

2.3.2 Scale factor between simulated and experimental intensities

Prior to observing the specimens under the microscope, a scale factor between experimental and simulated intensities is measured. RICM images of different glass-ambient medium systems of known refractive indices (measured with an Abbe refractometer) are taken about one hour after the ignition of the fluorescence lamp to allow for its complete stabilization, see Fig. 2.2a.

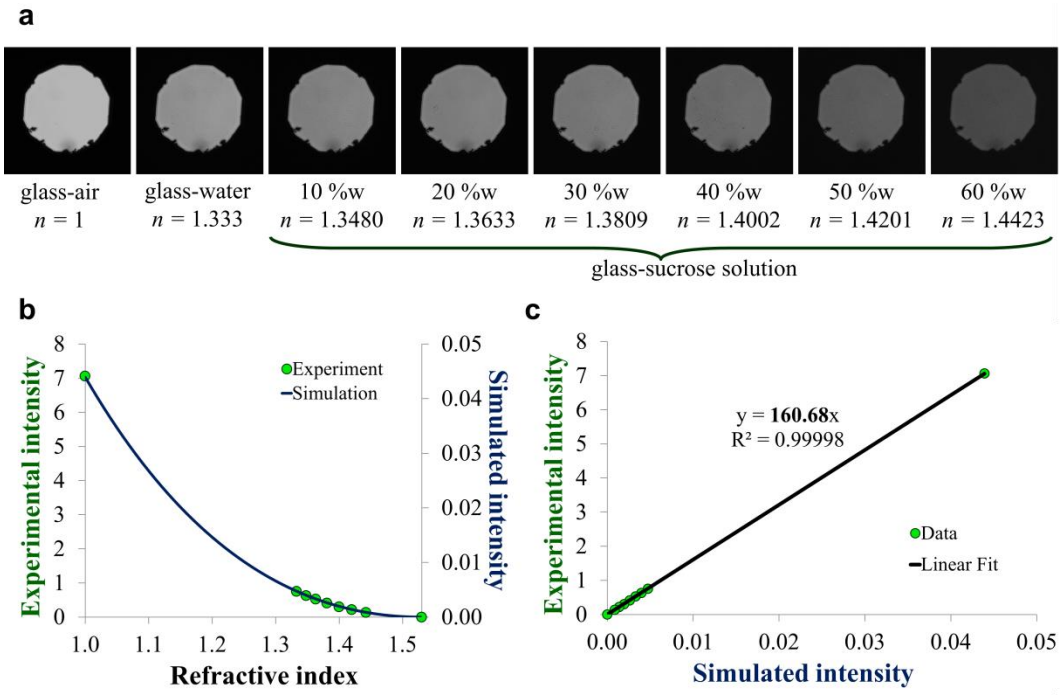

Figure 2.2. Scale factor between simulated and experimental intensities. (**a**) A variety of substrate-ambient medium interfaces are used to obtain different experimental intensities. (**b**) Experimental and the corresponding simulated intensities follow the same functional form when plotted against refractive index. Notice that the "zero" intensity has to be subtracted from the experimental value. (**c**) The scale factor is the slope of the linear correlation between the intensities.

The experimental intensity values are obtained from the measurement of an average intensity (over a selected region inside the field of view) from which a "zero" intensity is subtracted (measured from the dark shadow in the periphery) and the resulting values are normalized by the exposure time (although this normalization can be omitted if all images are taken with the same exposure time). Then, the measured experimental intensities are plotted as a function of the refractive index of the ambient medium. Because the refractive index of all the

components is known, simulations can be performed to get the corresponding simulated intensity showing that they follow the same functional form, as seen in Fig. 2.2b. Actually, in our approach, the refractive index of the cover glass was initially unknown and its value, 1.530, was estimated so that the best linear correlation (going through the origin) between the experimental and simulated intensities is obtained in Fig. 2.2c while the corresponding slope provides the scale factor between them.

The scale factor measured is found to remain fairly constant (~ 1 % variation) during several hours, even if different samples are observed; however, if the illumination is changed or the lamp is turned off, a new scale factor has to be measured. Notice also that once the refractive index of the cover glass is determined, only the construction of the plot in Fig. 2.2c is necessary.

2.3.3 Subtraction of non-uniform background

To accurately analyze intensities in RICM images, an image homogenization procedure is executed. It turns out that the field of view is not uniformly illuminated and this can introduce a significant error in minimum separation distance measurements. Therefore, images of the background, like the one in Fig. 2.3a, can be used to determine the intensity values (Fig. 2.3c) that have to be subtracted from a particular RICM image (Fig. 2.3b) so that its intensity variations due to a non-uniform background are accounted for. For instance, if this background correction is not made, a relative error as large as 28 % in separation distance determination could be obtained when the intensity used in the measurement is located at the brightest spot in Fig. 2.3c.

The procedure implemented is as follows: first, it is recommended to obtain a single background image by averaging and smoothing several glass-ambient medium interface images taken at different places over a clean cover glass while keeping the field of view aperture constant; second, the corresponding "zero" intensities are measured and subtracted from both the background image (Fig. 2.3a) and the image of interest (Fig. 2.3b); third, a selection corresponding to a common background in Fig. 2.3a and Fig. 2.3b is identified, while excluding inner areas containing all interferograms from objects (that is, all interferograms are masked out); fourth, average background intensities measured from the identified common selection are used to scale the background image onto the intensity scale of the image of interest; finally, intensity deviations over the background image with respect to the average background intensity

are computed (Fig. 2.3c) and subtracted from the image of interest. Notice that the procedure does not alter the average background intensity of the image of interest.

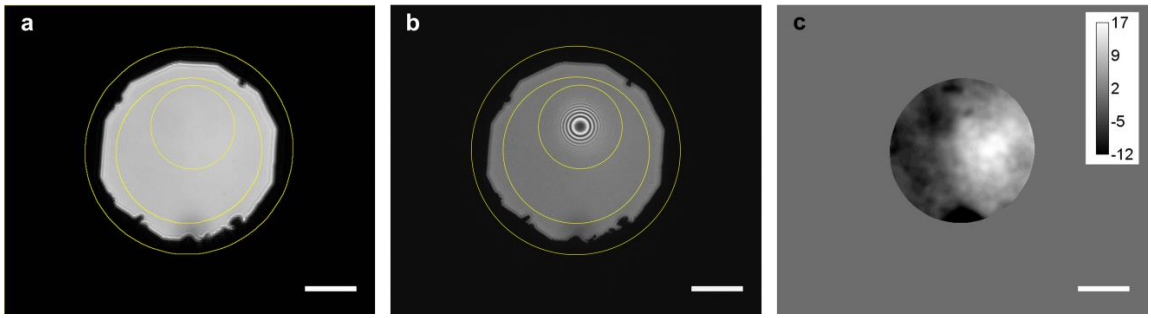

Figure 2.3. Subtraction of non-uniform background. (**a**) RICM image resulting from averaging and smoothing several individual images of glass/air interfaces; it illustrates the regions where the "zero" (outside outer selection) and background (selection inside the field of view) intensities are measured. (**b**) RICM image of a polymer vesicle in aqueous medium before homogenization, with an average background intensity of 355.44; notice that this value is measured within the field of view but masking out the area containing the interferogram corresponding to the polymer vesicle. (**c**) Intensity values to be subtracted from (b) so that irregularities coming from a non-uniform background are accounted for; minimum and maximum intensities of -60.14 and 16.86, respectively, were obtained. 10 μm scale bars.

2.3.4 Intensity profile measurement

After non-uniformities from the background are subtracted, the intensity profile along an observation line or area is measured, followed by a "zero" intensity subtraction (from the dark area outside the field of view), and normalization by the exposure time (if necessary), see Fig. 2.4. Notice that the observation lines are manually selected perpendicular to the fringe's front, so an average intensity profile over an area can be directly measured when dealing with wedge geometries or, if there is circular symmetry in the RICM image, the center of the interferogram is located and a circular average of intensities is obtained; in contrast, only single profiles can be obtained from an arbitrary convex geometry. To accurately determine the center of an interferogram with circular symmetry, a custom made routine is implemented in ImageJ as follows: first, a square selection power of two (128x128, 256x256, etc.) is made around the center and a new image is created; then, background is subtracted with a rolling ball radius of 50 pixels and the resulting image is convolved with itself using the FD Math command (Process>FFT>FD Math); a threshold is set using the relationship (min + (max – min)*0.92,

max) where *min* and *max* are the minimum and maximum intensity values, respectively, of the image obtained after convolution; the resulting image is then converted to binary and the center of mass is computed; finally, the center obtained is averaged with the center of the square image to obtain the center of the interferogram. This procedure provides sub-pixel resolution and has proven highly reliable and robust.

The positions of peaks and valleys (and consequently the fringe spacing and minimum and maximum intensities) are determined from the resulting intensity profile so that subsequent procedures can be performed. To obtain an absolute contour reconstruction and/or to perform fringe visibility analysis, the experimental intensity values are scaled to match the simulated intensity versus height curve from the theory for stratified planar structures, and the minimum separation distance between the specimens and the glass is measured assuming that particles and vesicles are close enough to the glass substrate (minimum separation distance < 200 nm).

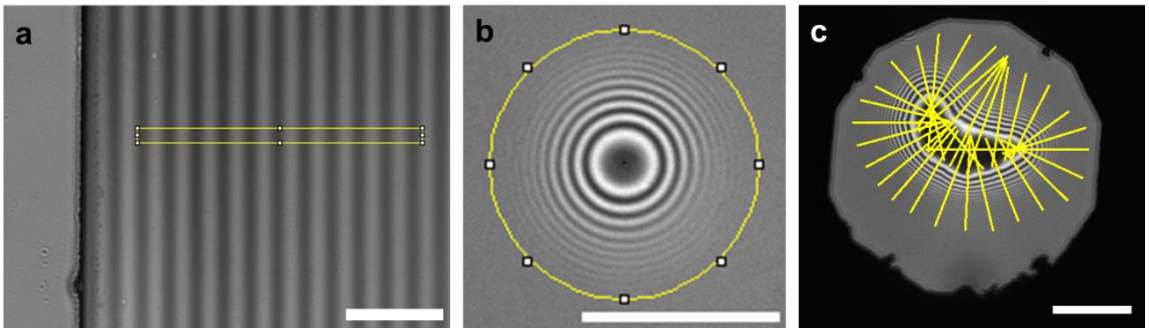

Figure 2.4. Intensity profiles in representative interferograms. (**a**) Interference fringes from a wedge geometry. (**b**) Concentric and symmetric fringes from a sphere-like geometry; center pixel is set to black. (**c**) Concentric and non-symmetric fringes from an arbitrarily shaped convex geometry. 10 μm scale bars.

CHAPTER III
REFLECTION INTERFERENCE CONTRAST MICROSCOPY OF ARBITRARY CONVEX SURFACES*

3.1 Overview

Current accurate applications of reflection interference contrast microscopy (RICM) are limited to known geometries; when the geometry of the object is unknown, an approximated fringe spacing analysis is usually performed. To complete an accurate RICM analysis in more general situations, we review and improve the formulation for intensity calculation based on non-planar interface image formation theory, and develop a method for its practical implementation in wedges and convex surfaces. In addition, a suitable RICM model for an arbitrary convex surface, with or without a uniform layer such as a membrane or ultrathin coating, is presented. Experimental work with polymer vesicles shows that the coupling of the improved RICM image formation theory, the calculation method, and the surface model allow an accurate reconstruction of the convex bottom shape of an object close to the substrate by fitting its experimental intensity pattern.

3.2 Introduction

An image formed by reflection interference contrast microscopy, RICM, contains precise information about the topography of the object under observation. Current applications of RICM are focused on analysis of experimental interference patterns from known geometries and sizes using sophisticated models of image formation[29-31], or greatly simplified fringe spacing analysis when the geometry of the object is unknown[24,32-36]. For instance, simultaneous determination of the three-dimensional (3D) positions of multiple spherical particles can be performed by direct comparison with simulated interferograms from spheres[30]. On the other hand, RICM adhesion studies of cells and lipid vesicles, where the geometry is unknown, usually involve determining their approximated contour near the contact region by inverse cosine transform[24,32-34]. However, if a sophisticated RICM image formation model could be applied to simulate intensity patterns

* Reprinted with permission from "Reflection interference contrast microscopy of arbitrary convex surfaces" by Jose C. Contreras-Naranjo, James A. Silas, and Victor M. Ugaz, 2010, Applied Optics 49: 3701-3712, Copyright 2010, The Optical Society (OSA)

from arbitrary geometries so that they could be directly compared with experimental interferograms, it would be possible to extract much more accurate information from RICM images (for example, object shape, separation distance, and membrane thickness, etc.).

In the present research we focus on geometries with an arbitrary convex surface with or without a uniform second layer such as an ultrathin coating or a membrane because these systems are important in a number of applications. In addition to cells and lipid vesicles, the polymer vesicles employed here come from the novel use of versatile materials such as amphiphilic block copolymers that self-assemble in aqueous solutions and are important in the design of drug delivery systems, biosensors and cell mimicry[54,79-81]. Another type of system that can be studied includes ultrathin polyelectrolyte multilayer films adsorbed onto micrometer-size colloidal particles. Following the removal of the particle template, these systems provide tailored hollow capsules suitable for diverse applications[82,83]. More generally speaking, an accurate RICM analysis fits extraordinarily well in understanding the deformation behavior of soft particles near a flat substrate, which is of paramount importance for the progress in colloid and interface science[39].

Since the first RICM theoretical considerations by Gingell and Todd in 1979[43], important theoretical improvements have been accomplished thanks to the work of Sackmann and co-workers during the 1990s[29,45,50]. The non-planar interface image formation theory[29], introduced in 1998, represents the most sophisticated theory yet. This paper presents a review and improvement of this theory, with the formulation of a general statement for intensity calculations and a correction in terms of the optical path length difference (*OPLD*) determination in non-planar interfaces. A method for the practical implementation of the improved theory in wedges and convex surfaces is presented, based on an approximated formulation that directly uses the convenient backward ray-tracing technique. Also, a general model for an arbitrary convex surface, with or without a uniform layer such as a membrane or ultrathin coating, is presented. In order to speed up the calculations without losing accuracy, the appropriate geometric simplifications in the model are studied using simulations. As a result, the experimental data demonstrate the validity of the improved theory, the calculation method employed in the simulations, and the developed surface model when used together to accurately obtain the surface profile of a polymer vesicle by fitting its experimental intensity pattern.

3.3 Results

3.3.1 RICM image formation theory improvement

RICM image formation is illustrated in Fig. 3.1a, followed by the description of the non-planar interface image formation theory[29] in Fig. 3.1b, which is the most sophisticated to date. According to this theory, the contributions to the intensity at $B(x, y)$ are integrated incoherently as follows:

$$I(x,y)=\left\langle \frac{\int \mathbf{E}*\mathbf{E}\,\mathrm{d}\Omega}{\int \mathrm{d}\Omega} \right\rangle_t \tag{3.1}$$

Where **E** is the local electric field, $\Omega = (\theta, \phi)$ are spherical coordinates denoting angles of incidence at B, and t stands for a time average. The integral in equation (3.1) has been rewritten as

$$I(x,y)=I^s+I^p \tag{3.2}$$

$$I^{s,p}=\frac{(I_0/2)\int_0^{2\pi}\int_0^{\alpha_{\mathrm{DA}}}\left[R^{s,p}(\theta,\phi)*R^{s,p}(\theta,\phi)\right]\sin(\theta)\mathrm{d}\theta\mathrm{d}\phi}{\int_0^{2\pi}\int_0^{\alpha_{\mathrm{IA}}}\sin(\theta)\mathrm{d}\theta\mathrm{d}\phi} \tag{3.3}$$

considering that *s*-polarized light cannot interfere with *p*-polarized light and vice versa; recently, polarization effects have been included in a planar model showing that they become relevant when a high illumination numerical aperture, INA, is used[46]. R is the effective reflection coefficient which is a function of the geometry, refractive indices, and constraints in the system; and I_0 is the intensity of the incident light supposed to be homogeneous in θ, in the interval [0, α_{IA}]. According to this formulation, the integration variables (θ, ϕ) correspond to (θ_2, ϕ_2) in Fig. 3.1b because they are indexing all rays incident at B that reenter the microscope after reflection at the non-planar interface.

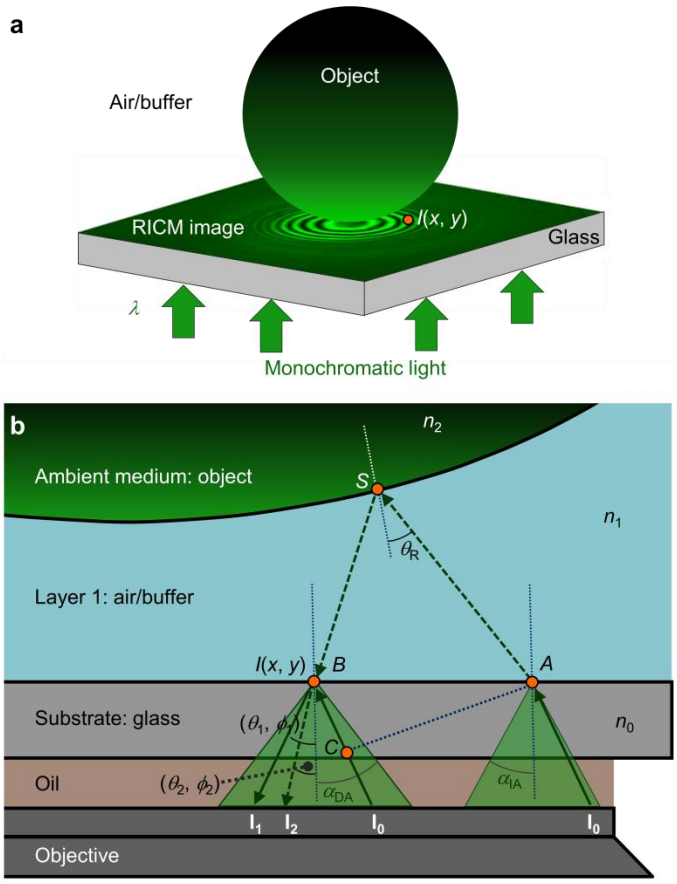

Figure 3.1. RICM overview and non-planar model in a single-layer system. (**a**) RICM image formed due to the interference of rays reflected from different optical interfaces in the system when the object is illuminated from below using monochromatic light. (**b**) The illumination source is considered monochromatic, pseudo-coherent, and angularly limited by the illumination numerical aperture (INA) of the microscope, which means all $\mathbf{I_0}$ originate from within the cone defined by the maximum illumination angle, α_{IA}. The normalized intensity at B in the image plane, $I(x, y)$, is calculated integrating over spherical coordinates (θ_2, ϕ_2) the contributions from rays $\mathbf{I_1}$ and $\mathbf{I_2}$ incident within the cone of detected light, α_{DA}, determined by the numerical aperture (NA) of the objective. The path length and intensity corresponding to each particular ray are determined by backward ray-tracing, taking into account reflection and transmission at every optical interface corresponding to a given geometry; however, multiple reflections are not considered.

This formulation correctly describes a situation such as the one depicted in Fig. 3.1b with two identical beams, $\mathbf{I_0}$, originating from the homogeneous illumination source, and $\mathbf{I_2}$ as the only ray incident at $B(x, y)$ after reflection at the non-planar interface, which gives a single possibility for defining the integration variables (θ, ϕ) as (θ_2, ϕ_2). However, if we think about a more complex situation where more than two complementary rays, $\mathbf{I_0}$, interfere, the use of a

consistent indexing (θ, ϕ), based on rays that are reflected back from the object, becomes more difficult and even impossible. This is due to the fact that, after reflection at the non-planar interface, each complementary $\boldsymbol{I_0}$ results in different contributions $\mathbf{I_2}$, $\mathbf{I_3}$,… and each one of them is more likely to have a different orientation (θ_2, ϕ_2), (θ_3, ϕ_3),... when incident at *B*. Another issue with the (θ_2, ϕ_2) indexing is that in some situations we may not be able to account for all $\mathbf{I_1}$ contributions to the intensity because the existence of $\mathbf{I_1}$ is determined by the existence of $\mathbf{I_2}$, and this depends on the geometry and constraints in the system. Because (θ_2, ϕ_2) are not general variables for integration in equations (3.1), (3.2), and (3.3), we instead consider the $\mathbf{I_1}$ angles (θ_1, ϕ_1), shown in Fig. 3.1b, as quantities capable of providing a basis for consistent indexing in any situation. These variables are unique because no other complementary $\mathbf{I_0}$ is reflected off the substrate-layer 1 interface and they exist whenever there are contributions to the intensity.

Based on these considerations, we express the local intensity, $I(x, y)$ at the image point *B*, located at the substrate-layer 1 interface, in terms of:

$$I(x,y) = \left\langle \frac{\int_{\Omega_1} \mathbf{E} * \mathbf{E}\, \mathrm{d}\Omega}{\int_{\Omega_1} \mathrm{d}\Omega} \right\rangle_t = I^s + I^p \tag{3.4}$$

$$I^{s,p} = \frac{\int_0^{2\pi} \int_0^{\alpha_{1A}} \left[R^{s,p}(\theta_1,\phi_1) * R^{s,p}(\theta_1,\phi_1)\right]\left[I_0(\theta_1)/2\right]\sin(\theta_1)\mathrm{d}\theta_1\mathrm{d}\phi_1}{\int_0^{2\pi} \int_0^{\alpha_{1A}} \sin(\theta_1)\mathrm{d}\theta_1\mathrm{d}\phi_1} \tag{3.5}$$

Here the average over solid angle of the contributions to the intensity is done by indexing the integration following $\mathbf{I_1}$, with orientation (θ_1, ϕ_1) as shown in Fig. 3.1b, and its interference with the corresponding contributions $\mathbf{I_2}$, $\mathbf{I_3}$, … if any, from complementary rays $\mathbf{I_0}$. This defines a two-dimensional (2D) set of angles in the $\theta_1\phi_1$-plane, Ω_1, corresponding to the solid angle where all contributions to the intensity reside (the differential element of solid angle is given by $\mathrm{d}\Omega = \sin(\theta_1)\mathrm{d}\theta_1\mathrm{d}\phi_1$). It can be seen that the denominator of equations (3.4) and (3.5) is a normalization constant directly related to Ω_1. Once the INA of the microscope is set to a certain value, the extended illumination source, $I_0(\theta_1)$, becomes geometrically constrained within the illumination

cone defined by α_{1A}. Consequently, the solid angle over which contributions to the intensity are collected, Ω_1, is set by $\theta_{1\,max} = \alpha_{1A}$, the only parameter that is necessary to obtain the normalization term. On the other hand, we see that the numerator can be calculated, unambiguously and at least in theory, by tracking all beams $\mathbf{I_1}$ within Ω_1 and finding all complementary rays $\mathbf{I_0}$ and their contributions $\mathbf{I_2}$, $\mathbf{I_3}$,… that satisfy the constraints in the system and combine to produce interference. However, the intensity calculation becomes more challenging in this new scenario because instead of using the convenient backward ray-tracing method based on (θ_2, ϕ_2) we have to start with (θ_1, ϕ_1), and only well-defined geometries such as wedges and spheres offer the possibility of obtaining an analytical solution.

In addition to the described general formulation for intensity determination, we find that a correction is also needed in the *OPLD* calculation to properly account for non-planar interfaces. The interference of $\mathbf{I_1}$ and $\mathbf{I_2}$, shown in Fig. 3.1b, has been previously described to have an *OPLD* as follows[29]:

$$OPLD = n_1\left(\overline{AS} + \overline{SB}\right) - n_0\overline{CB}; \quad \overline{CB} = \sin(\theta_1)\overline{AB} \tag{3.6}$$

However, this equation is only valid in the particular orientation of the 2D situation described in Fig. 3.1b. For arbitrary geometries an expression in terms of vectors is more appropriate:

$$OPLD = n_1\left(\overline{AS} + \overline{SB}\right) + n_0\left(\mathbf{R_0} \cdot \mathbf{BA}\right) \tag{3.7}$$

Where $\mathbf{R_0}$ is the unitary vector (pointing upward) that defines the orientation of ray $\mathbf{I_0}$ in the glass side and **BA** is the vector from point *B* to point *A*, according to Fig. 3.1b. Although the vector product term in equation (3.7) is part of the calculation of the *OPLD* between $\mathbf{I_1}$ and $\mathbf{I_2}$, it can be applied to the interference between $\mathbf{I_1}$ and additional contributions $\mathbf{I_3}$, $\mathbf{I_4}$ … by taking into account that, in general, *A* represents the point source in the image plane of the corresponding complementary $\mathbf{I_0}$.

In the following section we describe how to perform intensity calculations according to equations (3.4) and (3.5). For simplicity, we concentrate on geometries such as wedges and arbitrary convex surfaces, although these equations are general and can be applied to any arbitrary geometry with any number of layers. The selected geometries allow us to explore

simplifications to the problem so we can take advantage of the backward ray-tracing method to make the computations easier and practical.

3.3.2 RICM intensity calculations in wedges and convex surfaces

In geometries such as wedges and convex surfaces, a consistent indexing in (θ_i, ϕ_i), $i \geq 2$, is sometimes possible by performing a change of variables. We use the subscript "*i*" to generalize a feasible indexing by using any ray incident at $B(x, y)$ after being reflected back from any layer of the non-planar interface. In order to be successful, any single or multiple consistent indexing must be able to account for the contributions of all rays incident at *B*. Such indexing defines a 2D set of angles in the $\theta_i\phi_i$-plane, Ω_i, and has to correspond to a one-to-one mapping between points inside Ω_1 and Ω_i. Therefore, we formally introduce the map **G** of Ω_1 onto Ω_i defined by the change of variables:

$$\mathbf{G}: \begin{cases} \theta_i = \boldsymbol{\theta_i}(\theta_1, \phi_1) \\ \phi_i = \boldsymbol{\phi_i}(\theta_1, \phi_1) \end{cases} \tag{3.8}$$

That leads to:

$$I(x, y) = \left\langle \frac{\int_{\Omega_i} \mathbf{E} * \mathbf{E}\, \mathrm{d}\Omega}{\int_{\Omega_i} \mathrm{d}\Omega} \right\rangle_t = I^s + I^p \tag{3.9}$$

$$I^{s,p} = \frac{\iint_{\Omega_i} \left[R^{s,p}(\theta_i, \phi_i) * R^{s,p}(\theta_i, \phi_i)\right]\left[I_0(\theta_1(\theta_i, \phi_i))/2\right] J(\theta_i, \phi_i)\, \mathrm{d}\theta_i\, \mathrm{d}\phi_i}{\iint_{\Omega_i} J(\theta_i, \phi_i)\, \mathrm{d}\theta_i\, \mathrm{d}\phi_i} \tag{3.10}$$

Notice that the differential element of solid angle is now given by $\mathrm{d}\Omega = J(\theta_i, \phi_i)\mathrm{d}\theta_i\mathrm{d}\phi_i$, where $J(\theta_i, \phi_i)$ is the Jacobian of the transformation[84]. Because the map **G** depends on the geometry of the reflecting surface, this Jacobian is also a function of it and its calculation requires the first-order partial derivatives of the mapping functions to be continuous.

The most important condition for the success of equations (3.9) and (3.10) is the complete transformation of the integration space Ω_1 delimited by α_{IA}. When we use (θ_i, ϕ_i) variables, such solid angle is transformed by the geometry of the reflecting surface and it may be that only a partial transformation into Ω_i is possible. This is illustrated in Fig. 3.2 using the geometry of wedges. For the 30° wedge in the top row, the main constraint in both domains is α_{IA} and the interaction with α_{DA} produces two regions, one with only $\mathbf{I_1}$ contributions and a second one with interference of $\mathbf{I_1}$ and $\mathbf{I_2}$, which can be completely observed in Ω_1 and Ω_2. The intensity can therefore be calculated using either equations (3.9) and (3.10) or Equations (3.4) and (3.5) as shown in the third figure. In the 40° wedge at the bottom row, Ω_2 is cut off by α_{TIR} (total internal reflection limit) and from the translation of this limit to Ω_1 we can see that there is a missing region, $\mathbf{I_1}^*$, outside the borders, with only $\mathbf{I_1}$ contributions. In this situation, only equations (3.4) and (3.5) give the correct result while equations (3.9) and (3.10) produce a different value as can be seen in the intensity profile.

In addition to the possibility of not accounting for all contributions to the intensity when performing the change of variables, calculation of the Jacobian of the transformation implies that we know the relationship between (θ_1, ϕ_1) and (θ_i, ϕ_i). This is basically the same reason that makes the direct application of the general formulation impractical when dealing with an arbitrary geometry. Therefore, although equations (3.9) and (3.10) are given in terms of (θ_i, ϕ_i) variables, we still cannot take full advantage of the backward ray-tracing method. However, we can obtain a new formulation for the intensity calculation, where the inconvenient Jacobian in equation (3.10) is replaced by $\sin(\theta_i)$ such that the differential element of solid angle is now given by $d\Omega' = \sin(\theta_i)d\theta_i d\phi_i$. Consequently, we have:

$$I(x,y) \cong \left\langle \frac{\int_{\Omega_i} \mathbf{E} * \mathbf{E}\, d\Omega'}{\int_{\Omega_i} d\Omega'} \right\rangle_t = I^s + I^p \tag{3.11}$$

$$I^{s,p} = \frac{\iint_{\Omega_i} \left[R^{s,p}(\theta_i,\phi_i) * R^{s,p}(\theta_i,\phi_i)\right]\left[I_0\left(\theta_1(\theta_i,\phi_i)\right)/2\right]\sin(\theta_i)\,d\theta_i\,d\phi_i}{\iint_{\Omega_i} \sin(\theta_i)\,d\theta_i\,d\phi_i} \tag{3.12}$$

This formulation is not a mathematically correct transformation of equations (3.4) and (3.5) because $J(\theta_i, \phi_i) = \sin(\theta_i)$ only valid in the limiting case of planar parallel interfaces and we expect to obtain an approximate result that deviates from the correct one as the inclination of the non-planar interface increases. However, this approximated formulation yields correct fringe spacings from wedges and convex surfaces because it accounts for all the interference between complementary rays $\mathbf{I_0}$ with contributions $\mathbf{I_1}$, $\mathbf{I_2}$, $\mathbf{I_3}$… in such geometries. The fact that we might be missing single $\mathbf{I_1}$ contributions only affects the average intensity in the interferogram, similarly to what is seen in Fig. 3.2 (bottom row) for the case of the change of variables.

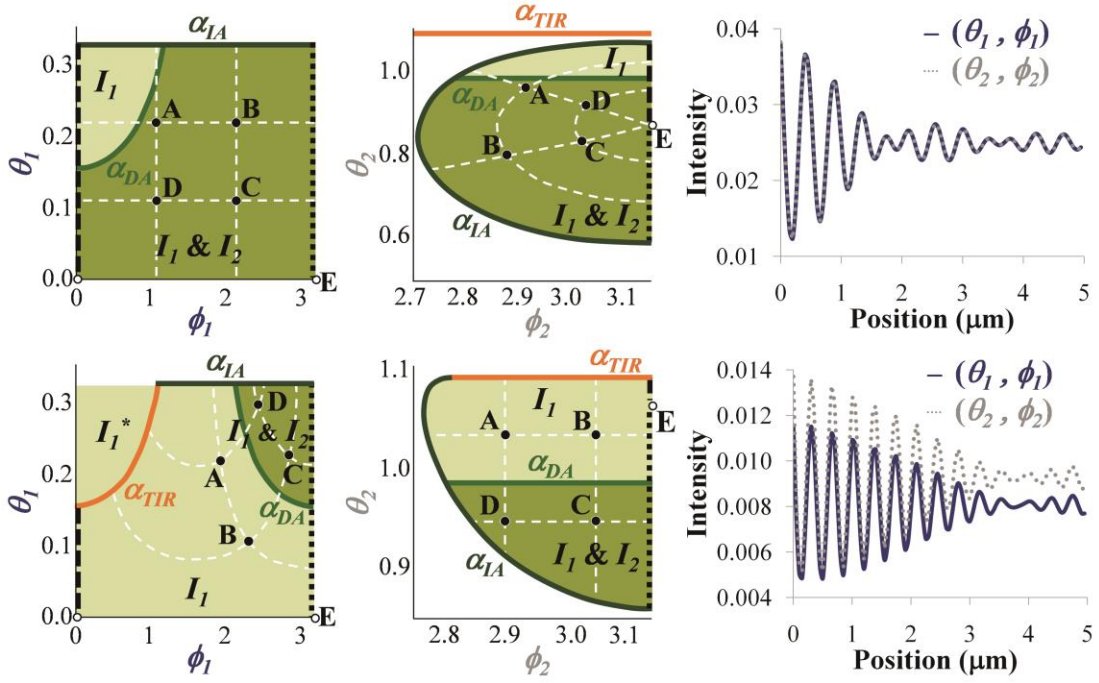

Figure 3.2. Missing intensities in wedge systems. Intensity calculations correspond to glass-water-air wedges of 30° (top row) and 40° (bottom row). The integration domains Ω_1 and Ω_2, shown in the first and second figures for each wedge, remain the same for all image plane positions where intensities are calculated and plotted in the third figure according to (θ_1, ϕ_1) and (θ_2, ϕ_2) indexing. To illustrate the transformation of Ω_1 into Ω_2 and vice versa, it can be seen how the boundaries of the integration domains, mainly determined by α_{IA} and α_{TIR}; four arbitrary interior points, A, B, C, and D; and some arbitrary interior lines, white dashed lines, translate from one domain to the other in each wedge geometry. The intensity profiles show that the change of variables is successful for the 30° wedge but not for the 40° wedge because of $\mathbf{I_1}^*$ contributions present in Ω_1 but missing in Ω_2. The simulations were performed in glass/water/air wedges with refractive indices 1.5/1.33/1, respectively, INA = 0.48, and NA = 1.25. Notice that $\theta_1 = 0$ represents a single point, E, at the Ω_2 boundary and ϕ goes only up to π in order to exploit the symmetry of the problem.

It is also important to consider how the approximated intensity profile is obtained from equations (3.11) and (3.12). The normalization term is no longer simply a constant given by α_{IA} because the absence of the correct Jacobian makes it a function that depends of the geometry of the reflecting surface, and possibly of position in the image plane. However, a similar issue associated with approximating the Jacobian also affects the numerator of equation (3.12), thereby making it possible to obtain the approximated intensity values from these equations after normalization. This is illustrated in Fig. 3.3, using simulations from a sphere, where the approximated solution gives acceptable intensity values (average relative error of 5.21%) that maintain the correct fringe spacing in the interferogram; the agreement is even better when smaller INAs are used (data not shown).

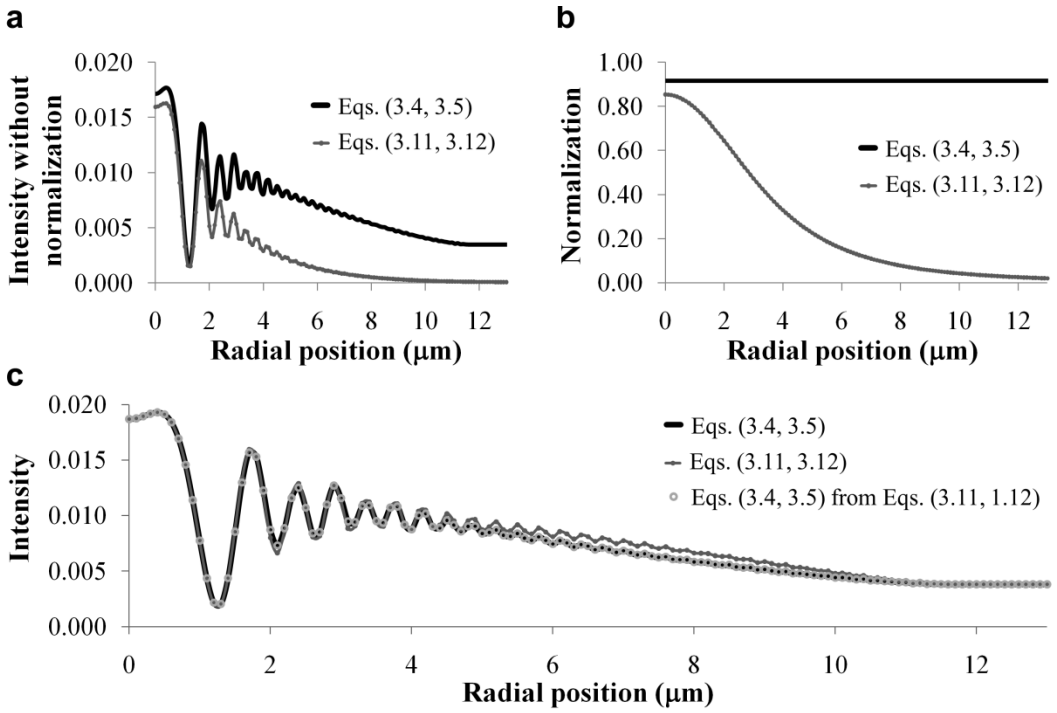

Figure 3.3. Exact and approximated intensity computations in convex geometries. Simulations corresponding to a 6 μm radius latex sphere in water and 100 nm above the glass surface, with INA = 0.78, NA = 1.25 and n_{latex} = 1.55, are performed to illustrate the behavior and convenience of the approximation given by equations (3.11) and (3.12) compared to the exact solution, equations (3.4) and (3.5). (**a**) The intensity without normalization is the calculation from the numerators of the mentioned equations; (**b**) the normalization corresponds to the evaluation of their denominators and (**c**) the final intensity value is obtained after normalization. It is important to point out that in these calculations there are no missing contributions in Ω_2.

Equations (3.11) and (3.12) can be directly implemented using simulations by backward ray-tracing of the rays with (θ_i, ϕ_i) orientation incident at $B(x, y)$, without previous knowledge of the relationship between (θ_1, ϕ_1) and (θ_i, ϕ_i), and applying appropriate normalization. However, the most significant aspect of this formulation is that numerical evaluation of the numerator in equation (3.11) allows indirect calculation of the exact intensity from equations (3.4) and (3.5). From Fig. 3.2 we see that within the boundaries of Ω_2 the map **G** is invertible; then, whenever $J(\theta_i, \phi_i) \neq 0$ we can write:

$$\mathbf{G}^{-1}: \begin{cases} \theta_1 = \boldsymbol{\theta_1}(\theta_i, \phi_i) \\ \phi_1 = \boldsymbol{\phi_1}(\theta_i, \phi_i) \end{cases} \tag{3.13}$$

Which defines the inverse map $\mathbf{G}^{-1}$ for wedges and convex surfaces. Therefore, when performing the integration in equation (3.11), we can proceed as follows: first, we find all contributions possible in Ω_i, by backward ray-tracing, with their corresponding effective reflection coefficients and intensities of the incident light; next, by using the idea of the inverse mapping, we proceed to relocate that information in Ω_1; finally, the existence of missing regions is determined in Ω_1 so that the missing contributions can be appropriately accounted for and the exact calculation according to equations (3.4) and (3.5) can be completed. More detailed information about the numerical construction of the inverse mapping and subsequent integration can be found in the Appendix A. Figure 3.3c shows a comparison between the exact calculation performed by direct evaluation of equations (3.4) and (3.5), the approximated calculation from direct evaluation of equations (3.11) and (3.12), and the indirect evaluation of equations (3.4) and (3.5) based on the direct evaluation of equations (3.11) and (3.12). It can be seen that we have successfully used the information collected from the approximated formulation and, via inverse mapping, performed an indirect evaluation of equations (3.4) and (3.5) which is in excellent agreement with the direct computation. This allows calculating exact intensity values in a much more computationally efficient manner when dealing with an arbitrary convex geometry.

Finally, we note how the previous formulation given by equations (3.1), (3.2), and (3.3) compares to the different sets of formulations developed here. When we look at the denominator of equation (3.3), we see that it corresponds to the same normalization term in equation (3.5), the exact general calculation, except that the numerator of equation (3.3) is equivalent to the one in equation (3.12), the approximated solution for wedges and convex surfaces. Consequently,

because the appropriate normalization term is required to obtain either the approximated or exact intensity, as seen in Fig. 3.3, it can be concluded that the previous formulation does not provide correct intensity values. However, we expect equations (3.1), (3.2), and (3.3) to accurately reproduce the fringe spacing in wedges and convex surfaces and to provide the correct intensity value in the limiting case of planar parallel interfaces, in the same way as the approximated solution.

3.3.3 RICM simulations of known geometries

The current mathematical models for wedges and spheres have been reviewed. For these known geometries it is possible to calculate the intensity directly from equations (3.4) and (3.5), equations (3.9) and (3.10) or equations (3.11) and (3.12), with essentially the same computational effort; thus, we can perform simulations to study and compare results from these formulations. In addition to the earlier discussions, we find that the normalization term in equation (3.12) is a particular constant for different inclination angles of the wedge, because the loci of contributions Ω_2, illustrated in Fig. 3.2, remain unchanged for all positions. On the other hand, simulations from a sphere in Fig. 3.3 illustrate how that normalization term monotonically decreases as a function of radial position. This behavior occurs due to the fact that the loci of contributions displace towards larger θ_i's and become smaller as we move away from the center of the sphere.

Also, we can use wedges and spheres to directly compare the results from our improved theory and models with previously published results[29]. Although, in general, equations (3.1), (3.2), and (3.3) do not produce the correct intensity values, the qualitative behavior previously observed in interferograms from these geometries is also obtained with the new general formulation. For instance, the mean intensity of fringe patterns from wedge geometries is constant within the interferogram (Fig. 3.2) but it is a function of the angle of inclination, while in the case of spheres the mean intensity varies within the interferogram (Fig. 3.3). This confirms that the mean intensity changes with local inclination of the non-planar interface, an effect that is successfully explained by the displacement of the loci of interference of the rays, the region labeled as "$\mathbf{I_1}$ **&** $\mathbf{I_2}$" inside Ω_2 in Fig. 3.2, and their interaction with constraints such as α_{DA}.

To look at the fringe spacing behavior, we notice that it is possible to obtain an approximated micro topography of the sample based on a fringe spacing analysis by using the simplest theory of RICM image formation[29,45]; when this is applied to wedges and spheres, the

inclination angle, β, and the radius of curvature, ρ, can be estimated, respectively. The deviation of such estimation from the correct values has been studied using simulations and an empirical correction term, δ_C, has been introduced as follows[29]:

$$\beta_C = \beta_{UC}\delta_{C,wedge}(\beta_{UC}) \tag{3.14}$$

$$\rho_C = \rho_{UC}\delta_{C,sphere}(\rho_{UC}) \tag{3.15}$$

Where the corrected measurement is obtained from the uncorrected value, denoted by subscripts UC, times the correction factor that is expressed as a function of uncorrected measurements. The statement made in equations (3.4) and (3.5) does not modify the fringe spacing with respect to equations (3.1), (3.2), and (3.3), however the correction made to the calculation of *OPLD* in equation (3.7) is expected to have a significant effect. This is shown in Fig. 3.4, where new correction factors for wedges and spheres are plotted and compared to the ones with the uncorrected *OPLD* and previously reported fittings (see equations (32) and (35) in[29] and the corresponding fitting parameters given). The fact that the factors calculated from uncorrected *OPLD* values, equation (3.6), follow previously reported fittings obtained by performing simulations of equations (3.1), (3.2), and (3.3) shows their agreement with our simulations. At the same time, it confirms that the fringe spacing remains invariant with respect

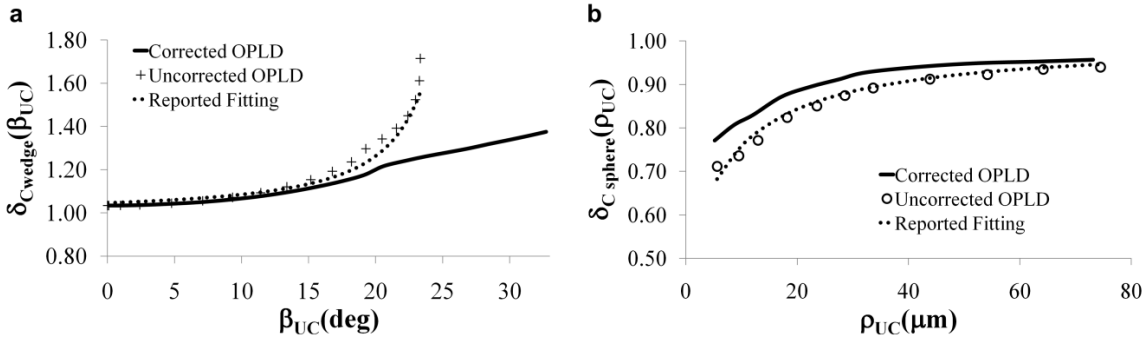

Figure 3.4. Comparison with previous results. Using the corrected *OPLD*, the correction factors for fringe spacing analysis in (**a**) wedges and (**b**) spheres have been determined. In addition, the factors calculated from the uncorrected *OPLD* are shown; they follow previously reported fittings obtained by using simulations of equations (3.1), (3.2), and (3.3). The systems studied correspond to glass-water-air for wedges and glass-water-latex for spheres contacting the substrate with INA = 0.48 and NA = 1.25.

to the formulation used for the intensity calculation. Finally, we see that the effect of the *OPLD* correction is basically to reinforce the results from the simplest theory as the correction terms are now closer to unity, especially for the cases of large inclinations of the non-planar interface.

Other known geometries such as ellipsoids and circular and elliptic cylinders have been studied, especially in order to determine the effect of using a cylindrical geometry to approximate a convex surface with non-zero Gaussian curvature. Some related results are discussed in the following section, in addition to simulations of double-layer systems with spherical geometry.

3.3.4 RICM of arbitrary convex surfaces

In this section we present an approach to model general convex reflecting surfaces with or without a thin layer. In addition, appropriate simplifications are studied that can enable the calculations to be performed faster without loss of accuracy. The simulations from such systems are performed according to the procedure described in Appendix A, using a numerically reconstructed inverse map. Then, a deformable polymer vesicle close to the glass surface is used to provide an experimental system that resembles an arbitrary convex surface.

3.3.4.1 Arbitrary convex surface model

Splines are smooth piecewise polynomial functions that can be utilized to model the contour of the object immediately above the observation line, the line where the intensity profile is measured and analyzed. Then, a general way to define a surface from this contour is to rotate the spline around a given axis. The location of the rotation axis, defined by the radius of rotation, *RoR*, gives the ability to represent the surface of the object under study that fits different experimental situations, as shown in Fig. 3.5a. This model allows arbitrary surfaces to be described and is able to exactly represent the geometries of spheres, with *RoR* = 0, and wedges and cylinders, with *RoR* = Infinity. The case of *RoR* = Infinity, referred to as the cylindrical approximation, is of particular interest because it has the advantage that a 3D geometric problem of finding intersections between the rays and the surface is simplified to a 2D problem, making the calculations easier and faster. At the same time, it is expected to be a valid approximation for any convex geometry because the RICM image is a strong function of the local height of the object, which remains unchanged.

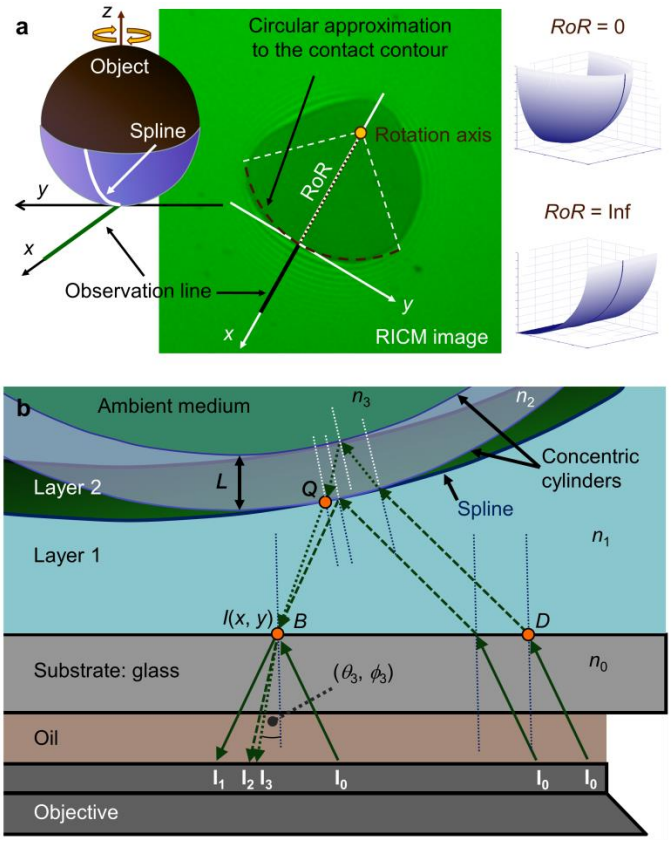

Figure 3.5. Arbitrary convex surfaces and double-layer systems. (**a**) Spline model for an arbitrary convex surface that fits different experimental situations by adjusting the *RoR* parameter. (**b**) Local geometry, approximations, and contributions to the intensity in the spline model extension to double-layer systems.

In order to evaluate our model, we performed simulations of latex spheres in water contacting a glass surface with NA = 1.25 using the exact geometry, and compared their interferograms with the ones from the cylindrical approximation. In general, the same fringe spacings are maintained across all radial positions and no difference is observed in the initial portion of the intensity profile although the magnitude of the intensity curve obtained from the cylindrical approximation diverges somewhat from the exact geometry. It is found that the average of the relative error between the interferograms, taken up to the point where the profiles decay to the background intensity, follows a linear trend with INA values larger than 0.48; the error is about 1.66% for INA = 0.48 and 4.76% for INA = 0.98. Several simulations show that this relative error presents small variations with the sphere size and can be as small as 1.03% for INA = 0.28. The behavior can be explained given that the loci of contributions become larger as

the INA value increases, collecting more information about the lateral shape of the object. Therefore, if the sphere is replaced by an elongated ellipsoid, the error decreases and tends to zero as the elongation becomes larger. For instance, the cylindrical approximation accurately represents the interferogram, along the *x* axis, of an elongated ellipsoid with radii 4, 40, and 4 μm along the *x*, *y*, and *z* axes, respectively. Because the spline model with *RoR* = Infinity does not introduce a significant error in the calculated intensities, especially when a small INA is used, subsequent simulations involving double-layer systems are performed using this model.

3.3.4.2 Model extension to double-layer systems

To the best of our knowledge, explicit models using the non-planar interface image formation theory in double-layer systems have not been reported. Thus, we formulated a method to calculate the intensity in these systems considering that the second layer resembles a membrane or ultrathin coating of arbitrary convex geometry with a uniform thickness, *L*, much smaller than the object size. The calculation is based in the indirect evaluation of equations (3.4) and (3.5), taking advantage of the backward ray-tracing method, as described in the Appendix A for a single-layer system. Therefore, when calculating the intensity $I(x, y)$ at a point *B*, every individual beam incident at that point and resulting from a reflection at the second layer/ambient medium interface, $\mathbf{I_3}$, is traced backward to a source point *D*, see Fig. 3.5b. In order to do this, the following approximation is used to speed up the calculations: once $\mathbf{I_3}$ intersects the spline at a point *Q*, the radius of curvature at *Q* is calculated to define concentric circular cylinders that model the local curvature and thickness of the layer, as illustrated in Fig. 3.5b. Using this local and well defined geometry, the tracing backward of the beam $\mathbf{I_3}$ can be completed to its source $\mathbf{I_0}$ at a point *D*, and the two complementary $\mathbf{I_0}$ beams with contributions $\mathbf{I_1}$ and $\mathbf{I_2}$ can be determined.

Notice that we trace backward $\mathbf{I_3}$ instead of $\mathbf{I_2}$. The main reason for this is to avoid an additional and necessary numerical search for $\mathbf{I_3}$ if we select $\mathbf{I_2}$; by choosing $\mathbf{I_3}$ and obtaining $\mathbf{I_0}$, $\mathbf{I_2}$ can be determined analytically from the cylindrical geometry after solving a fourth order polynomial equation. In addition, that choice does not introduce a consistency problem because the thickness of the second layer is assumed to be much smaller than the local radius of curvature and, consequently, $\mathbf{I_2}$ and $\mathbf{I_3}$ exist simultaneously. This represents the situation where a multiple and consistent indexing is possible for equations (3.11) and (3.12), which allows the indirect calculation of equations (3.4) and (3.5).

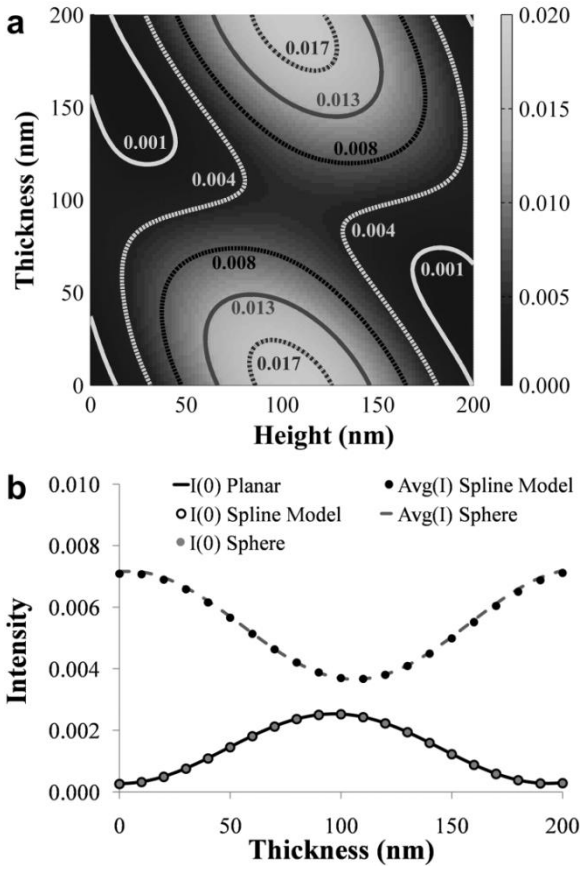

Figure 3.6. RICM in a spherical double-layer system. (**a**) The intensity at the center of the interferogram, *I*(0), can be easily obtained from the planar theory considering that the particle is close to the surface, and the thickness of the coating is small. (**b**) The non-planar theory gives the same information for *I*(0) and it points out that the average intensity of the interferogram, Avg(*I*), can be correlated with the thickness of the coating, as it can be seen for the case when the particle is in contact with the glass. The simulations are performed with INA = 0.48, NA = 1.25 and *RoR* = Infinity in the spline model.

To look at the implementation of this double-layer model, we performed simulations of a 6 μm radius latex sphere with an ultrathin coating (< 200 nm thickness) of refractive index 1.45 in water. For a symmetric particle with a convex geometry at its bottom, the intensity at the center of the interferogram, radial position 0 μm, can be calculated from the theory for stratified planar structures[29]. Using this planar theory it is possible to account for all reflections from the three interfaces involved, glass/water, water/coating and coating/latex, in addition to the finite aperture effect. This is shown in Fig. 3.6a where the intensity is plotted as a function of the thickness of layer one, height of the particle above the glass surface, and layer two, thickness of

the coating. If the height and the thickness are unknown, a single intensity at the center of the interferogram might correspond to multiple (height, thickness) pairs, as can be seen from the contours in Fig. 3.6a. Therefore, a more detailed analysis involving the complete intensity pattern and the geometry of the particle is required to obtain a unique solution.

Here we consider that the coated particle is in contact with the substrate, so the intensity at the center of the interferogram, $I(0)$, can be directly correlated with the thickness of the coating (Fig. 3.6b). These results verify the agreement between the intensity $I(0)$ obtained from the planar and non-planar theories, using the exact model for a sphere and the corresponding spline model with RoR = Infinity. Also, simulations from the non-planar theory indicate that the average intensity of the interferogram, Avg(I), can be correlated with the thickness of the coating. This additional information could be used to discriminate between thicknesses that give the same intensity $I(0)$. Finally, notice that the Avg(I) curve obtained from the cylindrical approximation is in very good agreement with the one from the spherical geometry, with an average relative error of 0.75%; confirming that the spline model with RoR = Infinity is a suitable model for intensity calculations in double-layer systems.

3.3.4.3 Experimental observation of a polymer vesicle near the substrate

A 200 μL volume of vesicle solution was placed in a sealed chamber on top of a cover glass coated with bovine serum albumin, BSA, to avoid adhesion and spreading of the vesicles onto the glass surface. After settling, the vesicles float above the glass surface in a slightly deformed configuration with respect to their spherical shape when they are free in solution. Figure 3.7a shows the RICM image of one of these vesicles using the smallest illumination numerical aperture available, INA = 0.48.

In this particular experiment, the shape of the object under observation and its height above the substrate are unknown, but they can be determined because we know all the parameters in the system. The refractive indices of glass, buffer and sucrose solutions are 1.530, 1.335 and 1.351, respectively, from RICM measurements. The polymer membrane is given by the hydrophobic core of polybutadiene; according to the literature, its thickness is about 15 nm[85] with a refractive index of 1.51[86]. Also, two additional effects have been incorporated into the simulations; first, the real illumination profile, $I_0(\theta_1)$, and second, a cosine-fourth law factor that affects the intensity of the rays incident at the position of interest.

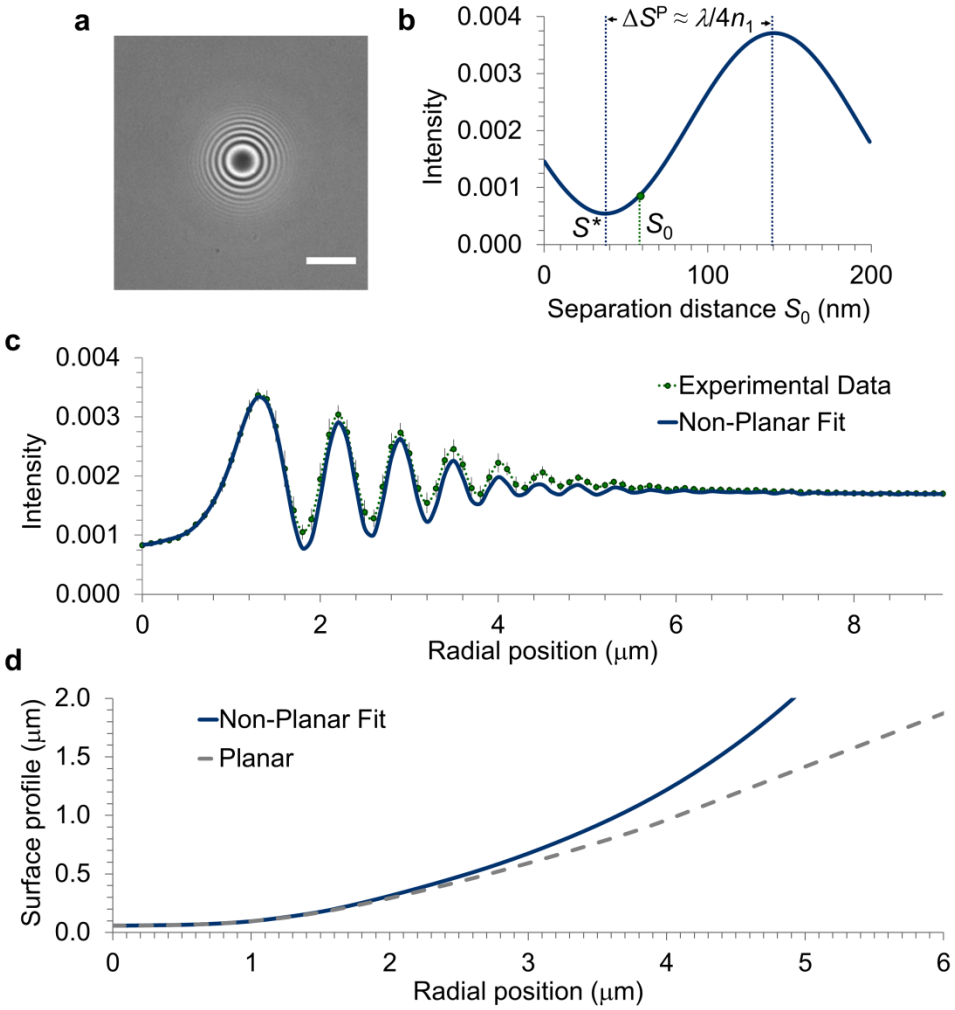

Figure 3.7. Experimental observation of a polymer vesicle near the substrate. (**a**) RICM image of a polymer vesicle in PBS and filled with sucrose solution when it is close to a glass surface coated with BSA (5 μm scale bar). (**b**) The intensity at the center of the interferogram, given by the planar theory, is used to determine the height of the vesicle above the glass surface. (**c**) The intensity profile is obtained from a circular average of the picture shown in (a). The experimental data were fitted by using the improved non-planar interface image formation theory and the spline model with *RoR* = Infinity. (**d**) Reconstructed bottom shape of the vesicle according to the non-planar and planar models.

The analysis of the experimental data begins with the determination of the minimum separation distance between the vesicle and the glass surface, S_0. We have previously seen in Fig. 3.6 that the intensity at the center of the interferogram is basically object size and shape independent and, given that the membrane thickness is known, it can be directly correlated with this minimum height using simulations from the planar theory that account for the INA and NA

effects, as seen in Fig. 3.7b. This is how we find S_0 = 59 ±1 nm, taking into account that the intensity continuously increases from the center up to the first intensity peak in Fig. 3.7c.

Now we determine the bottom shape of the vesicle that gives the best fit to the experimental intensity pattern. The traditional RICM analysis considers that the surface profile can be reconstructed by inverse cosine transform of the intensity distribution[45]; however, when dealing with a double-layer system, it has been pointed out that the traditional analysis underestimates the heights by a value S^*, in this case 37.4 nm[51]. Therefore, we use the result illustrated in Fig. 3.7b to obtain an appropriate fast reconstruction of the profile using the planar theory. The incremental height difference between two adjacent intensity extrema is ΔS^P = 103.8 nm, which is close to the value for normal incidence light, $\lambda/4n_1$ = 102.3 nm, in the traditional analysis; then, based on the previously determined S_0, the height for the first intensity peak ($S^* + \Delta S^P$), and the distance between consecutive extrema obtained from Fig. 3.7c, the bottom shape of the vesicle is reconstructed and the result is presented in Fig. 3.7d.

By incorporating the improved non-planar theory and the arbitrary convex surface model with a thin membrane, an additional surface profile is reconstructed, see Fig. 3.7d. Because the simulated intensity profile obtained from the reconstructed contour successfully reproduces the experimental data in Fig. 3.7c, it can be concluded that it corresponds to an accurate representation of the bottom shape of the vesicle under study. Up to a radial position of 1.5 μm there are no significant curvature effects and the bottom shape given by the planar theory is within 3% of error when compared to the non-planar result; however, beyond that point the error quickly increases reaching 20% at 4 μm. To the best of our knowledge, this is the first time that an accurate RICM analysis is performed in a double-layer system of unknown geometry.

3.4 Discussion

The improvement of the RICM image formation theory, with the general formulation for intensity calculations in equations (3.4) and (3.5), successfully accounts for contributions to the intensity that can be missing in previous formulations. But analysis of wedges and convex surfaces shows that the implementation of this formulation is not trivial, leading us to develop a method to obtain the exact result from an approximated, intermediate, formulation. In addition, simulations of known geometries such as wedges and spheres allow a direct comparison with previous models, revealing that the *OPLD* correction, equation (3.7), becomes important for

large inclinations of the non-planar interface and that the fringe spacing analysis is more accurate than previously thought.

RICM can be used to obtain valuable information from the system under study. For instance, by using simulations, we explored how to determine the thickness of an ultrathin coating (< 200 nm) on a spherical particle. The development of a general model for an arbitrary convex surface, including a uniform second layer which could be a thin coating or a membrane, expands the possible range of systems that can be accurately studied using RICM. Because RICM experiments are usually performed using the smallest INA available, a particular case of this surface model, the cylindrical approximation, becomes a suitable model with an expected average relative error in the calculated intensity profile smaller than 2%. If high INAs are used, the average relative error would be larger than 5%, but the correct fringe spacing is still maintained. Our experimental work with polymer vesicles shows that the coupling of the improved RICM image formation theory and the surface model allows an accurate reconstruction of the convex bottom shape of an object close to the substrate by fitting its experimental intensity profile.

A natural direction for expansion of the present work would be the study of concave geometries. RICM has already been employed to measure small contact angles of droplets using a wedge approximation[29,87] or simple fringe spacing analysis[36,88]; however, there is not a clear idea of the error involved in such measurements. Because it is possible to have multiple contributions to the intensity coming from different regions of a concave geometry, a consistent indexing based on rays that are reflected back from the object might not be feasible. Therefore, our formulation for intensity calculations is expected to play a critical role in this scenario. Also, the formulated method to calculate intensities in double-layer systems could potentially be used to analyze more complex systems such as cells, with different reflection distributions (for example, due to local refractive index heterogeneities) on the membrane. These local variations can be incorporated into the intensity calculation via the effective reflection coefficient, R, and their effect in interferograms when the object shape remains unchanged could be evaluated.

CHAPTER IV
A NANOMETER-SCALE RESOLUTION INTERFERENCE-BASED PROBE OF INTERFACIAL PHENOMENA BETWEEN MICROSCOPIC OBJECTS AND SURFACES[*]

4.1 Overview

Interferometric techniques have proven useful to infer proximity and local surface profiles of microscopic objects near surfaces. But a critical trade-off emerges between accuracy and mathematical complexity when these methods are applied outside the vicinity of closest approach. Here we introduce a significant advancement that enables reflection interference contrast microscopy (RICM) provide nearly instantaneous reconstruction of an arbitrary convex object's contour next to a bounding surface with nanometer resolution, making it possible to interrogate microparticle/surface interaction phenomena at radii of curvature 1,000 times smaller than those accessible by the conventional surface force apparatus. RICM's unique view-from-below perspective also reveals previously unseen deformations and allows the first direct observation of femtoliter-scale capillary condensation dynamics underneath micron-sized particles. Our implementation of RICM provides a generally applicable nanometer-scale resolution tool that can be potentially exploited to dynamically probe ensembles of objects near surfaces so that statistical/probabilistic behavior can be realistically captured.

4.2 Introduction

Deformation of soft micron-sized particles near surfaces is fundamentally important in fields ranging from colloid science to biomedicine[39,64,89-93]. However, these phenomena are challenging to directly probe, because the corresponding deformation dynamics often cannot be resolved with sufficiently high spatial and temporal resolution. An experimental technique that has shown particular promise involves illuminating an object in close proximity to a surface from below using monochromatic light. Interference of light reflected back from different optical interfaces

[*] Reprinted with permission from "A nanometre-scale resolution interference-based probe of interfacial phenomena between microscopic objects and surfaces" by Jose C. Contreras-Naranjo and Victor M. Ugaz, 2013, Nature Communications 4:1919 doi: 10.1038/ncomms2865, Copyright 2013, Nature Publishing Group

in the system directly reveals the existence of contact phenomena, if any, while the characteristic fringe pattern that emerges inherently embeds detailed information about the object's shape near the substrate at up to a microsecond-scale temporal resolution[15]. Reflection interference contrast microscopy (RICM)[45,48,49] employs non-planar interface image formation theory as a basis to extract this information and accurately reconstruct the surface profile, but its mathematical complexity renders the model cumbersome to implement in its full form.[29-31,94,95] These difficulties have stimulated development and continuous use of approaches that simplify the connection between the object's shape and the spacing between neighboring fringes in the interferogram[24,33,35,36,45,46]. But this simplicity is achieved at the expense of reconstruction accuracy, particularly when applied to curved microscopic objects, because these methods are strictly valid only for the case of planar parallel interfaces. We have devised a hybrid approach that couples a simplified non-planar RICM model with an innovative analysis of the entire interferogram; as a result, an arbitrarily-shaped convex object can be accurately reconstructed with an unprecedented nanometer-scale resolution.

4.3 Results

4.3.1 Direct imaging of contact phenomena

Our approach provides an extraordinary accurate picture of microparticle-surface interaction phenomena that greatly enhances well-known RICM capabilities extensively applied in the study of particle, cell, and lipid/polymer vesicle adhesion[21-28]. However, this technique has seen limited application in other fields where the great potential behind RICM's high resolution, set-up simplicity, and unique non-invasive "view-from-below" perspective can produce a significant impact. This becomes evident by comparing the RICM images obtained from polystyrene latex (PSL) particles deposited on a glass substrate under different conditions. Qualitatively, no significant particle deformation and a finite separation distance from the substrate are seen when dry particles are directly deposited on the surface (dry deposition, Fig. 4.1a) and observed within a few hours, as indicated by interferograms that display a clean uniform pattern of concentric rings without a minimum intensity value at the center. But some RICM images significantly change when the particles are deposited evaporatively from solution (wet deposition) and observed after more than 24 hours. Here, the concentric ring pattern no longer extends to the center of the interferogram, but terminates at a finite radius outlining what looks like a contact

area with a non-homogeneous intensity (Fig. 4.1b). Scanning electron microscopy (SEM) images also reveal significant changes in the contact region due to the water meniscus and accompanying capillary forces imposed during drying[96,97]. The extreme nature of these forces is especially evident in visible rugosity, in some cases appearing as if material has been pulled away from the particle surface. The interferograms become further distorted when impurities in the deposition solution accumulate around the perimeter of the contact zone (Fig. 4.1c). Although the interference fringe patterns become difficult to distinguish, the shape and extent of the surrounding deposition region can be quantified.

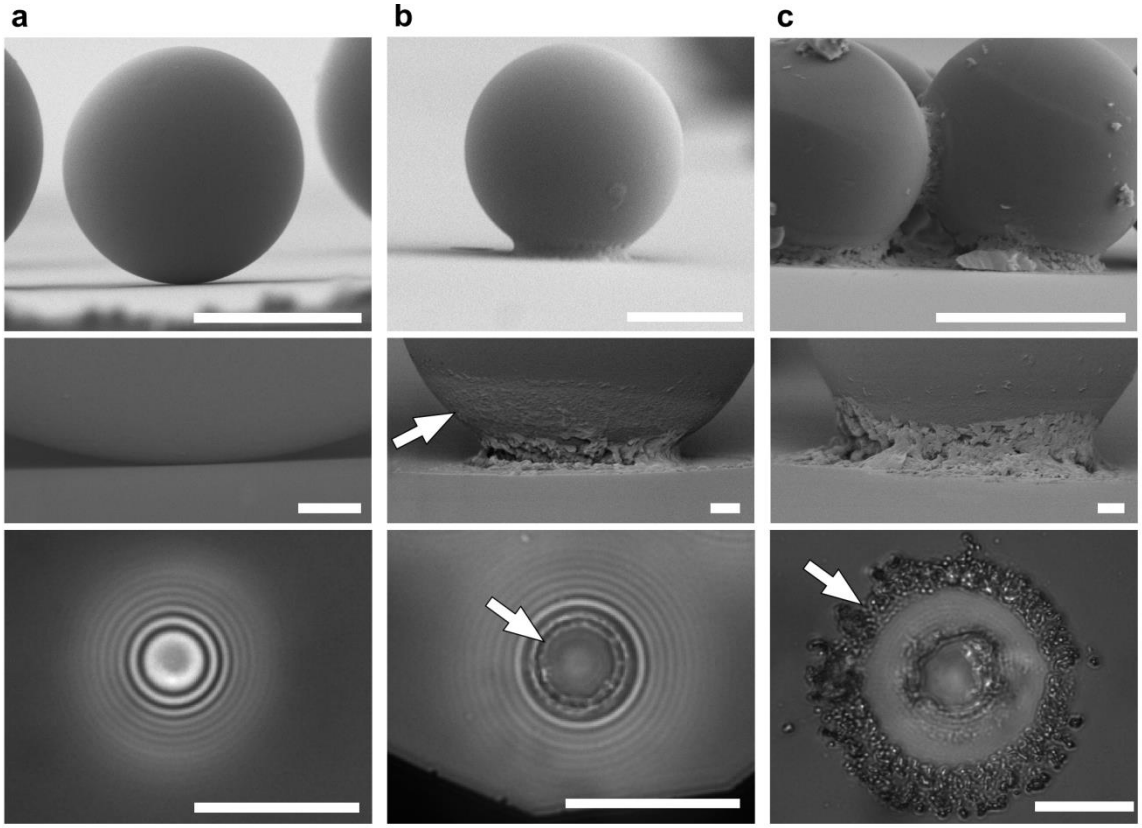

Figure 4.1. RICM reveals different particle deposition scenarios. Dry **(a)** and wet **(b-c)** deposition of 15 μm diameter PSL particles on a glass substrate studied with SEM (top/middle; 10/1 μm scale bars) and RICM (bottom; 10 μm scale bars). Contrary to (a), a contact region with a non-uniform appearance and substantial rugosity in the SEM (arrow) are seen in (b) and these non-uniformities become magnified when impurities accumulate underneath and around the particles in (c). In both (b) and (c), the RICM images clearly show the shape and extent of these features (arrows).

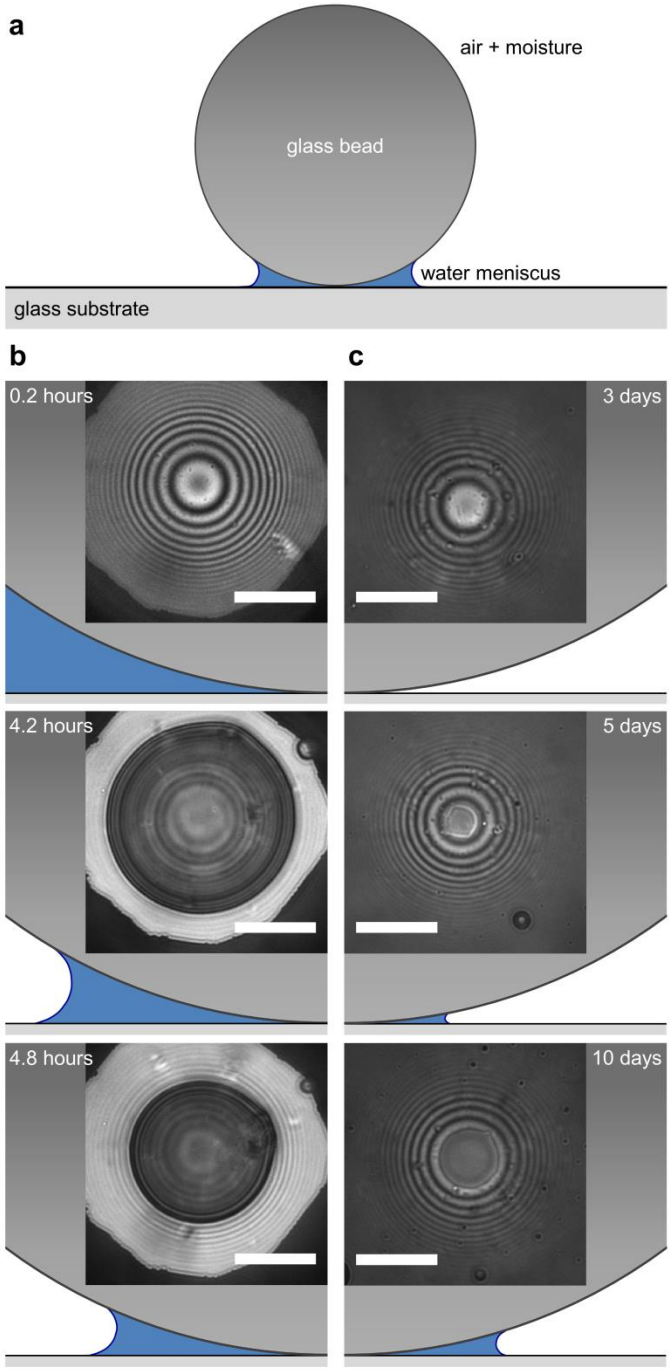

Figure 4.2. RICM observation of a liquid meniscus between micron-sized particles and a substrate. **(a)** Schematic representation of the water meniscus between 30-60 µm diameter glass beads and a glass surface. Following wet deposition, a meniscus forms and shrinks due to evaporation **(b)**, whereas a few days after dry deposition, this interfacial water appears and increases by condensation under ambient conditions (20 °C, 51 % relative humidity) **(c)**. Menisci illustrations in (b) and (c) are not drawn to scale; 10 µm scale bars in RICM images.

RICM also enables direct observation of liquid water underneath larger glass beads (Fig. 4.2a), as evident by a continuously shrinking meniscus due to drying following wet deposition (Fig. 4.2b) and visible motion of the meniscus boundary when an external air flow is imposed. Unexpectedly, a distinct meniscus remains evident even after 72 h of drying under vacuum. Hence, RICM directly reveals, for the first time to the best of our knowledge, the presence of small amounts of water (volumes in the order of 1 fL owing to capillary condensation[97]) underneath micron-sized particles after dry deposition on a glass substrate and upon exposure to ambient conditions for several days (Fig. 4.2c).

4.3.2 Fringe spacing analysis based on simplified non-planar RICM

Although contact phenomena can be directly observed and quantified (typically as an area in the RICM image), accurate analysis of the interference pattern requires a link between the intensities and the object's geometry (Fig. 4.3).

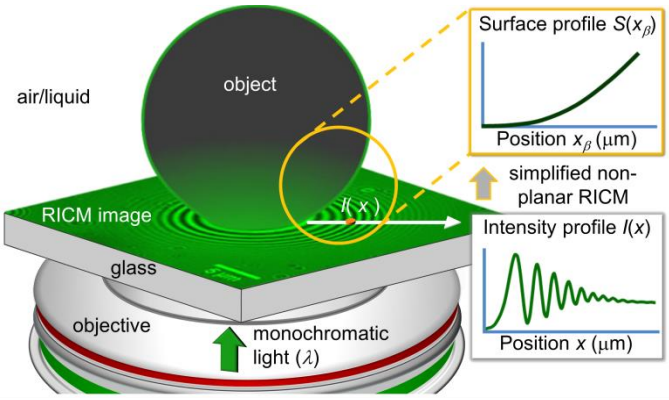

Figure 4.3. Schematic of surface profile reconstruction. Interference fringe patterns obtained from RICM images embed precise information about an object's topography in the vicinity of contact with a surface.

Instead of applying the complete non-planar interface image formation theory where all possible contributions to the observed intensity must be individually determined,[95] we consider a simplified two-dimensional model whereby a single set of complementary rays, $\mathbf{I_0}$, interfere to produce the intensity observed at a position x in the interferogram, $I(x)$. For the single-layer

system in Fig. 4.4a, $I(x)$ depends on the interference of rays $\mathbf{I_1}$ and $\mathbf{I_2}$ in terms of their optical path length difference *OPLD* (term in square brackets) as follows.

$$I(x) = I_1 + I_2 + 2\sqrt{I_1 I_2}\cos\left(\frac{2\pi}{\lambda}\left[2n_1 S(x_\beta)\frac{\cos^2(\theta_R)}{\cos(\beta+\theta_R)}\right]+\delta\right) \tag{4.1}$$

Here, β is the inclination angle of the non-planar interface at position x_β relative to the horizontal plane, $S(x_\beta)$ is the object's local height above the substrate at x_β, θ_R is the angle of reflection at $S(x_\beta)$, λ = 546 nm is the wavelength of the illuminating light (only monochromatic green light is considered here), n_1 is the refractive index of layer 1 (L1), and δ accounts for a phase shift of π if the refractive index of the object is higher than the index of the medium. Therefore, the intensity at x can be determined using geometric parameters $S(x_\beta)$, β, and θ_R at any appropriate x_β, where the following relationship, from the geometry in Fig. 4.4a, is satisfied:

$$x_\beta = x - S(x_\beta)\tan(\beta+\theta_R) \tag{4.2}$$

The ensemble of admissible x_β is bounded by the range of incident angles within the illumination and detection cones (α_{IA} and α_{DA}, respectively), according to the complete non-planar RICM theory. By identifying the single set of complementary rays making the most significant contribution to $I(x)$ within these constraints, our analysis seeks to establish a bijective mapping between x and x_β applicable to the whole range of conditions where interference occurs. In contrast, previous simplified models formulated since the early stages of RICM have seen their accurate implementation limited to interfaces with small inclinations and/or small illumination numerical aperture (INA) values, because they neglect non-planar effects ($\beta = 0$) and/or assume that only normal incidence light ($\theta_R = \beta$) is important[45,46,49,78,98].

To envision this, we first consider a wedge geometry (β = constant) in which case *OPLD* = $2n_1\sin(\beta)\cos(\theta_R)x$. The cosine dependence in *OPLD* implies that the most significant contribution to $I(x)$ occurs when *OPLD* is maximized; hence, our analysis is set at a given β, x, and n_1, leaving $\cos(\theta_R)$ as the remaining unknown. Although this term displays a maximum at $\theta_R = 0$, the admissible values are constrained by the finite range of allowable illumination and

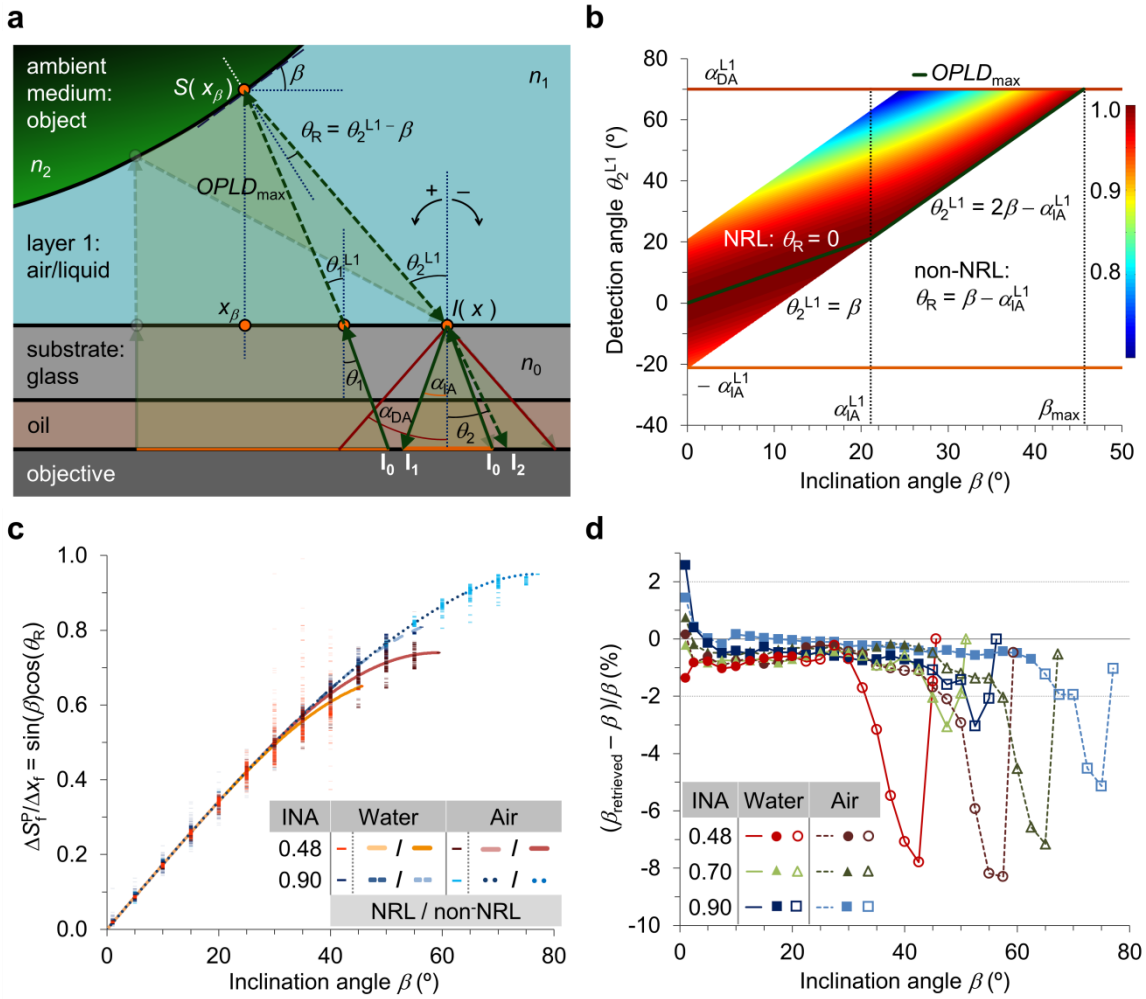

Figure 4.4. Fringe spacing analysis based on simplified non-planar RICM. (a) Simplified non-planar RICM image formation model. The intensity $I(x)$ is produced by the interference of rays $\mathbf{I_1}$ and $\mathbf{I_2}$ which correspond to the single set of complementary rays $\mathbf{I_0}$ with the maximum *OPLD* (determined by geometric parameters $S(x_\beta)$, β, and θ_R defined at position x_β) among all possible contributions (shaded area). Complementary $\mathbf{I_0}$ originate from within the illumination cone ($\theta_1 \leq \alpha_{IA}$, where α_{IA} is given by the illumination numerical aperture, INA, of the microscope); then, they are reflected back from planar (substrate/layer 1 at x) and non-planar (layer 1/object at x_β) interfaces producing rays $\mathbf{I_1}$ and $\mathbf{I_2}$, respectively, which interfere at position x only if they are incident within the cone of detected light ($\theta_2 \leq \alpha_{DA}$, where α_{DA} is determined by the numerical aperture, NA, of the objective). **(b)** The formulation of the simplified non-planar RICM model is completed when normal/non-normal reflected light regimes are identified at $OPLD_{max}$, as illustrated with a normalized *OPLD* plot for the range of detection angles corresponding to a series of wedge inclination angles with INA = 0.48 and water surroundings. **(c)** Despite the intrinsic fringe spacing variability, which produces the scattered data points, the behavior of $\Delta S^P_f/\Delta x_f$ with inclination angle observed in simulations from several different wedge systems is in excellent agreement with equation (4.4) where INA, n_1 (surroundings composition), and θ_R (reflected light regime) are the main parameters. **(d)** Percentage error of inclination angles retrieved from the averages of all fringe spacing values originated from simulations of comparable wedge systems. Closed and open symbols represent $\beta_{retrieved}$ using normal and non-normal reflected light models, respectively. In all figures, simulations are performed with NA = 1.25 for wedge angles ranging from 0° to β_{max}.

detection angles (Fig. 4.4b). When $\beta < \alpha_{IA,L1}$, $OPLD_{max}$ occurs when $\theta_R = 0$ (the normal reflected light (NRL) regime). For $\alpha_{IA,L1} \leq \beta \leq \beta_{max} = (\alpha_{IA,L1} + \alpha_{DA,L1})/2$, however, the set of rays corresponding to $\theta_R = 0$ no longer contribute to $I(x)$. Here, the angle θ_R associated with $OPLD_{max}$ is a function of β with $\theta_R = \beta - \alpha_{IA,L1}$ (the non-normal reflected light (non-NRL) regime). These regimes establish a map from β to θ_R and, therefore, a bijective mapping between x and x_β at $OPLD_{max}$ (see Appendix B).

To make the formulation more suitable for practical implementation, first equation (4.1) is rewritten in terms of experimentally measurable maximum and minimum intensities, I_{max} and I_{min} respectively, and a height value S^P is expressed as a function of $I(x)$ according to conventional inverse cosine transform methods.

$$S^P = S(x_\beta)\frac{\cos^2(\theta_R)}{\cos(\beta+\theta_R)} = \frac{\Delta S_f^P}{\pi}\cos^{-1}\left(\frac{A - I(x)}{B}\right) \tag{4.3}$$

Here, $A = (I_{max} + I_{min})/2$, $B = (I_{max} - I_{min})/2$, $\Delta S^P{}_f = \lambda/4n_1$, and $\delta = \pi$ for all cases studied. Notice that $S^P = S(x_\beta)$ only when planar parallel interfaces and normal incidence light are assumed ($\beta = \theta_R = 0$) and $\Delta S^P{}_f$ represents the constant height increment between two consecutive fringes. Then, using a wedge geometry (that is, where β and θ_R are both position independent), equation (4.2) and equation (4.3) are applied to any two intensities with a spacing Δx and located on a common branch of the intensity profile (that is, between the successive extrema that determine I_{max} and I_{min}) taken along the direction perpendicular to the fringe's front in the RICM image, so that the inclination angle β can be related to the corresponding measured increments ΔS^P and Δx (see Appendix C).

$$\sin(\beta)\cos(\theta_R) = \frac{\Delta S^P}{\Delta x} \tag{4.4}$$

To verify this relationship, we next cast our analysis in terms of Δx as the spacing between neighboring fringes in the interferogram Δx_f—a convenient parameter to extract experimentally; in this case, $\Delta S^P = \Delta S^P{}_f$ is constant. The complete non-planar interface image formation theory is used to simulate fringe spacings as a function of β in wedge systems under

an ensemble of different refractive index and illumination conditions for single- and double-layer objects in both air and water surroundings (see Appendix C, Table C1). Up to 51 individual fringes are computed for each case to account for intrinsic variability associated with Δx_f in a given wedge system. These data superimpose when co-plotted, thereby establishing a mapping from β to $\Delta S^P_f/\Delta x_f$ that is successfully reproduced by equation (4.4) when the appropriate reflected light regimes are used (Fig. 4.4c). Then, hundreds of $\Delta S^P_f/\Delta x_f$ values corresponding to comparable systems (that is the same β, n_1, and INA) are averaged to perform an inverse mapping (from $\Delta S^P_f/\Delta x_f$ to $\beta_{retrieved}$) by means of equation (4.4), to evaluate the accuracy of the fringe spacing analysis, as the original β is known (Fig. 4.4d). The values of $\beta_{retrieved}$ are in excellent agreement with those used in the simulations of the complete non-planar theory up to a cut-off value of β^* corresponding to the midpoint of the non-NRL regime in Fig. 4.4b. Therefore, equation (4.4) enables direct measurement of inclination angles of wedge shaped interfaces (from 0° to β^*), such as small contact angles of liquid droplets, avoiding the use of fittings or angular correction factors based on full non-planar theory calculations[29,87,95].

4.3.3 Near-instantaneous surface profile reconstruction

We now seek to apply these insights developed for wedges of constant β, toward analysis of intensity profiles corresponding to convex geometries with spatially varying inclination angles. Figure 4.5a shows $\Delta S^P/\Delta x$ for a spherical particle as a function of radial position from the center of the fringe pattern x obtained from interferograms simulated using the complete non-planar interface image formation theory. To generate this mapping, two different but complementary transformations of the intensity data are performed: first, for radial positions less than the location of the first intensity extrema, neighboring intensity values are analyzed so that Δx is constant and ΔS^P is calculated using equation (4.3) (Fig. 4.5a inset), and second, for those positions where interference fringes exist, Δx is taken as the fringe spacing Δx_f and $\Delta S^P = \Delta S^P_f$, exactly as in the previously discussed wedge case (for more details see Appendix D). As a result, the relationship between $\Delta S^P/\Delta x$ and x from the first transformation follows a clear and smooth trend although for experimental interferograms some variability is expected because of noise in the intensity values. The data from the second transformation is not as clearly defined as the $\Delta S^P_f/\Delta x_f$ versus β data for the wedge case (Fig. 4.4c), especially as radial position increases, because a single fringe spacing now incorporates contributions from multiple values of β at

different locations on the object's contour (in addition to the intrinsic variability observed in Δx_f for a particular β). A general trend can be established, however, by applying a smoothing procedure subject to the constraints that the smoothed $\Delta S^P/\Delta x$ data must increase monotonically with x, and according to equation (4.4) there is a maximum value that corresponds to β_{max}.

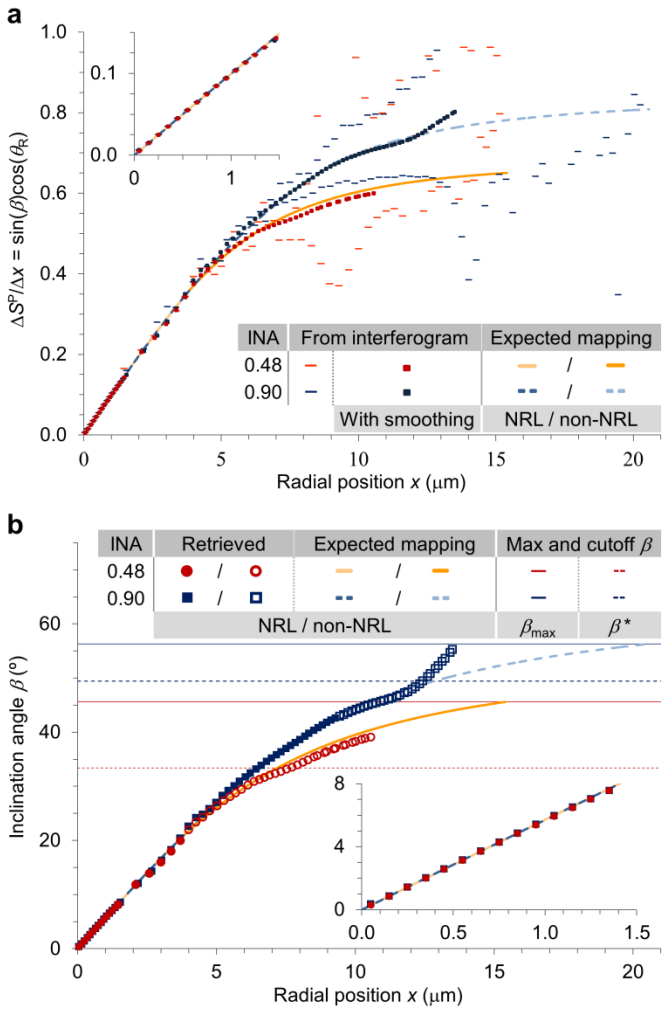

Figure 4.5. Convex geometry analysis. (a) Simulated $\Delta S^P/\Delta x$ versus x mapping corresponding to a 10 μm radius sphere in water contacting a glass substrate with NA = 1.25 and glass/water/particle refractive indices of 1.53/1.33/1.55, respectively. **(b)** Retrieved inclination angles from smoothed $\Delta S^P/\Delta x$ are cut off at β^* because significant errors are obtained beyond this value. Given that the geometry is known, it is possible to determine the expected mappings between the studied variables according to the normal/non-normal reflected light models.

Figure 4.5a reveals that the smoothed $\Delta S^{P}/\Delta x$ values closely follow the expected continuous mapping from x to $\sin(\beta)\cos(\theta_R)$ given by the geometry under consideration and the normal/non-normal reflected light regimes. This indicates that the simplified non-planar RICM model and equation (4.4) can be successfully applied to interferograms from convex geometries to accurately retrieve the inclination angles β associated with ΔS^{P} and Δx increments at discrete values of x (Fig. 4.5b). A logical approach to use this information would be to approximate the unknown surface profile of the object as an ensemble of wedges (shown for a spherical object in Appendix B, Fig. B1, where the intensity at each point in the interferogram is successfully mapped to a corresponding value of β). But it is challenging to use ΔS^{P}, Δx, and the retrieved β values alone to perform an accurate surface profile reconstruction because Δx is inherently large (that is, fringe spacing), limiting the resolution by which the profile can be discretized (see Appendix E), a current issue with simplified formulations that directly map fringe spacing to a constant incremental change in the object's local height above the substrate[45,46,49].

To overcome these limitations, a continuous approach to the problem is formulated. The discrete mapping between x and β in Fig. 4.5b is used to define β as a continuous function of x and, therefore, θ_R as a function of x. Then, the bijective mapping between x and x_β that is necessary to reconstruct the object's surface profile is achieved by using the geometrical relationship in equation (4.2) to obtain the following first order ordinary differential equation (see Appendix F).

$$\frac{dx_\beta}{dx} + F(x)\cdot x_\beta = G(x)$$

$$F(x) = -\frac{d(\tan(\beta+\theta_R))/dx}{\tan(\beta+\theta_R)+\tan^2(\beta+\theta_R)\tan(\beta)} \tag{4.5}$$

$$G(x) = \frac{\tan(\beta+\theta_R) - x\,d(\tan(\beta+\theta_R))/dx}{\tan(\beta+\theta_R)+\tan^2(\beta+\theta_R)\tan(\beta)}$$

The initial condition ${x_\beta}^0$ corresponding to the position x^0 of the first $\Delta S^{P}/\Delta x$ data point is determined from equation (4.2), where $\beta(x^0)$ and $\theta_R(x^0)$ are given by the previously defined mappings, and a slightly modified equation (4.4) (to account for an additional phase-shift factor

S^* when multiple layers are present[51]) provides $S(x_\beta^0)$ (see Appendix G). The differential equation is straightforward to solve with the minimal computational effort (for example, using MATLAB on an ordinary desktop PC) and a continuous surface profile is obtained by reorganizing equation (4.2) in the form $S(x_\beta)$ versus x_β.

We validated our simplified reconstruction approach using experimentally obtained interferograms from the RICM analysis of a glass bead in air and polymer vesicles in aqueous medium, which are in close proximity to a glass substrate (Fig. 4.6; INA = 0.48 and NA = 1.25). The optical path in the glass bead system is composed of glass/air/glass media with refractive indices of 1.53/1/1.51, respectively. The polymer vesicle systems involve glass/buffer/polymer membrane (15 nm thickness[85])/sucrose solution with refractive indices of 1.53/1.334 /1.51/1.351, respectively.

Our method enables reconstructed surface profiles to be obtained near-instantaneously (~ 1 s of computation time) from the corresponding interferograms (Fig. 4.6a-c). For comparison, two of these contours are obtained by means of discrete non-planar (using arbitrary small increments, see Appendix E) and planar (traditional analysis[45,49]) methods, and a third one is computed after solving the ODE in equation (4.5). The accuracy of these near-instantaneous procedures is then verified by comparing their predictions with the most accurate analysis available using the full non-planar model of RICM[95] requiring ~ 1 h of computation time (non-planar fit in Fig. 4.6a-c). Figure 4.6d clearly indicates that the continuous approach of the ODE method produces the best results with an error that does not have a tendency to increase as the reconstructed height increases and, in general, is smaller than 30 nm (black dashed line) over the entire range of intensities analyzed (essentially including all available fringes up to the 30th, 22nd, and 17th fringes for the results in Figs. 4.6a, 4.6b, and 4.6c, respectively). Of the discrete approaches, only the non-planar formulation maintains a similar degree of accuracy for a significant portion of the reconstructed heights, although the error increases to about 100 nm (black dotted line) at the end. For the discrete planar method, the error can grow quickly and even exponentially (the contour is underpredicted), especially when errors are larger than 100 nm. This description of the error closely resembles the behavior observed in simulated systems (see Appendix H).

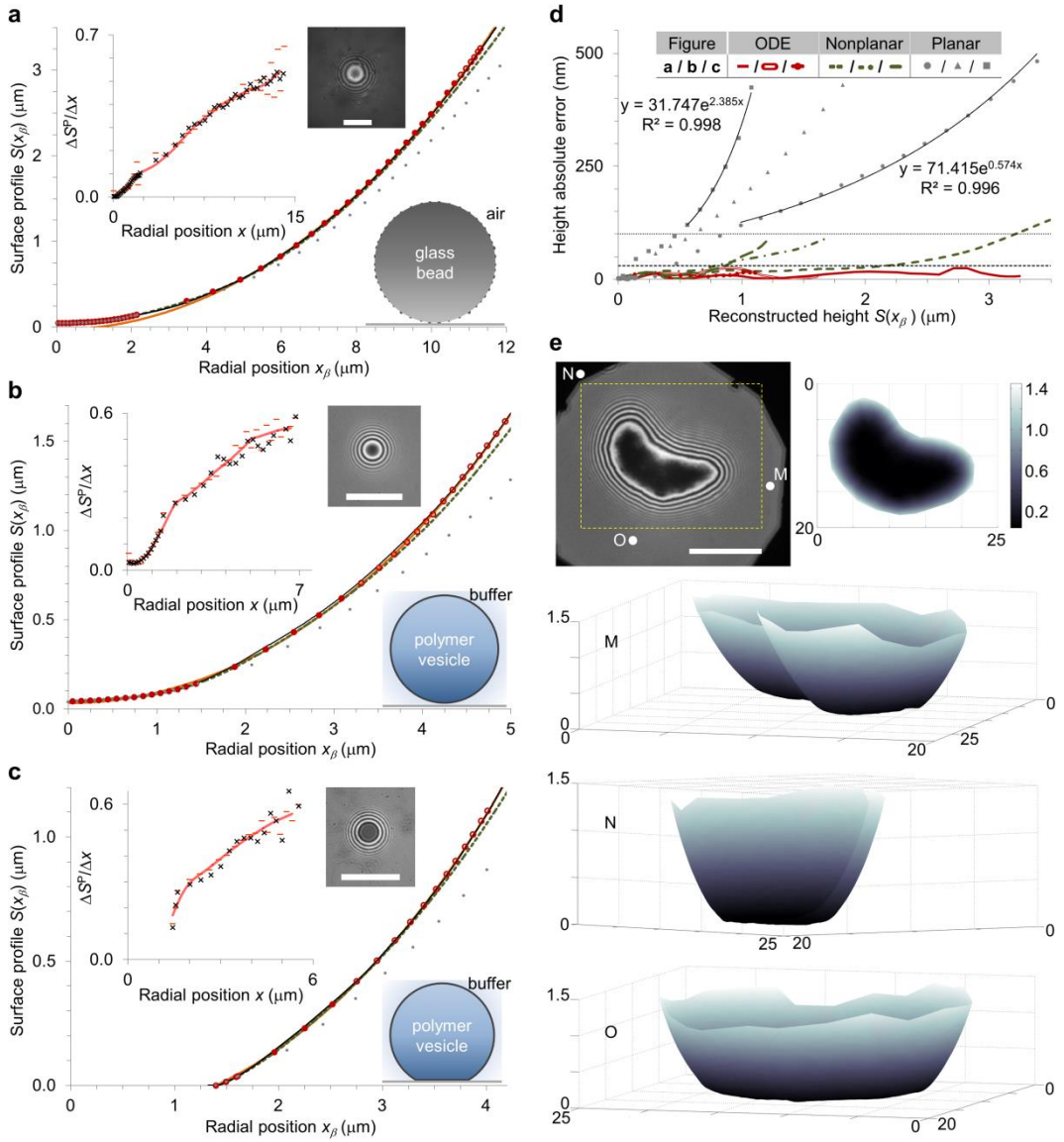

Figure 4.6. Near-instantaneous surface profile reconstruction. Detailed surface profile reconstruction of a glass bead in air **(a)** and polymer vesicles in buffer solution hovering next to the substrate **(b)** and in contact with the substrate **(c)**; insets present the corresponding RICM images (10 μm scale bars), schematic representations of the system, and $\Delta S^P/\Delta x$ versus x from a simulated non-planar fit (black exes) to experimental data (light red symbols/line, without/with smoothing). Four different procedures (listed in increasing order of accuracy) are used to reconstruct the bottom shape of these specimens: discrete planar (gray dots) and non-planar (dashed green line) methods, continuous ODE (closed/open red circles, NRL/non-NRL) approach, and non-planar fit (thin black line). A sphere profile (thick orange line) is fitted to selected reconstructed heights from the ODE method and the non-planar fit is used to define the expected surface profile so that the error of the other procedures can be quantified **(d)**. **(e)** A three-dimensional reconstruction of the bottom shape of a non-symmetric polymer vesicle hovering next to the substrate (~ 37 nm) as observed from three different points of view approximately located at M, N, and O in the RICM image, with the corresponding bottom view also shown; heights in the color bar and positions are given in microns, 10 μm scale bar in RICM image.

4.4 Discussion

Fundamental quantitative descriptors of an object's deformation can be easily obtained from the reconstructed profiles. As symmetry in the RICM images and bright field observation suggest that the systems in Fig. 4.6a-c adopt an overall spherical shape, fitting the predicted contours based on a spherical geometry yields estimated radii, R^{sphere}, and height values at the center of the symmetric interferograms, S_0^{sphere} (see Appendix I). R^{sphere} of 21.13, 8.51, and 7.12 μm for the glass bead, suspended vesicle, and vesicle in contact with the substrate, respectively, are in close agreement with corresponding values of 21.55, 8.38, and 7.23 μm measured directly from the bright field images, confirming an overall spherical shape (truncated sphere, actually, for the vesicle in contact, as assumed theoretically[99,100] and shown with confocal microscopy[7]). S_0^{sphere} values determined from the fitting provide from qualitative to quantitative information on each particular case. For the glass bead, RICM shows a finite separation distance of 49 ± 1 nm between particle and substrate, likely attributable to surface roughness[40,76,101,102], which compared with a negative S_0^{sphere} of –22.6 nm points to significant deviations from a perfectly spherical geometry at the nanoscale. An approximately spherical shape is maintained by the vesicle hovering near the substrate with deformation only observed within 250 nm above the glass, as indicated by the spherical fitting and a positive S_0^{sphere} of 32.2 nm close to that measured directly from RICM (41 ± 1 nm). For the vesicle in contact, a negative S_0^{sphere} of –138.2 nm allows the calculation of a 1.396 μm contact radius and 11.3 ° contact angle based on a truncated sphere geometry, in excellent agreement with the corresponding measurements from RICM (1.4 μm and 9.9 ° at a height of 7 nm). A contact radius to vesicle radius ratio of ~ 0.2 is close to previous reported values for similar shell polymerized vesicles in contact with a glass substrate[7].

Material deformation of soft micron-sized objects at surfaces is fundamentally important in a host of fields, but these effects have proven challenging to probe experimentally. It has long been appreciated that RICM enables the vicinity of a contact region between a microscopic object and a bounding surface to be characterized with nanometric resolution, but a complete accurate implementation of the technique to study dynamic phenomena has been challenging. The analysis of RICM interferograms introduced here overcomes many of these limitations, simultaneously incorporating all fringes available from the set-up resolution in a fast and accurate reconstruction of the non-contact regime surface profiles. Our results validate the method under diverse experimental conditions (air/aqueous media) and different characteristics

of the reflecting surface (smooth, soft polymer vesicle membrane versus rougher, solid glass bead), and Fig. 4.6e clearly indicates that it is in general applicable to arbitrarily-shaped convex objects. In addition, RICM experiments reveal topologically complex local deformations and contact phenomena relevant to virtually all adhesion models. The finding of various scenarios at the micro scale after dry/wet deposition of PSL particles on a glass substrate is in qualitative agreement with recent results that show how different deposition media affect the particle removal efficiency, a fact attributed to plastic deformation of particles caused by capillary forces[103]. Even more significant is the direct observation of femtoliter-scale capillary condensation dynamics underneath micron-sized particles, believed to be unique given that capillary condensation have only been directly observed using environmental SEM[104,105] and studied with the surface forces apparatus,[106,107] although employing two crossed cylindrical mica surfaces with very large radii of curvature (~ 1 – 2 cm). This unparalleled view of the particle-substrate interface offered by RICM reveals new details corresponding to more realistic conditions (different particle deposition scenarios, humidity effects, and accurate contour reconstruction) while potentially enabling near real-time analysis of ensembles containing hundreds of particles near surfaces so that statistical/probabilistic behavior can be realistically captured.

CHAPTER V
INTERFERENCE-BASED MEASUREMENTS ON MICROSPHERES: ROUGHNESS, DIAMETER AND LOCAL CURVATURE DETERMINATION

5.1 Overview

Accurate measurements of roughness and size of microspheres are fundamentally important in colloid science, drug delivery and biomedical applications, but complex instrumentation used might be of limited accessibility making it difficult to obtain statistically significant data. Therefore, the implementation of interference-based characterization techniques capable of simultaneously measure micrometer-sized particles and nanometer-scale features with high temporal resolution in simple setups offers a significant advantage. Here interferograms obtained from microspheres observed using reflection interference contrast microscopy (RICM) are analyzed with novel methods that allow accurate particle characterization, while taking into account roughness effects. By means of a theoretical and computational framework, surface roughness is studied and correlated to measurable visibility changes in RICM interferograms that can also be incorporated in improved measurements of separation distances between surfaces. Microsphere size determination from fringe spacing is optimized yielding relative errors typically less than 1% and intensities corresponding to the closest particle-substrate contact region are analyzed for measuring local radii of curvature and separation distances that are studied in connection with surface roughness. Lastly, the analysis of hundreds of microspheres is performed to illustrate RICM capabilities for particle characterization of statistical significance.

5.2 Introduction

Fabrication of microspheres with certain dimensions and surface specifications plays a significant role in drug delivery and biomedical applications[108-111]. Also, in the increasingly popular colloidal probe technique[21,40,90,112], accurate measurements of force interactions require determination of size, local curvature and roughness of the microsphere acting as a probe. In these scenarios, microsphere characterization is mostly done using both scanning electron microscopy (SEM) and atomic force microscopy (AFM) in a complementary way: while SEM magnification range provides visual assessment of the surface roughness and estimation of

microsphere size (relative error ~ 1%), AFM can be used for quantification of the nano-scale topography and local curvature in small scanning areas[1,73,74,113]. Although accurate measurements can be obtained with these techniques, their complex instrumentation represents limited accessibility for researchers and also an important constraint when hundreds of measurements are required for proper statistical characterization of particle samples. Therefore, the implementation of relatively simple characterization techniques capable of simultaneously measure micrometer-sized particles and nanometer-scale features offers a significant advantage.

Interference-based techniques are known for their setup simplicity and practical use while offering up to angstrom/microsecond-scale resolution[14,15]. However, the accurate use of interference for the study of microscopic objects has been difficult to achieve because most setups and analysis methods are ideal for planar-like geometries[14,17-20]. Here, interferograms obtained from microspheres observed using reflection interference contrast microscopy (RICM)[45,48,49] are analyzed following recently developed methods that allow accurate investigation of their geometry[114]. These quantitative measurements are studied for simultaneous surface roughness, particle size and local curvature determination, while taking into account roughness effects not considered previously.

As a result, a simplified non-planar model of RICM[114] has been enhanced to include surface roughness and, by means of a theoretical framework and computational methods, a relationship between the standard deviation of surface heights and the fringe visibility of a rough object relative to the fringe visibility of the corresponding smooth surface has been specifically determined for the RICM setup. In addition, these visibility changes have been included in the construction of the theoretical curves used for measurement of separation distances between surfaces when assuming planar parallel interfaces. We specifically consider the implementation of these advancements in the experimental RICM analysis of microspheres in close proximity to the substrate (< 200 nm), where methods are optimized for accurate diameter measurements (relative error typically < 1%) using fringe spacing orders that capture the overall spherical geometry without the influence of roughness. In contrast, measured visibility changes attributed to surface roughness become relevant for particle-substrate separation distance measurements that are studied in connection with surface roughness when contact occurs; also, the local radius of curvature is determined for the closest part of the microsphere to the substrate. Finally, these methods are implemented in the analysis of hundreds of microspheres to illustrate their capabilities for particle characterization of statistical significance.

5.3 Results

5.3.1 Surface roughness effects on RICM interferograms

Our approach uses geometrical optics and is intended to provide nanometer-scale roughness information about curved microscopic objects near a smooth and transparent substrate. Therefore, a simplified non-planar model of RICM image formation[114] is considered, where the smooth (that is, mean) surface profile of the object $S(x_\beta)$ presents local nanometer-scale variations $Z(x_\beta)$ that represent surface roughness, see Fig. 5.1a. This allows the computation of the intensity at position x, $I(x)$, in terms of a modified optical path length difference *OPLD* (term in square brackets) expressed as a function of geometric parameters defined at position x_β due to non-planar effects[114], as follows.

$$I(x) = I_1 + I_2 + 2\sqrt{I_1 I_2}\cos\left(\frac{2\pi}{\lambda}\left[2n_1\left(S(x_\beta) + Z(x_\beta)\frac{\cos(\theta_R+\beta)}{\cos(\theta_R)}\right)\frac{\cos^2(\theta_R)}{\cos(\theta_R+\beta)}\right] + \delta\right) \quad (5.1)$$

Here, β is the inclination angle of the smooth non-planar interface at x_β relative to the horizontal plane, θ_R is the angle of reflection at $S(x_\beta)$ and its value depends on the reflected light regime that applies (normal or non-normal)[114], λ = 546 nm is the wavelength of the illuminating light (only monochromatic green light is considered here), n_1 is the refractive index of layer 1 (L1), and δ accounts for a phase shift of π if the refractive index of the object is higher than the index of the medium. However, equation (5.1) in its current form is of limited practical use because RICM images with pixel sizes of 100x100 nm^2 or larger do not reveal specific single effects of small nanometer-scale roughness, an even more significant fact when intensity profiles are obtained from an average over rather large areas (for instance, when performing a circular average in a concentric and symmetric interferogram). Consequently, we seek to determine ensemble average effects of surface roughness that are measurable in RICM interferograms.

It has been shown that fringe visibility, $\upsilon = (I_{max} - I_{min})/(I_{max} + I_{min})$ where I_{max} and I_{min} are the maximum and minimum intensities of the interference fringes, is affected by the root-mean-square surface roughness, σ, in several different interferometers and theoretical relationships between υ and σ have been determined in each particular case[37]. Such relationships can be obtained by following an ensemble average approach[115], which, in our case, would provide a specific mapping between υ and σ applicable to the RICM technique. To envision this,

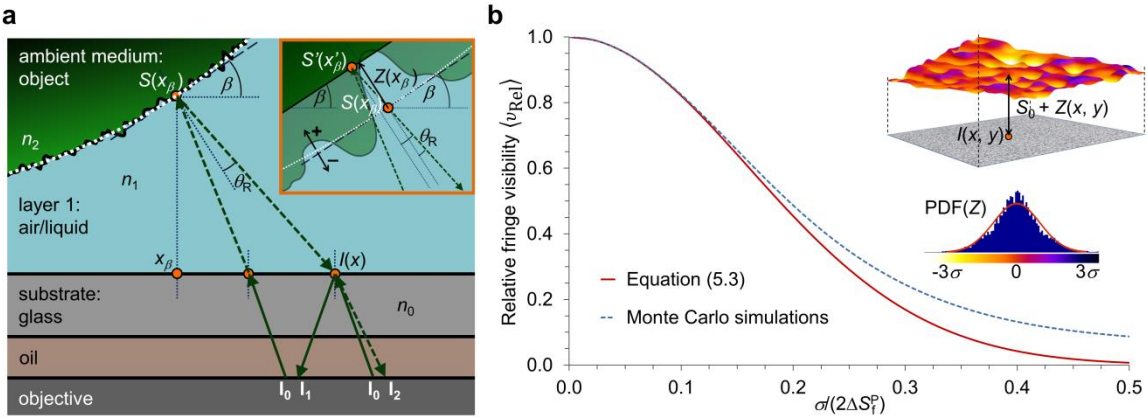

Figure 5.1. Surface roughness effects on RICM interferograms. (a) Simplified non-planar RICM image formation model including surface roughness. When a single set of complementary rays $\mathbf{I_0}$ interfere to produce the intensity $I(x)$, approximations are needed in the local geometry at $S(x_\beta)$ to model the reflection from the rough non-planar interface as shown in the inset. First, the reflection angle θ_R is considered to be determined by the inclination angle β of the smooth non-planar interface at x_β and, following the normal to the surface, a new wedge-like geometry with inclination angle β is defined at a distance $Z(x_\beta)$ apart from $S(x_\beta)$. Second, ray $\mathbf{I_2}$, which would have been reflected at $S(x_\beta)$ in the smooth case, is now reflected back from the wedge geometry at $S'(x'_\beta) = S(x_\beta) + Z(x_\beta)\cos(\theta_R + \beta)/\cos(\theta_R)$ disregarding the presence of the original surface. **(b)** Using an ensemble average approach, it is determined that the relative visibility of fringes in RICM interferograms decreases with surface roughness, and a mapping between the two variables is established theoretically and by performing Monte Carlo simulations for surfaces with a Gaussian probability density function (PDF) of heights (inset).

the following assumptions are made: first, $Z(x_\beta)$ represents local surface variations that are small when compared to λ; second, the correlation length of the surface roughness is smaller than the fringe spacing so that σ only induce a change in υ and not a change in the interference pattern; third, the ensemble average is performed along positions where $S(x_\beta)\cos^2(\theta_R)/\cos(\theta_R + \beta)$ remains constant; and fourth, to facilitate analytical mappings, $Z(x_\beta)$ follows a Gaussian probability distribution with mean zero and standard deviation σ. Then, we obtain an ensemble average of intensities $\langle I(x)\rangle$ from equation (5.1) (see Appendix J).

$$\langle I(x)\rangle = I_1 + I_2 + 2\sqrt{I_1 I_2}\, e^{-2(\pi\cos(\theta_R)[2n_1\sigma/\lambda])^2}\cos\left(\frac{2\pi}{\lambda}\left[2n_1 S(x_\beta)\frac{\cos^2(\theta_R)}{\cos(\theta_R+\beta)}\right] + \delta\right) \qquad (5.2)$$

Here, σ is shown to only affect the amplitude of the intensities through an exponential function that inherits the geometry and setup dependent parameter θ_R, and a term in square brackets that can be expressed as $2n_1\sigma/\lambda = \sigma/(2\Delta S^P_f)$, where ΔS^P_f is the constant height increment between two

consecutive fringes when planar parallel interfaces and normal incidence light are assumed ($x = x_\beta$ and $\beta = \theta_R = 0$)[114]. Thus, equation (5.2) indicates that, under the assumptions made, roughness effects are effectively decoupled from the phase term that provides the mean or smooth geometry information. By using the definition of visibility and taking as a reference the corresponding smooth surface, the following relationship is found between a relative ensemble average visibility $\langle v_{Rel} \rangle$ and σ (see Appendix K).

$$\langle v_{Rel} \rangle = e^{-2(\pi \cos(\theta_R)[\sigma/(2\Delta S_f^P)])^2} \tag{5.3}$$

To verify this relationship, we model a rough planar surface with a Gaussian distribution of heights $Z(x, y)$ and place it parallel to the smooth substrate at a separation distance S_0; then, use equation (5.1) to evaluate single intensities $I(x, y)$ corresponding to $S_0 + Z(x, y)$ over the entire surface (see insets in Fig. 5.1b), so that the ensemble average intensity $\langle I \rangle$ can be computed in what we describe as a Monte Carlo method, see Appendix K. By varying S_0, under different refractive index conditions, $\langle v_{Rel} \rangle$ can be computed from the fringes in the $\langle I \rangle$ versus S_0 curve, and this is repeated for different σ to obtain the mapping between $\langle v_{Rel} \rangle$ and $\sigma/(2\Delta S_f^P)$, see Fig 5.1b. It can be seen that both equation (5.3) and the Monte Carlo simulations present similar exponential decay behavior and are in excellent quantitative agreement for small roughness of the surface. However, a significant difference is observed as σ increases because, eventually, height variations become too large (that is, the first assumption is no longer valid). To determine when and how this happens, we notice that Z ranges approximately from -4σ to 4σ, where an amplitude of 8σ in height (peak to valley variations) covers a full period ($2\Delta S_f^P$) of the cosine function in equation (5.1) when $\sigma/(2\Delta S_f^P) = 1/8 = 0.125$. Effectively, for $\sigma/(2\Delta S_f^P) > 0.125$ ($\langle v_{Rel} \rangle < 0.735$) relative differences between the two mappings quickly increase beyond 1% as the ensemble average of intensities becomes more complex with heights involving two or more periods in equation (5.1), an effect not properly captured by equation (5.3). Therefore, we expect our analytical expressions to provide quantitative results for $\langle v_{Rel} \rangle \geq 0.65$ where $\sigma/(2\Delta S_f^P) < 0.15$ with a relative difference between the two mappings no larger than 2% (a maximum amplitude of 8σ in Z can be considered as probabilistically conservative).

5.3.2 Surface roughness and separation distance measurements

Now we focus our attention on the theoretical ensemble-average-intensity versus separation distance curve, $\langle I \rangle$ versus S_0 (where $\beta = \theta_R = 0$), with the aim of understanding roughness effects on RICM separation distance measurements between surfaces. When S_0 is varied between a surface with roughness σ and a smooth substrate, there is a minimum average separation distance, $\langle S_0 \rangle^C$, that can be achieved due to the presence of roughness at contact[40,116-118]. For planar surfaces, $\langle S_0 \rangle^C$ corresponds to the roughness peak distribution, about 3-4 times σ for a Gaussian surface, a range reported experimentally for a large microsphere-planar substrate configuration[118]; for small microspheres, however, curvature effects at the point of contact are expected to lower this range. Therefore and in order to illustrate our approach, we consider the relationship between $\langle S_0 \rangle^C$ and σ given by $\langle S_0 \rangle^C = \sqrt{5}\sigma$, which is derived from the subcritical case of an unbinding membrane in a short-ranged potential and is equivalent to the hard-wall case[119]. These considerations indicate that separation distance measurements at contact can also be used to infer the roughness of a surface (in addition to fringe visibility), as long as $\langle I \rangle_{Rough}$ versus S_0 is properly determined and the asperities do not suffer significant contact deformation (low applied loads).

Hence, the construction of the mapping $\langle I \rangle_{Rough}$ versus S_0 is performed in two steps. First, for $S_0 \geq \langle S_0 \rangle^C$, the surfaces likely exist in a non-contact regime and the simplified non-planar model with roughness effects in equation (5.2) and Monte Carlo simulations from equation (5.1) properly describe the shape of the $\langle I \rangle_{Rough}$ versus S_0 curve by introducing a decrease in fringe visibility, see Fig. 5.2a. Second, although contact is expected at $S_0 = \langle S_0 \rangle^C$, given the statistical nature of the rough surface and the fact that $\langle S_0 \rangle^C$ represents an average at contact, it is possible to locally measure $\langle I \rangle$ values corresponding to $S_0 < \langle S_0 \rangle^C$. To account for this, $\sigma = S_0/\sqrt{5}$ is substituted in equation (5.2) to construct a mapping from S_0 to $\langle I \rangle_{Rough}$ at contact. This mapping, presented in Fig. 5.2a, provides the $\langle I \rangle_{Rough}$ versus S_0 curve for $0 \leq S_0 < \langle S_0 \rangle^C$ (a reasonable supplement to the non-contact regime), meaning that intensities within this interval are interpreted as being originated from a continuously smoother surface as S_0 decreases and, consequently, the rough and smooth curve converge and both share the same $\langle I(0) \rangle$.

An important observation in Fig. 5.2a is that the roughness effects on the $\langle I \rangle_{Rough}$ versus S_0 curve previously described can be emulated by properly scaling the corresponding smooth

curve according to the visibility given by equation (5.3) and the fact that the intensity changes $\Delta I_{min}/\Delta I_{max} = 1$. This implies that the $\langle I \rangle$ versus S_0 mapping obtained from the theory for stratified planar structures[29], including illumination numerical aperture (INA) and multiple layer effects, can also be scaled to obtain a more accurate $\langle I \rangle_{Rough}$ versus S_0 providing that the visibility change due to roughness is known (for instance, using equation (5.3) while incorporating an improved ΔS^{P}_{f} value). Such curves are presented in Fig. 5.2b for two different INAs, including the smallest INA typically available of 0.48 (used here from now on). The improvement obtained is significant and especially evident for large separations (> ~80 nm) and large INAs.

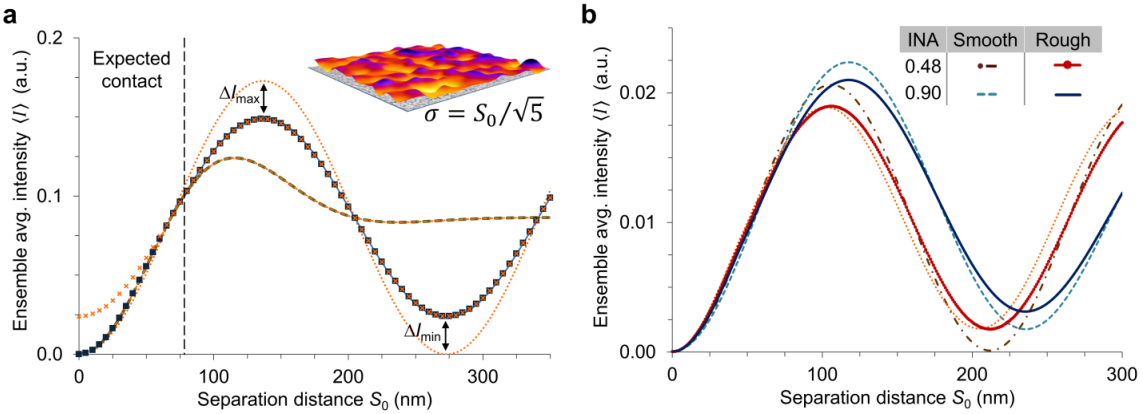

Figure 5.2. Surface roughness and separation distance measurements. (a) Visibility changes due to a rough surface (σ = 35 nm) can be appreciated on the intensity versus separation distance curve obtained from equation (5.2) (dark blue squares) and Monte Carlo simulations (continuous blue line). The portion of the curve where the surfaces are expected to be in hard-wall contact is computed from equation (5.2) using a variable σ (discontinuous green line, full curve shown) given by the relationship in the inset. Notice that by scaling the smooth curve (dotted orange line), visibility changes (orange exes) and the curve at expected contact (dashed orange line) can be emulated. Curves correspond to glass/air/surface with refractive indices of 1.53/1/1.55, respectively. **(b)** Improved RICM separation distance measurements can be obtained by constructing intensity versus separation distance curves that simultaneously capture roughness and INA effects; for comparison, see the rough curve from equation (5.2) (dotted orange line). The system presented is composed of glass/water/surface with corresponding refractive indices of 1.53/1.333/1.55, σ = 20 nm, and 1.25 numerical aperture.

5.3.3 Microsphere size and fringe visibility effects

The practical implementation of surface roughness measurements using RICM depends on computing the fringe visibility of the rough surface relative to the fringe visibility of the corresponding smooth surface. In general, an experimental RICM interferogram provides the

fringe visibility of a rough object and a way of determining the visibility of the corresponding smooth surface is as follows. First, for an arbitrarily shaped convex object, its geometry can be accurately reconstructed with nanometer-scale resolution[114], that is, the average or smooth profile can be found. Then, this reconstructed geometry is used to simulate the corresponding interferogram by means of the complete non-planar interface image formation theory of RICM[95], from which the visibility of the smooth surface is computed, and, lastly, the relative visibility is measured and linked to the object roughness. This approach is employed here for the particular case of microspheres, as described in Fig. 5.3. Therefore, this section deals with implementing computational methods that facilitate accurate quantification of the information contained in RICM images from microspheres in the range 6-60 μm diameter, especially finding the interferogram center, using interference fringes for accurate particle size determination and identifying important visibility effects that must be taken into account in roughness measurements.

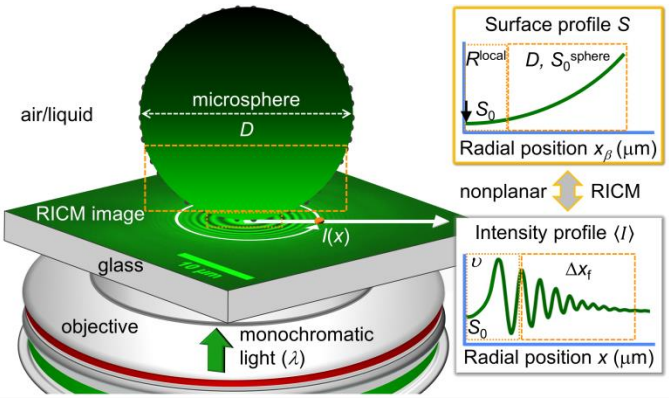

Figure 5.3. Schematic of RICM analysis of microspheres. Rough microspheres near a transparent smooth substrate can be studied with RICM to obtain particle size and surface roughness information. First, an intensity profile with representative ensemble average intensities over radial positions is obtained after performing a circular average, see white arrows on RICM image. The intensity profile is then split for analysis, where fringe spacing Δx_f data in the dashed box correspond to large areas on the microsphere surface and are appropriate to determine its overall spherical geometry (diameter D and separation distance S_0^{sphere}, using simplified non-planar RICM). The remaining intensities, from the center and including up to the first peak and valley (dotted box) provide detailed information about the local radius of curvature, R^{local}, and microsphere roughness in the form of fringe visibility, υ, and the separation distance, S_0, between the two surfaces when in contact.

The analysis of a concentric and symmetric interferogram begins with the precise determination of its center, so that the circular average properly provides a profile of intensity $\langle I \rangle$ versus radial position x. By employing computational methods, it has been found that sub-pixel resolution can be achieved in our custom made routines for center finding and, over the particle range studied here, the average error observed was 7.3 ± 4.8 nm with a maximum error of 21.2 nm, see Fig. 5.4a. Then, fringe spacing data Δx_f collected from the averaged intensity profile is used to construct the mapping $\Delta S^P_f/\Delta x_f$ versus x, see Fig. 5.4b, from which the smooth surface profile can be reconstructed[114]. For microspheres, assuming a perfect sphere of diameter D with a separation distance S_0^{sphere} from the substrate, we use a relationship derived for this particular geometry by means of the simplified non-planar model of RICM, see Appendix L.

$$x = S_0^{\text{sphere}} \tan(\beta + \theta_R) + D\big(\sin(\beta) + \big(1 - \cos(\beta)\big)\tan(\beta + \theta_R)\big)/2 \tag{5.4}$$

This equation implicitly contains the mapping from x to $\sin(\beta)\cos(\theta_R)$ that is equivalent to the mapping from x to $\Delta S^P_f/\Delta x_f$, therefore, providing a way of directly finding the geometric parameters D and S_0^{sphere} by fitting the experimental data with equation (5.4), see Fig 5.4b. The fitting is performed in two steps, first, assuming that $S_0^{\text{sphere}} = 0$ to obtain an initial estimate for D and, second, varying both D and S_0^{sphere} to find the best fit using non-linear least-squares. Notice that not all $\Delta S^P_f/\Delta x_f$ values are used in the fitting, where the first two data points are excluded because they are expected to contain precise local topographical information and/or deformation and likely deviate from the overall sphere geometry[114]; on the other hand, including too many data points reduces accuracy because of the continuously increasing variability observed with radial position, see Fig 5.4b. To determine the optimum range of fringe spacing orders to be included, starting from the third Δx_f^3, experimental measurements of the standard reference material (SRM) 1961 (nominal 30 μm diameter polystyrene spheres) in aqueous medium are performed, along with simulations of a similar system using full non-planar RICM, see Fig 5.4c. It is found that both experiments and simulations point to a specific range of fringe spacing orders (Δx_f^3-Δx_f^{12}) where the magnitude of the size measurement error and its variability are minimized, a result that can be extended to the range of microsphere sizes considered here, see Fig 5.4d.

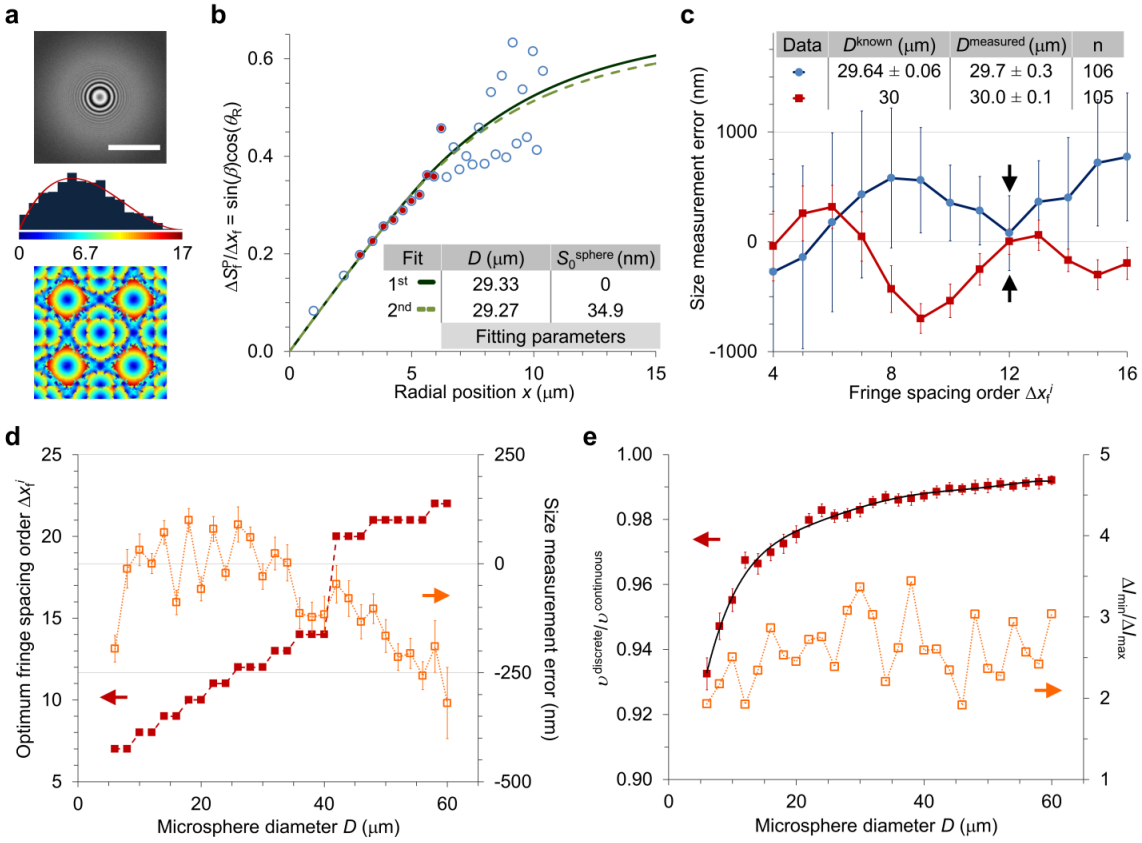

Figure 5.4. Microsphere size and fringe visibility effects. (a) 1000 simulated RICM images of a 20 μm diameter sphere (like the one shown on top; 10 μm scale bar), where the interferogram center is randomly placed within the central pixel, are used to obtain a characterization of the error (beta distribution in the middle; minimum, average and maximum error given in nm) when employing methods for accurately determining the center of the interferograms with sub-pixel resolution (error within central pixel shown at bottom; 100x100 nm). **(b)** Accurate measurements of microsphere size are performed by fitting $\Delta S^{P}_{f}/\Delta x_{f}$ data (open blue circles) in a selected range (closed red circles) by means of equation (5.4), as seen here for a SRM 1961 particle in aqueous medium. **(c)** The upper limit of the optimum range (indicated by arrows) for the fitting is determined from the minimum error in particle size measured from experimental (blue line with circles) and simulated (red line with squares) microspheres of known dimensions. **(d)** Using simulations alone, the result in (c) is extended to the range of microspheres studied and the expected error is quantified. **(e)** A significant decrease in fringe visibility, measured at the first peak and valley of the intensity profile, results from pixilation in the simulated RICM images; although a sixth order polynomial (black line) describes the relative decrease in visibility, the intensity changes that take place appear to be uncorrelated with particle size. All systems used for simulations are composed of glass/water/sphere with corresponding refractive indices 1.53/1.33/1.55, and 1.25 numerical aperture; the spheres are 50 nm above the substrate except in (c), where separation distances from 0 to 200 nm are considered. Error bars represent one standard deviation.

An important feature of our computations using full non-planar RICM is that entire two-dimensional images are simulated, so that pixilation, noise and variability from the center finding are taken into account when the circular average is performed and a discrete one dimensional intensity profile is measured. This becomes evident when the visibility of the discrete intensity profile is compared with the visibility of the corresponding continuous profile. The observed decrease in relative visibility due to pixilation is virtually relevant to all particle sizes studied and especially significant for small particles, see Fig. 5.4e. Although a clear trend can be established for the relative decrease in visibility as particles become smaller, the way the intensity changes at the extrema ($\Delta I_{min}/\Delta I_{max}$) seems to be unpredictable. Thus, this effect has to be considered in a case by case basis when computing the visibility of the smooth surface from simulations in roughness measurements.

5.3.4 Surface roughness and local curvature of microspheres

As indicated earlier in Fig. 5.3, a detailed analysis is performed on the ensemble average intensities, $\langle I \rangle_{\text{Rough}}$ versus x, including up to the first measurable peak and valley that are used to compute $\langle v \rangle_{\text{Rough}}$, see Fig. 5.5a. Because, in general, the corresponding local geometry cannot be assumed to be spherical, we use simplified non-planar RICM to analyze the complete interferogram and reconstruct the surface profile while neglecting, at first, roughness effects[114]. The resulting geometry approaches the overall spherical shape (determined from equation (5.4)) for large radial positions and diverges from it in the proximity to the substrate where the local geometry becomes relevant, as seen Fig. 5.5b. Then, a discrete intensity profile $\langle I \rangle_{\text{Smooth}}$ versus x that closely reproduces the fringe spacing of $\langle I \rangle_{\text{Rough}}$ versus x is generated from this arbitrarily-shaped convex geometry and $\langle v \rangle_{\text{Smooth}}$ is determined from the corresponding first peak and valley used to obtain $\langle v \rangle_{\text{Rough}}$ (notice that only this specific portion of the intensity profile needs to be simulated). The computed relative visibility $\langle v \rangle_{\text{Rel}} = \langle v \rangle_{\text{Rough}}/\langle v \rangle_{\text{Smooth}}$ provides a value of σ, by means of equation (5.3), and the visibility change required to construct the appropriate curve for separation distance measurements (with $\Delta I_{min}/\Delta I_{max} = 1$) including roughness effects, see Fig. 5.5a. Consequently, for particles in contact, $\langle S_0 \rangle^{C}$ can be measured and studied in connection with the roughness observed from visibility.

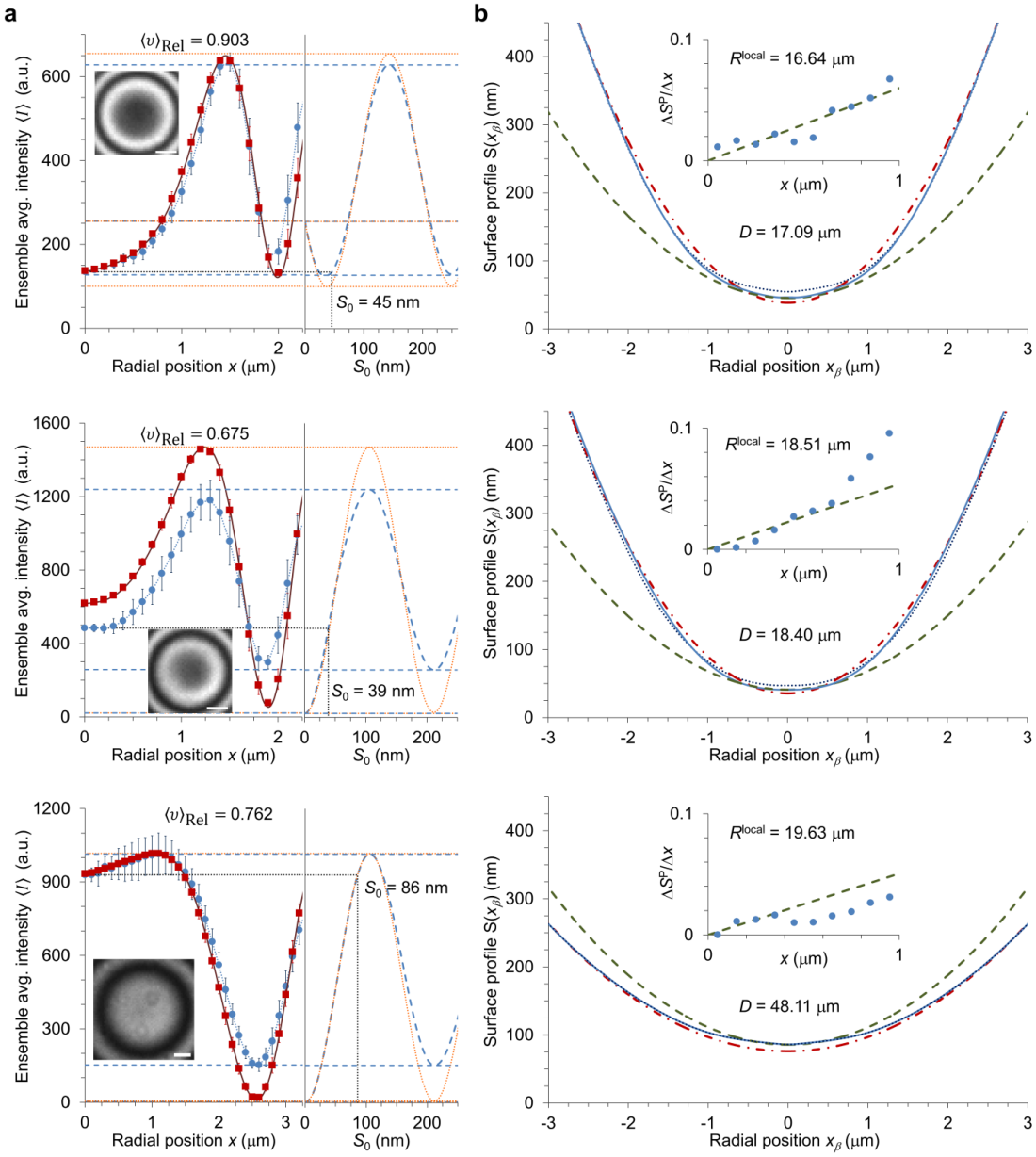

Figure 5.5. Surface roughness and local curvature of microspheres. (a) Experimental (rough; blue circles) and simulated (smooth; continuous/discrete: red line/squares) intensity profiles corresponding to a polymer vesicle (top), PSL microsphere (middle), and glass bead (bottom) in aqueous medium and near the substrate are plotted (left) in the same scale, based on background intensities, to illustrate the differences in visibility due to roughness and the corresponding smooth (dotted orange line) and rough (dashed blue line) curves for separation distance measurements (right). **(b)** The surface profile of the microspheres is reconstructed using simplified non-planar (without/with roughness: dotted/continuous blue line) and two spherical fittings are shown: the overall particle diameter (dash-dot red line) and local radius of curvature at the bottom (green dashed line), determined by fitting $\Delta S^P/\Delta x$ data (inset; blue circles) obtained by means of the rough separation distance curve in (a). The components of the systems studied are glass substrate, buffer, PSL particle, glass particle, polymer membrane, and sucrose solution with refractive indices of 1.53, 1.334, 1.59, 1.51, 1.51, and 1.351 respectively; 1.25 numerical aperture used.

Roughness effects can now be incorporated in the construction of the $\Delta S^P/\Delta x$ versus x mapping when analyzing neighboring intensities located before the first intensity extrema, in what has been previously called as the first transformation[114]. By using the corresponding branch of the $\langle I \rangle_{Rough}$ versus S_0 mapping, seen in Fig. 5.5a, the height increments for planar parallel interfaces ΔS^P for these intensities can be computed and divided by the constant positional increment Δx (100 nm in our setup) to obtain $\Delta S^P/\Delta x$ versus x, see insets in Fig. 5.5b. Therefore, a more accurate reconstruction of the surface profile can be achieved for cases where visibility changes affect these intensities, especially within 100 nm above the glass substrate, see Fig. 5.5b. Here we incorporate and evaluate these corrections in the measurement of an arbitrarily defined local radius of curvature, R^{local}, as the radius of the spherical geometry that provides the best fit to the first few $\Delta S^P/\Delta x$ values ($x < 1$ μm) resulting from the first transformation. To find R^{local}, a simplified version of equation (5.4) is employed, where only normal reflected light is considered ($\theta_R = 0$), see insets in Fig. 5.5b.

Table 5.1 summarizes the results obtained when two monodisperse samples of different types of microspheres are analyzed as previously described, providing accurate information about their diameter, local radius of curvature, roughness from fringe visibility and separation distance at contact with the substrate.

Table 5.1. RICM measurements on monodisperese microspheres samples

Particles (sample size)	Diameter (μm)	R^{local} (μm)	S_0 (nm)	$\langle v \rangle_{Rel}$	$\Delta I_{min}/\Delta I_{max}$	σ (nm)
PSL15(193)	15.13 ± 2.08	16.18 ± 6.65	39.7 ± 3.4	0.737 ± 0.049	0.65 ± 0.49	26.3 ± 2.9
Glass15 (122)	15.69 ± 2.34	13.99 ± 5.77	40.8 ± 9.4	0.723 ± 0.063	1.92 ± 4.50	27.0 ± 3.7

5.4 Discussion

Differences in relative fringe visibility behavior are evident when microspheres of diverse nature are compared in Fig. 5.5. At first, we analyze the computed $\langle v \rangle_{Rel}$ in terms of surface roughness, as suggested by our approach based on geometrical optics and ensemble average of intensities, and compare the σ obtained with the corresponding measured separation distances S_0, under the

assumption of a Gaussian distribution of surface heights. For the polymer vesicle hovering above the glass (coated with ~4 nm thickness[120,121] bovine serum albumin, BSA), the measured S_0 (~45 nm, close to S_0^{sphere} = 38.4 nm) is consistent with a non-contact scenario according to the 14.9 nm roughness determined from fringe visibility ($S_0 \approx 3\sigma$) and the fact that a contact area is only detected without BSA. A plausible explanation for the roughness observed (of the same magnitude as the 15 nm thickness[85] of the polymer membrane) is that the polymerized shell preserves undulations present in the fluid membrane before polymerization; for instance, bending excitations of ~10 nm root mean square and short wavelength (< 0.5 μm) have been reported in cells[23]. In the case of the PSL microsphere, the separation distance measured (~39 nm, close to 35.5 nm from the spherical fit) points to (expected) contact with the glass when compared to the 29.6 nm of σ ($S_0 \approx 1.3\sigma$); however, for a particle under low loads, it appears to be too close to the substrate indicating a poor agreement between σ and S_0 as measured from RICM. In contrast, the large glass bead exhibits ~86 nm of separation distance (close to S_0^{sphere} = 76.1 nm) in good agreement with a surface roughness of 24.7 nm from $\langle v \rangle_{\text{Rel}}$ ($S_0 \approx 3.5\sigma$). Although roughness from fringe visibility reported for the vesicle and glass bead seems reasonable and in accordance with the separation distance between the specimens and the substrate, additional factors discussed in the following paragraphs allow a better understanding of discrepancies in the PSL particle measurements.

An important observation in Fig 5.5a is that the intensity changes at the first peak and valley are highly asymmetric ($\Delta I_{\text{min}}/\Delta I_{\text{max}} >> 1$) for the glass bead, contrary to the vesicle and, in particular, the PSL microsphere case ($\Delta I_{\text{min}}/\Delta I_{\text{max}} \sim 0.8$). Consequently, the first branches of the rough and smooth curves for separation distance measurements in the glass bead necessarily coincide and a particular scaling is required for subsequent branches; in other words, intensities near the center of the interferogram (x < 0.9 μm) behave as originated from a smooth surface despite the large $\langle v \rangle_{\text{Rel}}$ and S_0 measured that indicate the presence of significant irregularities. This apparent inconsistency can be clarified by taking a closer look at the topography of the particles studied, as seen in Fig. 5.6a-b, where SEM and RICM allow a qualitative assessment of the microspheres' surface. Given the non-homogeneous asperity covered (~11 %) glass bead surface, it is possible to have configurations where the surface is locally smooth around radial position x = 0 and, as x increases, the ensemble average of intensities from the circular average collects roughness information from larger areas (including the asperities actually in contact with the substrate that cause S_0) introducing more representative changes ΔI for the following

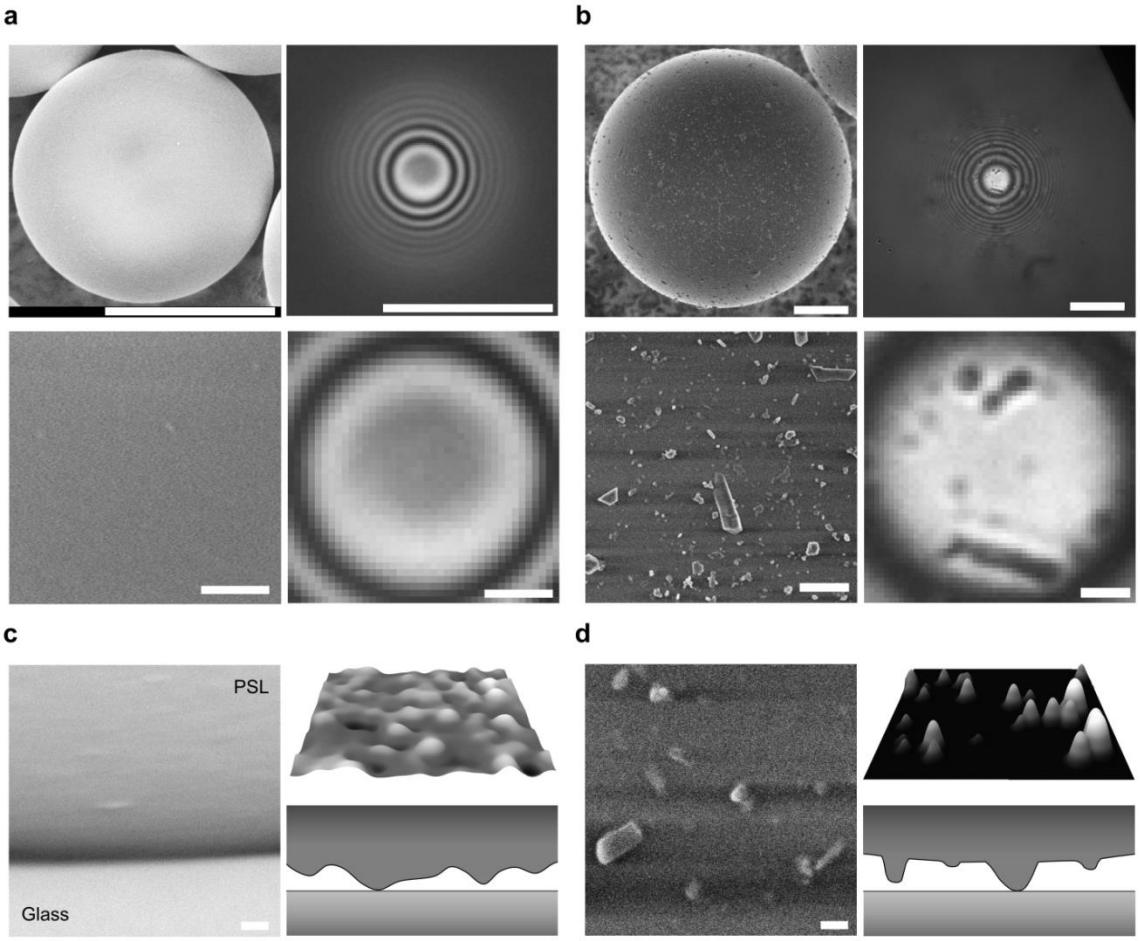

Figure 5.6. SEM and RICM qualitative surface roughness analysis of microspheres. PSL **(a)** and glass **(b)** microspheres are observed under SEM (left) and RICM (right) techniques at different length scales (10/1 μm scale bars at top/bottom). Direct SEM observation clearly shows differences in the uniformity of the particles' surface at the micro and nano-scale, where PSL looks highly homogeneous while asperities of various shapes and dimensions give a non-uniform appearance to the glass surface. Similar information can also be inferred from RICM images taken in air where the uniform and clean interferogram of the PSL particle contrasts with the one from the glass bead showing evidence of some of the large features (~1 micron and even smaller). This information for the PSL **(c)** and glass **(d)** microspheres facilitates the formulation of appropriate surface roughness models at the nano-scale relevant at contact and for RICM fringe visibility analysis (right), as verified by SEM observation at the corresponding scale (left, 100 nm scale bar).

intensity extrema, as seen at the bottom of Fig 5.5a. The PSL particle, on the other hand, is fairly uniform with features that smoothly appear over the surface in length scales larger than 100 nm, similar to what is expected for the polymer vesicle membrane. Therefore, Fig. 5.6 allows verifying that a Gaussian roughness model is suitable for the PSL microsphere, as shown in Fig.

5.6c, but a different surface model might be more appropriate to achieve better quantification of σ from $\langle v \rangle_{\mathrm{Rel}}$ for the glass bead, see Fig. 5.6d. More importantly, this discussion reveals that RICM interferograms are also sensitive to surface homogeneity ($\Delta I_{\mathrm{min}}/\Delta I_{\mathrm{max}}$) relative to fringe spacing (typically ~1 μm for the first peak/valley) and emphasizes the highly localized nature of the topographic information embedded at/near the center of the interferogram.

Based on these insights, we now revisit the PSL microsphere in contact with the substrate in Fig. 5.5. Fairly symmetric intensity changes mean that representative surface variations are effectively captured when $\langle v \rangle_{\mathrm{Rel}}$ is measured from radial positions between 1-2 μm involving heights $S(x_\beta) - S_0 > 50$ nm. In addition, the relatively small size of the PSL particle coupled with smooth variations over a few hundreds of nanometers also imply that S_0 is locally determined and, probably, uncorrelated with $\langle v \rangle_{\mathrm{Rel}}$ (in contrast to what happens with the large glass bead). These observations are generally applicable to other microspheres; for instance, the results in Table 5.1 indicate that both PSL (PSL15) and glass (Glass15) particle samples of 15 μm nominal size have similar surface topography as determined from fringe visibility analysis and the separation distance measured, with no correlation observed between σ and S_0 in either case. The main difference between the samples appears to be larger variability present in the Glass15 measurements, with around 5 % of the particles exhibiting indicators of a non-homogeneous surface ($\Delta I_{\mathrm{min}}/\Delta I_{\mathrm{max}} > 5$).

Moving onto larger length scales, RICM capabilities for particle size measurements have long been appreciated, in particular using analysis of limited applicability[40,48] and with more practical measurements only possible by means of correction factors derived from full non-planar RICM[29,95]. The method presented here is quite robust and easy to implement because it is based on a direct and optimized analysis of multiple interference fringes, resulting in relative errors less than 1% for microspheres with diameters between 7 to 60 μm. When smaller particles are analyzed as described here, the exclusion of the first two Δx_{f} values leaves too little information for the fitting, resulting in an increased relative error; therefore, a full analysis to reconstruct the geometry is suggested in these cases, followed by a spherical fitting to determine particle dimensions[114]. In addition to the high nanometer accuracy reported for our method, it also exhibits great precision. For the highly monodisperse SRM 1961 (0.8% coefficient of variation, CV) a consistent 1.1 % CV is obtained, where the slightly higher dispersion is possibly due to S_0^{sphere} being another fitting parameter implicated. For the monodisperse PSL15 microspheres in

Table 5.1, the reported measurements (13.7 % CV) are in excellent agreement with manufacturer's values of 15 μm and 14% CV; though no manufacturer information is available for Glass15, we feel confident about the 14.9 % CV measured by RICM. Finally, the great accuracy and precision achieved in size determination implies that S_0^{sphere} might provide valuable independent information as pointed out before[114]; although individual values could be negative leading to large variability, S_0^{sphere} computed from several measurements seems to represent a characteristic value for a given particle sample (in a similar way S_0 does, see Appendix L).

An additional microscopic measurement reported in Table 5.1 is R^{local}, which is consistently higher than the corresponding microsphere radius for the polymer vesicle, PSL15 and Glass15 samples, in contrast to what is observed for the large glass bead in Fig. 5.5. Therefore, this increase in local curvature seems to occur for small microspheres that are closer to the substrate than the large glass bead, suggesting that it probably originates from elastic deformation due to interactions with the substrate; this is also consistent with R^{local} being larger for PSL15 than for Glass15, a valid comparison given that both samples essentially have the same size distribution. Interestingly, R^{local} is essentially the same whether roughness corrections are included or not (see Appendix L), which is not totally surprising because its computation mainly involve changes between consecutive intensities in the first transformation instead of absolute intensity values.

Although the surface roughness analysis presented here focuses on microspheres that facilitate obtaining ensemble average intensities, it can be applied, in general, to relatively smooth arbitrary convex geometries for which simplified and full non-planar RICM models are currently available[95,114]. Also, the assumption of surface roughness following a Gaussian distribution of heights can be relaxed, given that more appropriate distributions for certain objects (see Fig. 5.6d) can be analyzed, in general, using Monte Carlo simulations. It is important to notice that quantitative analysis of fringe visibility is challenging, because a number of factors such as scattering (expected to increase with σ), absorption and substrate roughness have not been taken into account (for simplicity), while additional errors from the refractive index of the object, focusing, and model shortcomings also come into play. Consequently, there is still room for improvement and for now, our results consistently indicate that $\langle v \rangle_{\text{Rel}}$ is a parameter affected by the object's nano-scale topography in RICM measurements and agreement between surface roughness inferred from $\langle v \rangle_{\text{Rel}}$ and S_0 measurements can only be expected, in general, for large microspheres.

CHAPTER VI
CONCLUSIONS AND RECOMMENDATIONS

6.1 Conclusions

Reflection interference contrast microscopy is a powerful technique for the study of microscopic objects near surfaces, capable of measuring an object's arbitrary convex shape with nanometer-scale resolution, while simultaneously providing information about its nanometer-scale topography and the presence of contact phenomena, if any, with high temporal resolution and in a non-invasive way. Because the methods of analysis developed here are of practical application, RICM has a clear potential for near real-time analysis of ensembles of objects near surfaces so that statistical/probabilistic behavior can be realistically captured.

The most complete non-planar interface image formation theory of RICM was improved with a more precise and general mathematical formulation for intensity calculations. In addition, an important correction was made in the three-dimensional evaluation of the optical path length difference, indicating that simplified fringe spacing analysis is more accurate than what previously thought, especially for large inclinations of the non-planar interface. The improved theory was coupled with a general method to simulate the interference pattern from arbitrary convex geometries with either single or double reflecting layers, revealing that an accurate reconstruction of an object's arbitrary convex shape is possible by fitting its experimental intensity pattern.

A simplified non-planar RICM model was formulated, enabling the identification of normal and non-normal reflected light regimes; these are two complementary regimes of illumination that cover all possible scenarios for interference in arbitrary convex geometries. Based on this simplified model, a significant breakthrough was achieved: data in RICM intensity profiles can be easily transformed to directly provide the inclination angles of the geometry under study so that the surface profile can be accurately reconstructed with an unprecedented nanometer-scale resolution via an appropriate mathematical procedure of fast execution. This innovative analysis of RICM interferograms and the near-instantaneous surface profile reconstruction method are applicable to arbitrarily shaped convex objects under different experimental conditions.

Simple experiments involving the deposition of microspheres on surfaces have revealed the existence of different microscopic scenarios depending on deposition media and unique femtoliter-scale capillary condensation dynamics underneath micron-sized glass beads, thanks to direct observation by RICM. Therefore, RICM's high resolution, set-up simplicity and distinctive non-invasive "view-from-below" perspective can play a significant role in non-traditional fields; for instance, in this case, potentially facilitating particle deposition/resuspension studies under more realistic conditions directly quantifiable.

A theoretical framework and computational methods, based on the idea of ensemble averages of intensities, provided a specific relationship for the RICM set-up between the nanometer-scale topography of a microscopic object and its fringe visibility relative to the fringe visibility of the corresponding smooth surface. Using this principle, experimental RICM interferograms from microspheres can be conveniently analyzed to extract surface roughness information. In addition, visibility changes can be incorporated in improved separation distance measurements, revealing that for small (nominal 15-μm diameter) particles in contact with the substrate, these measurements are determined by the local topography and no correlation was observed with the roughness from fringe visibility analysis.

Precise and accurate measurements of microspheres' size (< 1% relative error) in the range from 7 to 60 μm diameter can be performed by means of an optimized and robust fringe spacing analysis of their RICM interferograms. Consequently, particle size distributions of monodisperse samples can be accurately quantified.

6.2 Recommendations for future work

A natural direction for expansion of the present work would be the study of concave geometries. In this scenario, exact intensity computations represent a significant challenge because it is possible to have multiple contributions to the intensity coming from different regions of a concave geometry, so a consistent indexing based on rays that are reflected back from the object might not be feasible. However, the development of appropriate calculation methods to accurately simulate intensity profiles can provide a valuable tool for understanding the reflection-interference phenomenon in convex geometries, possibly leading to the formulation of simplified models and appropriate surface profile reconstruction methods, as done here for the arbitrary convex geometry case. This would mean the possibility of having a complete set of tools for analysis of RICM images corresponding to diverse geometric configurations of the

reflecting surface and potentially formulating a general way of accurately retrieving arbitrary geometries from their interference patterns.

Interesting and unique contact phenomena presented qualitatively in Chapter IV can be expanded and quantified. Differences observed when water is used as deposition medium can be further investigated to determine any remnants of water; observation of large numbers of particles could reveal the frequency of occurrence of the different deposition scenarios, which can be related to resuspension efficiency with RICM measurements performed on samples before and after resuspension experiments. Moreover, the effect of diverse deposition media with various surface tension and evaporation rates can provide additional insights about the phenomena observed. For the capillary condensation dynamics, short and long term relative humidity effects can be determined; following contact angle and roughness measurements on the glass bead and substrate surfaces, accurate quantification of the water content can be obtained including mathematical modeling of meniscus shape and expected equilibrium configuration. Also, RICM observations before and after resuspension experiments can directly relate capillary condensation with resuspension effeiciency under different conditions, and similar studies with other particle sizes, topography and materials can offer an improved picture of this phenomenon.

The theoretical and computational approaches based on ensemble averages of intensities in Chapter V have proven useful for the determination and validation of analytical relationships between roughness and measurable parameters in RICM interferograms. However, they represent the simplest possible scenario and more sophisticated methods are desirable to quantify their accuracy, especially including scattering and finite illumination aperture effects. Surface roughness models different from the Gaussian one can be considered in the analysis of other samples of particles exhibiting asperity-like roughness. In addition, surface profiles from AFM measurements on the particles can also be incorporated using computational methods to facilitate accurate analysis of hundreds of particles via RICM fringe visibility analysis. Finally, it is recommended to extent the current range for particle size measurements, especially for smaller particles using simulations and measurements from at least another standard reference material.

REFERENCES

1 Castle, J. E. & Zhdan, P. A. Characterization of surface topography by SEM and SFM: problems and solutions. *J. Phys. D: Appl. Phys.* **30**, 722-740 (1997).

2 Haupt, B. J., Pelling, A. E. & Horton, M. A. Integrated confocal and scanning probe microscopy for biomedical research. *ScientificWorldJournal* **6**, 1609-1618 (2006).

3 Tabor, R. F. *et al.* Combined AFM-confocal microscopy of oil droplets: absolute separations and forces in nanofilms. *J. Phys. Chem. Lett.* **2**, 961-965 (2011).

4 Tabor, R. F., Grieser, F., Dagastine, R. R. & Chan, D. Y. C. Measurement and analysis of forces in bubble and droplet systems using AFM. *J. Colloid Interface Sci.* **371**, 1-14 (2012).

5 Bevan, M. A. & Eichmann, S. L. Optical microscopy measurements of kT-scale colloidal interactions. *Curr. Opin. Colloid Interface Sci.* **16**, 149-157 (2011).

6 Inoue, S. in *Handbook of biological confocal microscopy* (ed J. B. Pawley) Ch. 1, 1-19 (Springer, 2006).

7 Gaspard, J., Hahn, M. S. & Silas, J. A. Polymerization of hydrogels inside self-assembled block copolymer vesicles. *Langmuir* **25**, 12878-12884 (2009).

8 Kirk, S., Skepper, J. & Donald, A. M. Application of environmental scanning electron microscopy to determine biological surface structure. *J. Microsc.* **233**, 205-224 (2009).

9 Rykaczewski, K., Landin, T., Walker, M. L., Scott, J. H. J. & Varanasi, K. K. Direct imaging of complex nano- to microscale interfaces involving solid, liquid, and gas phases. *ACS Nano* **6**, 9326-9334 (2012).

10 Klang, V., Valenta, C. & Matsko, N. B. Electron microscopy of pharmaceutical systems. *Micron* **44**, 45-74 (2013).

11 Bibi, S. *et al.* Microscopy imaging of liposomes: from coverslips to environmental SEM. *Int. J. Pharm.* **417**, 138-150 (2011).

12 Kemper, B. & von Bally, G. Digital holographic microscopy for live cell applications and technical inspection. *Appl. Optics* **47**, A52-A61 (2008).

13 Fung, J. *et al.* Measuring translational, rotational, and vibrational dynamics in colloids with digital holographic microscopy. *Opt. Express* **19**, 8051-8065 (2011).

14 Bennett, J. M. Measurement of the rms roughness, autocovariance function and other statistical properties of optical surfaces using a FECO scanning interferometer. *Appl. Optics* **15**, 2705-2721 (1976).

15 de Ruiter, J., Oh, J. M., van den Ende, D. & Mugele, F. Dynamics of collapse of air films in drop impact. *Phys. Rev. Lett.* **108**, 074505 (2012).

16 Driscoll, M. M. & Nagel, S. R. Ultrafast interference imaging of air in splashing dynamics. *Phys. Rev. Lett.* **107**, 154502 (2011).

17 Ribbens, W. B. Interferometric surface roughness measurement. *Appl. Optics* **8**, 2173-2176 (1969).

18 Brand, U. & Hillmann, W. Calibration of step height standards for nanometrology using interference microscopy and stylus profilometry. *Precis. Eng.* **17**, 22-33 (1995).

19 Bhushan, B. *Modern tribology handbook* (CRC Press, 2010).

20 Spannagel, R., Schuldt, T. & Braxmaier, C. High resolution optical surface investigation based on heterodyne interferometry. *Int. J. Optomechatron.* **6**, 264-274 (2012).

21 Erath, J., Schmidt, S. & Fery, A. Characterization of adhesion phenomena and contact of surfaces by soft colloidal probe AFM. *Soft Matter* **6**, 1432-1437 (2010).

22 Simson, R. *et al.* Membrane bending modulus and adhesion energy of wild-type and mutant cells of Dictyostelium lacking talin or cortexillins. *Biophys. J.* **74**, 514-522 (1998).

23 Zidovska, A. & Sackmann, E. Brownian motion of nucleated cell envelopes impedes adhesion. *Phys. Rev. Lett.* **96**, 048103 (2006).

24 Albersdorfer, A., Feder, T. & Sackmann, E. Adhesion-induced domain formation by interplay of long-range repulsion and short-range attraction force: a model membrane study. *Biophys. J.* **73**, 245-257 (1997).

25 Bruinsma, R., Behrisch, A. & Sackmann, E. Adhesive switching of membranes: experiment and theory. *Phys. Rev. E* **61**, 4253-4267 (2000).

26 Cuvelier, D. & Nassoy, P. Hidden dynamics of vesicle adhesion induced by specific stickers. *Phys. Rev. Lett.* **93**, 228101 (2004).

27 Robbins, G. P. *et al.* Effects of membrane rheology on leuko-polymersome adhesion to inflammatory ligands. *Soft Matter* **7**, 769-779 (2011).

28 Selhuber, C., Blummel, J., Czerwinski, F. & Spatz, J. P. Tuning surface energies with nanopatterned substrates. *Nano Lett.* **6**, 267-270 (2006).

29 Wiegand, G., Neumaier, K. R. & Sackmann, E. Microinterferometry: three-dimensional reconstruction of surface microtopography for thin-film and wetting studies by reflection interference contrast microscopy (RICM). *Appl. Optics* **37**, 6892-6905 (1998).

30 Clack, N. G. & Groves, J. T. Many-particle tracking with nanometer resolution in three dimensions by reflection interference contrast microscopy. *Langmuir* **21**, 6430-6435 (2005).

31 Gomez, E. W., Clack, N. G., Wu, H. J. & Groves, J. T. Like-charge interactions between colloidal particles are asymmetric with respect to sign. *Soft Matter* **5**, 1931-1936 (2009).

32 Kloboucek, A., Behrisch, A., Faix, J. & Sackmann, E. Adhesion-induced receptor segregation and adhesion plaque formation: a model membrane study. *Biophys. J.* **77**, 2311-2328 (1999).

33 Sackmann, E. & Bruinsma, R. F. Cell adhesion as wetting transition? *ChemPhysChem* **3**, 262-269 (2002).

34 Sackmann, E. & Goennenwein, S. Cell adhesion as dynamic interplay of lock-and-key, generic and elastic forces. *Prog. Theor. Phys. Supp.*, 78-99 (2006).

35 Moulinet, S. & Bartolo, D. Life and death of a fakir droplet: impalement transitions on superhydrophobic surfaces. *Eur. Phys. J. E* **24**, 251-260 (2007).

36 Sundberg, M., Mansson, A. & Tagerud, S. Contact angle measurements by confocal microscopy for non-destructive microscale surface characterization. *J. Colloid Interface Sci.* **313**, 454-460 (2007).

37 Atkinson, J. T. & Lalor, M. J. The effect of surface roughness on fringe visibility in optical interferometry. *Opt. Laser Eng.* **1**, 131-146 (1980).

38 Moy, V. T., Jiao, Y., Hillmann, T., Lehmann, H. & Sano, T. Adhesion energy of receptor-mediated interaction measured by elastic deformation. *Biophys. J.* **76**, 1632-1638 (1999).

39 Liu, K. K. Deformation behaviour of soft particles: a review. *J. Phys. D Appl. Phys.* **39**, R189-R199 (2006).

40 Attili, S. & Richter, R. P. Combining colloidal probe atomic force and reflection interference contrast microscopy to study the compressive mechanics of hyaluronan brushes. *Langmuir* **28**, 3206-3216 (2012).

41 Curtis, A. S. G. Mechanism of adhesion of cells to glass: a study by interference reflection microscopy. *J. Cell Biol.* **20**, 199-215 (1964).

42 Ploem, J. S. *Mononuclear phagocytes in immunity, infection and pathology* (Blackwell Scientific, 1975).

43 Gingell, D. & Todd, I. Interference reflection microscopy: a quantitative theory for image interpretation and its application to cell-substratum separation measurement. *Biophys. J.* **26**, 507-526 (1979).

44 Gingell, D., Todd, I. & Heavens, O. S. Quantitative interference microscopy: effect of microscope aperture. *Opt. Acta* **29**, 901-908 (1982).

45 Radler, J. & Sackmann, E. Imaging optical thicknesses and separation distances of phospholipid vesicles at solid surfaces. *J. Phys. II* **3**, 727-748 (1993).

46 Theodoly, O., Huang, Z. H. & Valignat, M. P. New modeling of reflection interference contrast microscopy including polarization and numerical aperture

effects: application to nanometric distance measurements and object profile reconstruction. *Langmuir* **26**, 1940-1948 (2010).

47 Schilling, J., Sengupta, K., Goennenwein, S., Bausch, A. R. & Sackmann, E. Absolute interfacial distance measurements by dual-wavelength reflection interference contrast microscopy. *Phys. Rev. E* **69**, 021901 (2004).

48 Limozin, L. & Sengupta, K. Quantitative reflection interference contrast microscopy (RICM) in soft matter and cell adhesion. *ChemPhysChem* **10**, 2752-2768 (2009).

49 Zilker, A., Engelhardt, H. & Sackmann, E. Dynamic reflection interference contrast (RIC-) microscopy: a new method to study surface excitations of cells and to measure membrane bending elastic moduli. *J. Phys.* **48**, 2139-2151 (1987).

50 Kuhner, M. & Sackmann, E. Ultrathin hydrated dextran films grafted on glass: preparation and characterization of structural, viscous, and elastic properties by quantitative microinterferometry. *Langmuir* **12**, 4866-4876 (1996).

51 Limozin, L. & Sengupta, K. Modulation of vesicle adhesion and spreading kinetics by hyaluronan cushions. *Biophys. J.* **93**, 3300-3313 (2007).

52 Dubreuil, F., Elsner, N. & Fery, A. Elastic properties of polyelectrolyte capsules studied by atomic-force microscopy and RICM. *Eur. Phys. J. E* **12**, 215-221 (2003).

53 Ferri, J. K. *et al.* Separating membrane and surface tension contributions in Pickering droplet deformation. *Soft Matter* **4**, 2259-2266 (2008).

54 Discher, B. M. *et al.* Polymersomes: tough vesicles made from diblock copolymers. *Science* **284**, 1143-1146 (1999).

55 Discher, D. E. & Eisenberg, A. Polymer vesicles. *Science* **297**, 967-973 (2002).

56 Lin, J. J. *et al.* The effect of polymer chain length and surface density on the adhesiveness of functionalized polymersomes. *Langmuir* **20**, 5493-5500 (2004).

57 Lin, J. J., Bates, F. S., Hammer, D. A. & Silas, J. A. Adhesion of polymer vesicles. *Phys. Rev. Lett.* **95**, 026101 (2005).

58 Nam, J. & Santore, M. M. Adhesion plaque formation dynamics between polymer vesicles in the limit of highly concentrated binding sites. *Langmuir* **23**, 7216-7224 (2007).

59 Abkarian, M. & Viallat, A. Dynamics of vesicles in a wall-bounded shear flow. *Biophys. J.* **89**, 1055-1066 (2005).

60 Vezy, C., Massiera, G. & Viallat, A. Adhesion induced non-planar and asynchronous flow of a giant vesicle membrane in an external shear flow. *Soft Matter* **3**, 844-851 (2007).

61 Seifert, U. Hydrodynamic lift on bound vesicles. *Phys. Rev. Lett.* **83**, 876-879 (1999).

62 Cantat, I. & Misbah, C. Lift force and dynamical unbinding of adhering vesicles under shear flow. *Phys. Rev. Lett.* **83**, 880-883 (1999).

63 Hammer, D. A. & Discher, D. E. Synthetic cells-self-assembling polymer membranes and bioadhesive colloids. *Annu. Rev. Mater. Res.* **31**, 387-404 (2001).

64 Chang, K. C., Tees, D. F. J. & Hammer, D. A. The state diagram for cell adhesion under flow: leukocyte rolling and firm adhesion. *Proc. Natl. Acad. Sci. USA* **97**, 11262-11267 (2000).

65 Robert, P. *et al.* A novel leukocyte adhesion deficiency III variant: kindlin-3 deficiency results in integrin-and nonintegrin-related defects in different steps of leukocyte adhesion. *J. Immunol.* **186**, 5273-5283 (2011).

66 Cretel, E., Touchard, D., Bongrand, P. & Pierres, A. A new method for rapid detection of T lymphocyte decision to proliferate after encountering activating surfaces. *J. Immunol. Methods* **364**, 33-39 (2011).

67 Pierres, A. *et al.* Cell membrane alignment along adhesive surfaces: contribution of active and passive cell processes. *Biophys. J.* **84**, 2058-2070 (2003).

68 Pierres, A., Benoliel, A.-M., Touchard, D. & Bongrand, P. How cells tiptoe on adhesive surfaces before sticking. *Biophys. J.* **94**, 4114-4122 (2008).

69 Pierres, A., Monnet-Corti, V., Benoliel, A.-M. & Bongrand, P. Do membrane undulations help cells probe the world? *Trends Cell Biol.* **19**, 428-433 (2009).

70 Lam Hui, K., Wang, C., Grooman, B., Wayt, J. & Upadhyaya, A. Membrane dynamics correlate with formation of signaling clusters during cell spreading. *Biophys. J.* **102**, 1524-1533 (2012).

71 Sandi, M. J. *et al.* p8 expression controls pancreatic cancer cell migration, invasion, adhesion, and tumorigenesis. *J. Cell. Physiol.* **226**, 3442-3451 (2011).

72 Robert, P., Sengupta, K., Puech, P.-H., Bongrand, P. & Limozin, L. Tuning the formation and rupture of single ligand-receptor bonds by hyaluronan-induced repulsion. *Biophys. J.* **95**, 3999-4012 (2008).

73 Neto, C. & Craig, V. S. J. Colloid probe characterization: radius and roughness determination. *Langmuir* **17**, 2097-2099 (2001).

74 Indrieri, M., Podesta, A., Bongiorno, G., Marchesi, D. & Milani, P. Adhesive-free colloidal probes for nanoscale force measurements: production and characterization. *Rev. Sci. Instrum.* **82**, 023708 (2011).

75 Radler, J. & Sackmann, E. On the measurement of weak repulsive and frictional colloidal forces by reflection interference contrast microscopy. *Langmuir* **8**, 848-853 (1992).

76 Picart, C. *et al.* Microinterferometric study of the structure, interfacial potential, and viscoelastic properties of polyelectrolyte multilayer films on a planar substrate. *J. Phys. Chem. B* **108**, 7196-7205 (2004).

77 Nadal, F., Dazzi, A., Argoul, F. & Pouligny, B. Probing the confined dynamics of a spherical colloid close to a surface by combined optical trapping and reflection interference contrast microscopy. *Appl. Phys. Lett.* **79**, 3887-3889 (2001).

78 Heinrich, V., Wong, W. P., Halvorsen, K. & Evans, E. Imaging biomolecular interactions by fast three-dimensional tracking of laser-confined carrier particles. *Langmuir* **24**, 1194-1203 (2008).

79 Discher, B. M. *et al.* Cross-linked polymersome membranes: vesicles with broadly adjustable properties. *J. Phys. Chem. B* **106**, 2848-2854 (2002).

80 Kita-Tokarczyk, K., Grumelard, J., Haefele, T. & Meier, W. Block copolymer vesicles - using concepts from polymer chemistry to mimic biomembranes. *Polymer* **46**, 3540-3563 (2005).

81 Mecke, A., Dittrich, C. & Meier, W. Biomimetic membranes designed from amphiphilic block copolymers. *Soft Matter* **2**, 751-759 (2006).

82 Sukhorukov, G. B. *et al.* Layer-by-layer self assembly of polyelectrolytes on colloidal particles. *Colloids Surf. A* **137**, 253-266 (1998).

83 Wang, Y., Angelatos, A. S. & Caruso, F. Template synthesis of nanostructured materials via layer-by-layer assembly. *Chem. Mater.* **20**, 848-858 (2008).

84 Weisstein, E. W. *Change of variables theorem*, <http://mathworld.wolfram.com/ChangeofVariablesTheorem.html> (2010).

85 Bermudez, H., Brannan, A. K., Hammer, D. A., Bates, F. S. & Discher, D. E. Molecular weight dependence of polymersome membrane structure, elasticity, and stability. *Macromolecules* **35**, 8203-8208 (2002).

86 Mark, J. E. *Polymer data handbook* (Oxford University Press, 1999).

87 Wiegand, G., Jaworek, T., Wegner, G. & Sackmann, E. Studies of structure and local wetting properties on heterogeneous, micropatterned solid surfaces by microinterferometry. *J. Colloid Interface Sci.* **196**, 299-312 (1997).

88 Stockelhuber, K. W., Radoev, B. & Schulze, H. J. Some new observations on line tension of microscopic droplets. *Colloids Surf. A* **156**, 323-333 (1999).

89 Shull, K. R. Contact mechanics and the adhesion of soft solids. *Mater. Sci. Eng. R Rep.* **36**, 1-45 (2002).

90 Kappl, M. & Butt, H. J. The colloidal probe technique and its application to adhesion force measurements. *Part. Part. Syst. Charact.* **19**, 129-143 (2002).

91 Ziskind, G. Particle resuspension from surfaces: revisited and re-evaluated. *Rev. Chem. Eng.* **22**, 1-123 (2006).

92 Khismatullin, D. B. & Truskey, G. A. Three-dimensional numerical simulation of receptor-mediated leukocyte adhesion to surfaces: effects of cell deformability and viscoelasticity. *Phys. Fluids* **17**, 031505 (2005).

93 Hammer, D. A. *et al.* Leuko-polymersomes. *Faraday Discuss.* **139**, 129-141 (2008).

94 Kim, K. & Saleh, O. A. A high-resolution magnetic tweezer for single-molecule measurements. *Nucleic Acids Res.* **37**, e136 (2009).

95 Contreras-Naranjo, J. C., Silas, J. A. & Ugaz, V. M. Reflection interference contrast microscopy of arbitrary convex surfaces. *Appl. Optics* **49**, 3701-3712 (2010).

96 Orr, F. M., Scriven, L. E. & Rivas, A. P. Pendular rings between solids: meniscus properties and capillary force. *J. Fluid Mech.* **67**, 723-742 (1975).

97 Butt, H. J. & Kappl, M. Normal capillary forces. *Adv. Colloid Interface Sci.* **146**, 48-60 (2009).

98 Sengupta, K. & Limozin, L. Adhesion of soft membranes controlled by tension and interfacial polymers. *Phys. Rev. Lett.* **104**, 088101 (2010).

99 Wan, K. T. & Liu, K. K. Contact mechanics of a thin-walled capsule adhered onto a rigid planar substrate. *Med. Biol. Eng. Comput.* **39**, 605-608 (2001).

100 Shanahan, M. E. R. Adhesion of a liquid-filled spherical membrane. *J. Adhes.* **79**, 881-891 (2003).

101 Das, S. K., Schechter, R. S. & Sharma, M. M. The role of surface roughness and contact deformation on the hydrodynamic detachment of particles from surfaces. *J. Colloid Interface Sci.* **164**, 63-77 (1994).

102 Suresh, L. & Walz, J. Y. Direct measurement of the effect of surface roughness on the colloidal forces between a particle and flat plate. *J. Colloid Interface Sci.* **196**, 177-190 (1997).

103 Hu, S., Kim, T. H., Park, J. G. & Busnaina, A. A. Effect of different deposition mediums on the adhesion and removal of particles. *J. Electrochem. Soc.* **157**, H662-H665 (2010).

104 Schenk, M., Futing, M. & Reichelt, R. Direct visualization of the dynamic behavior of a water meniscus by scanning electron microscopy. *J. Appl. Phys.* **84**, 4880-4884 (1998).

105 Weeks, B. L., Vaughn, M. W. & DeYoreo, J. J. Direct imaging of meniscus formation in atomic force microscopy using environmental scanning electron microscopy. *Langmuir* **21**, 8096-8098 (2005).

106 Fisher, L. R. & Israelachvili, J. N. Direct experimental verification of the Kelvin equation for capillary condensation. *Nature* **277**, 548-549 (1979).

107 Christenson, H. K. Capillary condensation due to van der Waals attraction in wet slits. *Phys. Rev. Lett.* **73**, 1821-1824 (1994).

108 Kim, K. & Pack, D. W. in *BioMEMS and biomedical nanotechnology* Vol. 1 (ed Mauro Ferrari) Ch. 2, 19-50 (Springer, 2006).

109 Gong, X., Peng, S., Wen, W., Sheng, P. & Li, W. Design and fabrication of magnetically functionalized core/shell microspheres for smart drug delivery. *Adv. Funct. Mater.* **19**, 292-297 (2009).

110 Liu, X., Jin, X. & Ma, P. X. Nanofibrous hollow microspheres self-assembled from star-shaped polymers as injectable cell carriers for knee repair. *Nat. Mater.* **10**, 398-406 (2011).

111 Fan, J.-B., Huang, C., Jiang, L. & Wang, S. Nanoporous microspheres: from controllable synthesis to healthcare applications. *J. Mater. Chem. B* **1**, 2222-2235 (2013).

112 Ducker, W. A., Senden, T. J. & Pashley, R. M. Direct measurement of colloidal forces using an atomic force microscope. *Nature* **353**, 239-241 (1991).

113 van Zwol, P. J., Palasantzas, G., van de Schootbrugge, M., De Hosson, J. T. M. & Craig, V. S. J. Roughness of microspheres for force measurements. *Langmuir* **24**, 7528-7531 (2008).

114 Contreras-Naranjo, J. C. & Ugaz, V. M. A nanometre-scale resolution interference-based probe of interfacial phenomena between microscopic objects and surfaces. *Nat. Commun.* **4** (2013).

115 Chandley, P. J. Determination of the standard deviation of height on a rough surface using interference microscopy. *Opt. Quant. Electron.* **11**, 407-412 (1979).

116 Persson, B. N. J. Contact mechanics for randomly rough surfaces. *Surf. Sci. Rep.* **61**, 201-227 (2006).

117 Lu, P. & O'Shea, S. J. Mechanical contact between rough surfaces at low load. *J. Phys. D: Appl. Phys.* **45**, 475303 (2012).

118 van Zwol, P. J., Palasantzas, G. & De Hosson, J. T. M. Influence of random roughness on the Casimir force at small separations. *Phys. Rev. B* **77**, 075412 (2008).

119 Netz, R. R. Complete unbinding of fluid membranes in the presence of short-ranged forces. *Phys. Rev. E* **51**, 2286 (1995).

120 Wright, A. K. & Thompson, M. R. Hydrodynamic structure of bovine serum albumin determined by transient electric birefringence. *Biophys. J.* **15**, 137-141 (1975).

121 Caruso, F. & Möhwald, H. Protein multilayer formation on colloids through a stepwise self-assembly technique. *J. Am. Chem. Soc.* **121**, 6039-6046 (1999).

APPENDIX A
INDIRECT EVALUATION OF THE EXACT INTENSITY FORMULATION FROM THE DIRECT EVALUATION OF THE APPROXIMATED SOLUTION

In this Appendix, we describe the indirect evaluation of equations (3.4) and (3.5), exact intensity formulation, from the direct evaluation of equations (3.11) and (3.12), approximated solution; a comparison between results from these sets of equations is presented in Fig. 3.3c. The main idea is to take advantage of the backward ray-tracing method to account for all the contributions of rays $\mathbf{I_2}$, $\mathbf{I_3}$… that are reflected back from the non-planar interface, and simplify the calculations when dealing with an arbitrary convex surface. Although we focus on single-layer systems, the same procedure can be applied to situations involving multiple layers (see the double-layer system depicted in Fig. 3.6). The variables used have been defined in Fig. 3.1b and through the main text of Chapter III.

Ideally, we would like to know in advance if interference occurs at the position of interest, $B(x, y)$; in other words, if there is a range of incident angles where we expect to have $\mathbf{I_2}$ contributions that interfere with $\mathbf{I_1}$. As seen in Fig. 3.2, such angles are constrained, as in most situations, by α_{IA} and α_{DA}. The boundary corresponding to α_{IA} in Ω_2 is a function of the geometry of the reflecting surface and, in general, also a function of position at image plane. Therefore, because we are interested in arbitrary convex surfaces, it is not possible to obtain an analytical expression for the incident angle range that would be valid across all possible geometries and positions. To approximately predict the positions at image plane where interference fringes could still exist for an arbitrary convex geometry, we can use an analytical solution for the maximum inclination angle of a wedge, β_{max}, to observe interference:

$$\beta_{max} = \frac{\alpha_{DA}^{L1} + \alpha_{IA}^{L1}}{2} \tag{A1}$$

Where the superscripts L1 indicate that α_{IA} and α_{DA} are given in layer 1, and it is assumed that they are the only relevant constraints. Then, we define general integration limits for the (θ_2, ϕ_2) variables at $B(x, y)$; θ_2 goes from 0 to α_{DA} and ϕ_2 ranges from 0 to π to exploit the symmetry of the system. The upper limit of θ_2 is defined as α_{DA} taking into account that we are pursuing the

indirect calculation of the exact formulation, and beyond that limit there are no contributions from rays reflected back from the non-planar interface because they cannot reenter the microscope. However, if we want to evaluate an approximated intensity value directly from equations (3.11) and (3.12), the upper limit of θ_2 would be set to α_{TIR} given that $\mathbf{I_2}$ rays with θ_2 in between α_{DA} and α_{TIR} might be indexing single $\mathbf{I_1}$ contributions to the intensity, see Fig. 3.2. From the following paragraphs it can be seen that the exact limits for the angles where interference occurs are implicitly determined during the course of our calculations.

The integration can be performed numerically within the specified domain, noting that we only need to compute the numerators of the mentioned equations because the denominators of equations (3.4) and (3.5) can be easily determined as $2\pi(1 - \cos(\alpha_{IA}))$. In our simulations, we make calls to the functions quad and dblquad in MATLAB R2007b which use adaptive Simpson quadrature. When the integrand at a particular point (θ_2, ϕ_2) has to be calculated, the backward ray-tracing procedure is executed. For those situations where $\mathbf{I_2}$ can be traced backward to a source point *A*, as shown in Fig. 3.1b, we still need to verify that it will contribute to the intensity. The first and most important condition is that $\mathbf{I_0}$ must come from the illumination source ($\theta_1 \leq \alpha_{IA}$). If this is not satisfied, the integrand value can be set to zero and $\mathbf{I_1}$ and $\mathbf{I_2}$ are not of further interest. Provided that $\theta_1 \leq \alpha_{IA}$ we have, at least, the $\mathbf{I_1}$ contribution to the intensity and its possible interference with $\mathbf{I_2}$ depends on two additional constraints: the point *A* must be inside the field of view and the *OPLD* must be smaller than the coherence length of waves from the mercury arc lamp.

The conditions stated above can be incorporated into the calculation of the effective reflection coefficients as follows:

$$\begin{aligned} R^{s,p}(\theta_2,\phi_2) = \Theta(\alpha_{IA} - \theta_1)[&r_{01}^{s,p}(\theta_1) \\ &+ \Psi(\mathbf{A}, OPLD) t_{01}^{s,p}(\theta_1) r_{12}^{s,p}(\theta_R) t_{10}^{s,p}(\theta_2^{L1}) \\ &\times \exp(-ik\,OPLD)] \end{aligned} \tag{A2}$$

Here $\theta_2^{L1} = \sin^{-1}(n_0 \sin(\theta_2)/n_1)$ is the angle θ_2 in layer 1, according to Snell's law; r_{ij} and t_{ij} are the reflection and transmission coefficients of the interface between the layers *i* and *j*, respectively, given by the Fresnel equations and taken as a function of the angle between the incident ray and the normal to the interface (*i*, *j*); $k = 2\pi/\lambda$ is the wavenumber and λ is the wavelength of the

illuminating light; *OPLD* is given by equation (3.7); the Heaviside function Θ guarantees that the rays come from within the illumination cone; and:

$$\Psi(\mathbf{A}, OPLD) = \begin{cases} 1 & \text{if } |\mathbf{A}| < \mathbf{r}_{\text{FieldStop}} \text{ and } OPLD < 30\mu\text{m} \\ 0 & \text{otherwise} \end{cases} \tag{A3}$$

At this point we are able to evaluate the numerator of equations (3.11) and (3.12), but because our interest is the exact calculation, it is possible to write:

$$R^{s,p}(\theta_1, \phi_1) = R^{s,p}(\theta_2, \phi_2) \tag{A4}$$

In other words, the effective reflection coefficient can be indistinctly considered either as a function of (θ_2, ϕ_2) or (θ_1, ϕ_1). When we do this at every non-zero $R^{s,p}(\theta_2, \phi_2)$ point calculated while evaluating the approximated integral, we are numerically constructing the inverse map $\mathbf{G}^{-1}$, equation (3.13), for the convex geometry involved. This means that we can calculate integrand values for the numerators of equations (3.4) and (3.5) that correspond to a particular region in the Ω_1 domain with possible interference between $\mathbf{I_1}$ and $\mathbf{I_2}$ contributions (such a region is labeled as "$\mathbf{I_1}$ **&** $\mathbf{I_2}$" in Fig. 3.2).

In order to compute the desired integral, two final steps are necessary. First, if the "$\mathbf{I_1}$ **&** $\mathbf{I_2}$" region does not fill the entire Ω_1 domain, that implies that there is a region of single $\mathbf{I_1}$ contributions where the integration can be performed directly, using equations (3.4) and (3.5), provided the translation of the boundary $\theta_2 = \alpha_{\text{DA}}$ from Ω_2 into Ω_1. Second, because the integrand values in "$\mathbf{I_1}$ **&** $\mathbf{I_2}$" form a non-regular grid in the Ω_1 domain, a set of points (θ_1, ϕ_1, *Integrand*), it is necessary to find an appropriate method to complete the computation of the desired integral. 2D Delaunay triangulation performed on a set of (θ_1, ϕ_1) allows to obtain a 3D approximation of the surface *Integrand* = $F(\theta_1, \phi_1)$ with a series of flat triangles. Then, the integration can be carried out as a summation of volumes over all the triangles inside Ω_1. Figure A1 shows a typical surface of integrand values approximated by the triangulation method.

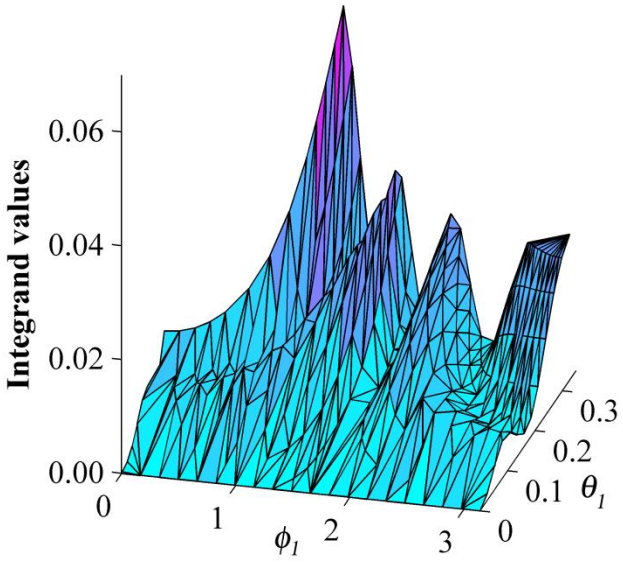

Figure A1. Typical surface of integrand values approximated by the Delaunay triangulation method.

APPENDIX B

FORMULATING NORMAL/NON-NORMAL REFLECTED LIGHT MODELS

Our approach uses the complete non-planar RICM model[95] to simulate a large variety of intensity patterns from known geometries under different conditions (that is, illumination numerical apertures (INAs), refractive indices (n_i), membrane/coating thicknesses (*L2*), etc…). Then, the geometries used (wedges and spheres) and information from their corresponding interferograms (such as fringe spacing) are analyzed to identify reasonable simplifications and key parameters that allow us to formulate a simplified non-planar RICM model while finding the most accurate and simple way to retrieve the original geometry in a wide range of possible scenarios.

Let's consider a spherical particle under different illumination conditions (Fig. B1). When looking for the appropriate simplifications, we try replacing the exact spherical geometry with a series of wedges, with one particular wedge per calculated intensity point along radial positions starting from the center of the interferogram. This is very convenient given that wedge geometries are the simplest non-planar interfaces that only involve 2D computations and similar geometric simplifications in the form of cylindrical approximations have been successfully implemented before[95]. Actually, the simulated intensity profiles from the series of wedges compare very well with the ones from the exact geometry, especially in terms of fringe spacing Δx_f (Fig. B1b,e). The fact that wedges can reproduce the illumination behavior observed in arbitrary convex geometries (as shown here for a spherical case) is a remarkable observation that gives us valuable insights: first, a full 3D description of the reflection-interference phenomenon can be simplified and, second, relatively simple geometries like wedges could provide some useful analytical expressions applicable to arbitrary convex shapes.

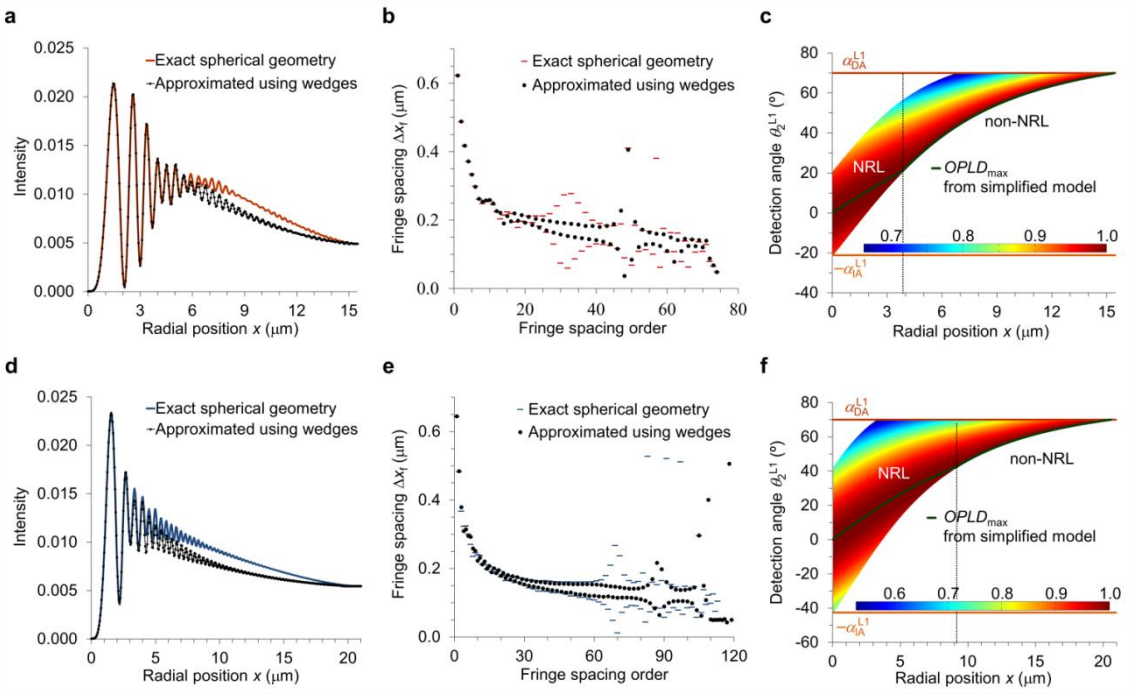

Figure B1. Approximating exact RICM spherical geometry computations with a series of wedges leads to the formulation of a simplified non-planar RICM model. (**a,d**) Exact and approximated intensity profiles simulated from a 10 μm radius sphere in water contacting a glass substrate. (**b,e**) Interferograms in (a, d) are now shown in terms of fringe spacing. (**c,f**) Normalized *OPLD* for the admissible range of detection angles at each position according to the exact spherical geometry (simplified 2D view), illustrating the applicability of the simplified non-planar RICM model to convex geometries. Simulations were performed with INA = 0.48 (top row) and 0.90 (bottom row); NA = 1.25, and glass/water/particle refractive indices of 1.53/1.33/1.55, respectively.

Therefore, we consider a simplified 2D picture for the detection angles, θ_2^{L1}, to describe and analyze the behavior of light contributing to interference (Fig. 4.4a,b and Fig. B1c,f). In this scenario, the simplest non-planar model for determining $I(x)$ is illustrated in Fig. 4.4a and formulated in equation (4.1) (derived by following Contreras-Naranjo et al.[95] for the calculation of the optical path length difference, *OPLD*). The most significant implication of this model is that $I(x)$ depends on geometric parameters ($S(x_\beta)$, β, and θ_{R}) defined at position x_β instead of x, due to the non-planar effect. Then, an analysis based on wedge systems allows establishing normal/non-normal reflected light regimes at $OPLD_{\max}$ (Fig. 4.4b and Table B1), which completes a bijective mapping between x and x_β for the direct calculation of the intensity profile ($I(x)$ versus x) when the geometry of the object ($S(x_\beta)$ versus x_β) is known.

Table B1. Analytical relationships corresponding to $OPLD_{max}$ as derived from wedge systems.

Simplified Non-planar RICM Model	
Normal Reflected Light (NRL)	Non-Normal Reflected Light (non-NRL)
$\theta_1^{L1} = \beta$	$\theta_1^{L1} = \alpha_{IA}^{L1}$
$\theta_2^{L1} = \beta$	$\theta_2^{L1} = 2\beta - \alpha_{IA}^{L1}$
$\theta_R = 0$	$\theta_R = \beta - \alpha_{IA}^{L1}$
$0 \le \beta < \alpha_{IA}^{L1}$	$\alpha_{IA}^{L1} \le \beta < \beta_{max}$

Although formulation of the simplified non-planar RICM model is based on wedge geometries, the model is expected to work well with arbitrary convex geometries for reasons previously discussed. Effectively, when these results from wedges are incorporated into a non-planar interface with varying slopes such as a sphere, Fig. B1c,f shows that they accurately follow the behavior observed for $OPLD_{max}$ in the exact geometry and successfully describe the presence of two different regimes. For that reason, the relationships presented in Fig. 4.4b and Table B1 offer a general criterion to determine when normal/non-normal reflected light approaches should be used to establish a bijective mapping between positions x and x_β when dealing with arbitrary convex geometries.

APPENDIX C
ACCURATE FRINGE SPACING ANALYSIS

Here we describe how the formulated model (Fig. 4.4a,b), despite its simplicity, can be used to obtain key relationships between a particular geometry and its corresponding intensity profile. Equation (4.3) is an important step in this direction because it shows how discrete intensity values $I(x)$ can be transformed into height values S^{P}, although S^{P} still have to be corrected to account for non-planar effects. By studying simple geometries such as wedges (Fig. C1), exact analytical expressions can be formulated which facilitates the further necessary analysis.

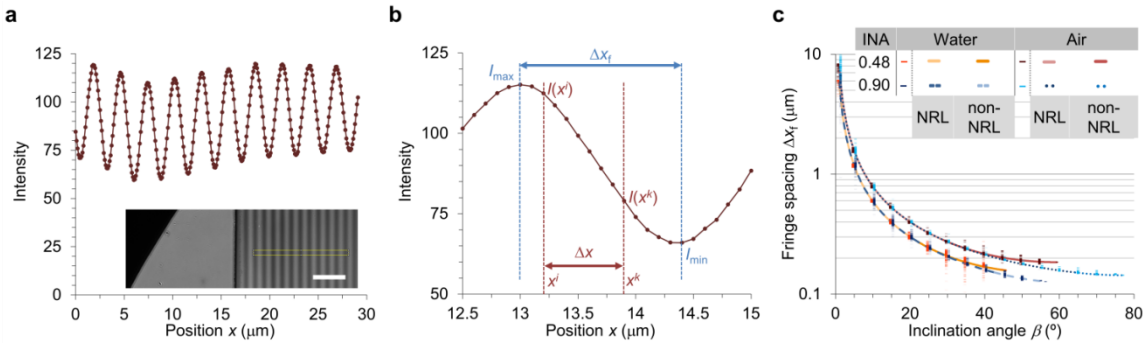

Figure C1. Wedge geometry analysis. (**a**) Intensity profile from the selected region in the RICM image (inset, 10 μm scale bar) corresponding to a wedge system; notice the fairly uniform fringe spacing. (**b**) Important parameters are identified in a particular branch of the intensity profile in (a). (**c**) It is possible to establish mappings between fringe spacing and wedge inclination angle using simulations from ensembles of wedge systems that, despite significant intrinsic variability (scattered data), follow the trends determined by equation (4.4).

Let's start with the slope definition in a wedge system β when two intensities at positions x^i and x^k are considered (see Fig. C1b).

$$\tan(\beta) = \frac{dS(x_\beta)}{dx_\beta} = \frac{S(x_\beta^k) - S(x_\beta^i)}{x_\beta^k - x_\beta^i} = \frac{\Delta S}{\Delta x_\beta} \tag{C1}$$

In contrast, from previous formulations the slope would have been expressed as $\tan(\beta) = (S^{Pk} - S^{Pi})/(x^k - x^i) = \Delta S^P/\Delta x$ [29], which is not the ratio of the appropriate height and position differentials according to the geometry under consideration. Then, equation (4.2) and equation (4.3) are used to obtain independent expressions for Δx_β and ΔS, respectively, as follows.

$$\Delta x_\beta = \Delta x - \Delta S \tan(\beta + \theta_R) \tag{C2a}$$

$$\Delta S = \left[\frac{\Delta S_f^P}{\pi} \left| \cos^{-1}\left(\frac{A - I(x^k)}{B} \right) - \cos^{-1}\left(\frac{A - I(x^i)}{B} \right) \right| \right] \frac{\cos(\beta + \theta_R)}{\cos^2(\theta_R)} = \Delta S^P \frac{\cos(\beta + \theta_R)}{\cos^2(\theta_R)} \tag{C2b}$$

Finally, equation (4.4) is obtained by substituting equations (C2) into equation (C1) and after some algebraic/trigonometric manipulation. The absolute value in equation (C2b) guaranties that the height increments are positive, as assumed in the current analysis.

A convenient parameter extracted from any interferogram is the spacing between neighboring fringes Δx_f and, as seen from simulations and experiments, this parameter is fairly constant (position independent) in wedge systems although significant variability has been observed. In fact, our simplified model and derived relationships indicate that the increment ΔS^P is constant ($\Delta S^P = \Delta S^P_f$) when consecutive intensity extrema are analyzed and, consequently, ΔS, Δx_β, and Δx_f are also constant in a wedge system. This enables the verification of equation (4.4) by constructing mappings from β to Δx_f (Fig. C1c) and from β to $\Delta S^P_f/\Delta x_f$ (Fig. 4.4c) based on simulations using the full non-planar RICM theory. Details about the construction of these mappings are given in the following paragraphs and Fig. C2.

Notice that according to equation (4.4) the relevant parameters for the mapping from β to Δx_f are λ (wavelength of light being used), n_1 (surroundings composition), and θ_R (reflected light behavior that is a function of INA for the non-NRL regime) indicating that other parameters such as n_2 (composition of the object or membrane/coating), n_3 (object's composition in double-layer systems), *L2* (membrane/coating thickness), and NA (determines β_{max}) do not affect the shape of the mapping. In order to verify this, the ensemble of conditions given in Table C1 is used to simulate hundreds of interferograms (see Fig. C2a) corresponding to different wedge systems from which single fringe spacing data (Fig. C2b-d) can be collected and analyzed.

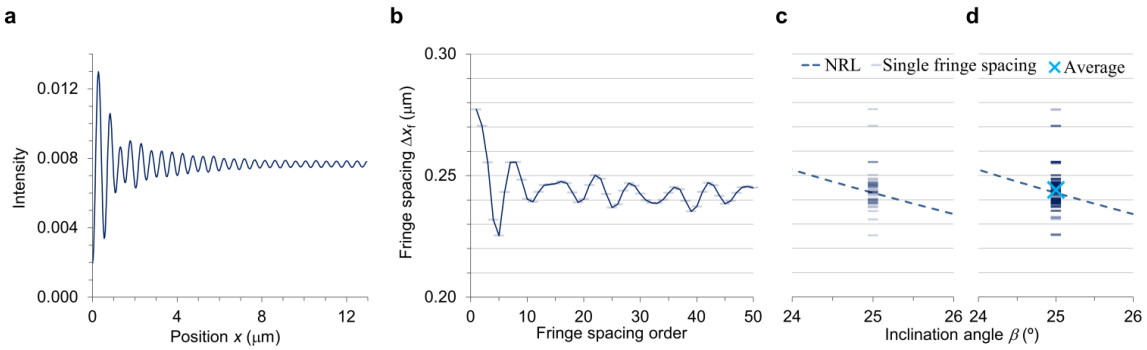

Figure C2. Detailed calculations of the wedge geometry analysis performed to validate equation (4.4). First, a series of intensity profiles from wedge geometries are simulated under different conditions; for instance, (**a**) illustrates the interferogram of the wedge system defined by: $\beta = 25^{o}$; single-layer ($L2$ = 0 nm); $n_0/n_1/n_2$ refractive indices of 1.53/1.33/1.47, respectively; INA = 0.90; and NA = 1.25. Then, up to 50 Δx_f values are extracted from each intensity profile in order to account for the variability observed. For the interferogram in (a), this is shown in (**b**) as a function of fringe spacing order and (**c**) presents the same Δx_f values (seen as scattered data) but now associated with the corresponding β. Next, all fringe spacing values from comparable wedge systems are plotted together (**d**) so that the trend observed in the mapping from β to Δx_f (including variability) can be compared with the expected mapping from equation (4.4) (NRL in (c-d)). Finally, average Δx_f values like the one in (d) are used as inputs to equation (4.4) in order to evaluate its performance when predicting inclination angles from interferograms of wedge systems.

Table C1. Ensemble of wedge systems used to verify equation (4.4)

Single-layer systems		
n_0	n_1	n_2
1.53	1.33 1.00	1.47 1.51 1.55 1.59 1.63

Double-layer systems				
n_0	n_1	n_2	n_3	$L2$ (nm)
1.53	1.33 1.00	1.45	1.55	50 100 150 200

INA = 0.48, 0.70, 0.90; NA = 1.25

When all these data are plotted together to obtain Δx_f versus β, fringe spacing values corresponding to wedge systems with the same n_1 and INA differentiate from other systems, establishing independent trends as seen in Fig. C1c, thereby verifying the mapping given by equation (4.4). Because our approach is not only limited to fringe spacing analysis, a more convenient way of expressing equation (4.4) is with the mapping from β to $\Delta S^P_f/\Delta x_f$; as demonstrated in the present work, $\Delta S^P/\Delta x$ is a measurable key parameter when studying arbitrary convex geometries.

Once equation (4.4) has been successfully verified, it is used to retrieve the original β values. Figure 4.4d illustrates that the relative error in $\beta_{retrieved}$ quickly increases beyond the midpoint of the non-NRL regime, where a cutoff angle $\beta^* = (\alpha_{IA,L1} + \beta_{max})/2$ is defined involving errors around -2%. From a practical point of view this issue is not very significant because for such relatively large inclinations the corresponding fringe spacing is very small (even comparable to pixel size) and, in addition, the visibility of those fringes is very low (being greatly affected by camera noise) so that their interference pattern easily fades away and cannot be detected. In fact, $\beta^{MaxRes} = \tan^{-1}(n_2(NA - INA)/n_1)$ provides estimation for the microscope's spatial resolution limit[45]. See Table C2 for a comparison of these parameters and errors at β^*.

Table C2. Maximum resolution and cutoff inclination angles β

β^{MaxRes} (°) | β^* (°) | error at β^* (%)					
INA	Water			Air	
0.48	33.80	33.37	-2.22	26.71	44.01	-1.11
0.70	25.55	41.32	-0.83	19.77	55.82	-1.59
0.90	16.92	49.45	-1.47	12.89	70.62	-2.58

APPENDIX D
INNOVATIVE ANALYSIS OF RICM INTENSITY PROFILES

Given that our simplified non-planar RICM model facilitates an accurate intensity analysis to retrieve inclination angles in the case of wedge geometries (Fig. 4.4), we now try to implement these ideas in the analysis of interferograms from arbitrary convex surfaces with the aim of accurately reconstructing the corresponding geometries. A first and fundamental step is the construction of the mapping from x to $\Delta S^{P}/\Delta x$ (Fig. 4.5a) by means of equation (4.4), with details of its construction presented here.

As indicated in the main text, two different but complementary transformations of the intensity data are performed to obtain $\Delta S^{P}/\Delta x$ from a given interferogram. The first transformation is based on the analysis of two consecutive intensities at positions x^{j} and x^{j+1} (located on a common branch of the intensity profile) and assuming that there is a common inclination angle β^{j} associated with them. Therefore, $\Delta x^{j} = x^{j+1} - x^{j}$ is typically a constant determined by the pixel size in the RICM image and the direction in which the intensity profile is measured. On the other hand, ΔS^{Pj} varies, as computed by means of equation (4.3), where better results are produced when using the exact ΔS^{P}_{f} calculated from the theory for stratified planar structures[29], which accounts for INA and multiple layers effects (instead of $\Delta S^{P}_{f} = \lambda/4n_1$). This approach can be applied to the complete intensity profile by performing branch-wise computations where I_{max}, I_{min}, and $\Delta S^{Pj}/\Delta x^{j}$ values are determined for each branch separately.

The second transformation is based on the analysis of two consecutive fringes at positions ${x_f}^{j}$ and ${x_f}^{j+1}$ and assuming that there is a common inclination angle β^{j} associated with them. Therefore, $\Delta x^{j} = \Delta {x_f}^{j} = {x_f}^{j+1} - {x_f}^{j}$ is roughly a constant only for wedge like geometries and it varies for arbitrary convex geometries (see Appendix B, Fig. B1b,e). On the other hand, $\Delta S^{Pj} = \Delta S^{P}_{f} = \lambda/4n_1$ is now a constant for any system and no improved ΔS^{P}_{f} calculation have proven to be necessary although INA values as high as 0.90 and double-layer systems have been considered (exactly as in the fringe spacing analysis for wedge systems). At this point, a series of $\Delta S^{Pj}/\Delta x^{j} = \Delta S^{Pj}_{f}/\Delta {x_f}^{j}$ values can be computed for all fringe spacing available.

To construct the mapping from x to $\Delta S^{P}/\Delta x$, notice that every $\Delta S^{Pj}/\Delta x^{j}$ has to be associated with a particular position, and the constructed mapping is expected to follow the

continuous $\sin(\beta)\cos(\theta_R)$ versus x function given by the geometry under consideration and the normal/non-normal reflected light regimes. This provides an important tool to determine the best way of constructing the mapping when an interferogram from a known geometry is analyzed. In Fig. D1, $\sin(\beta)\cos(\theta_R)$ versus x is determined by a known spherical geometry and it is found that $\Delta S^{Pj}/\Delta x^j$ versus $(x^j + x^{j+1})/2$, for the first transformation (from intensities), and $\Delta S^{Pj}{}_f/\Delta x_f{}^j$ versus $x_f{}^j$, for the second transformation (from fringe spacing), closely follow the expected mapping up to a point where variability is so large that it is difficult to distinguish a clear trend. An important observation is that, although variability affects both transformations, the one from fringe spacing remains closer to the expected mapping as radial position increases (especially for the larger INA value), while the transformation from intensities accurately follows the expected mapping for x values less than the position of the first fringe. In other words, our simplified model precisely predicts the intensities on the first branch of the interferogram and for subsequent branches the position of the fringes can be better predicted than the intensities, following a similar behavior described in other RICM model[46]. Therefore, a convenient method of constructing the complete mapping from x to $\Delta S^P/\Delta x$ is using the values obtained from these transformations in a complementary way, as presented in Fig. 4.5a.

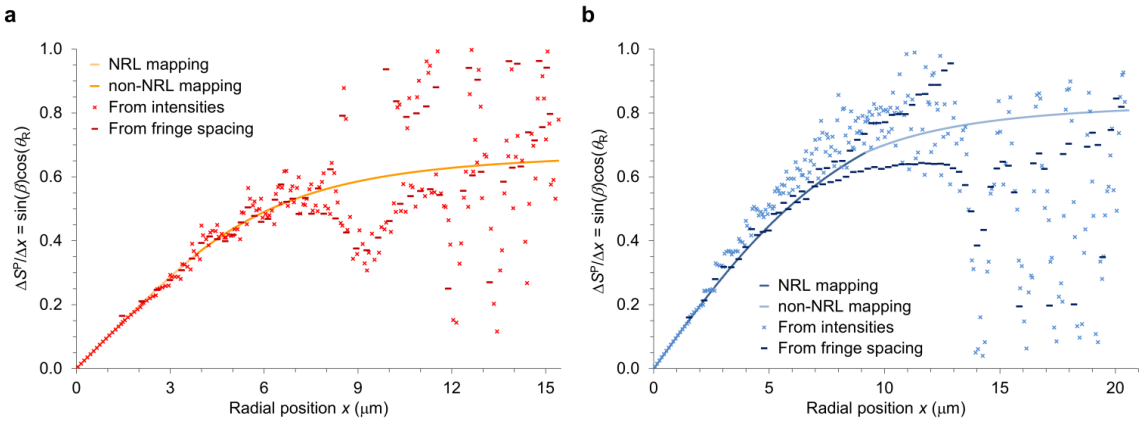

Figure D1. Construction of the mapping from x to $\Delta S^P/\Delta x$. Simulated intensity profiles corresponding to a 10 μm radius sphere in water contacting a glass substrate are analyzed by means of two different transformations (from intensities and from fringe spacing) with INA values of 0.48 (**a**) and 0.90 (**b**). Simulations were performed with NA = 1.25, and glass/water/particle refractive indices of 1.53/1.33/1.55, respectively.

A significant factor that has to be addressed is the variability observed. The main sources of variability are the noise in the intensity values (which directly affects the first transformation and also affects the accurate localization of the fringes), the assumption of a single β^j associated with a finite spacing Δx^j (especially important for the second transformation), and intrinsic variability in the fringe spacing (as seen before when analyzing wedge systems). Consequently, our approach involves the application of a smoothing procedure on the $\Delta S^P/\Delta x$ versus x discrete values; this crucial step determines the accuracy and extent of the surface profile reconstruction methods that will be described later. The smoothing is performed using a customized routine based on the *smooth* function in MATLAB and its adjustable parameters. This routine assumes that variability increases with radial position for an arbitrary convex geometry so that the smoothing parameters are adjusted accordingly as monotonically increasing smoothed data are obtained from left to right. At the end, the smoothing procedure is stopped whenever we first meet one of the following conditions: first, smoothed data reaches the maximum $\Delta S^P{}_f/\Delta x_f{}^{min} = (\sin(\alpha_{DA,L1}) + \sin(\alpha_{lA,L1}))/2$ predicted by equation (4.4) at β_{max} or second, it is no longer possible to obtain monotonically increasing smoothed data.

APPENDIX E

SURFACE PROFILE RECONSTRUCTION USING A DISCRETE APPROACH

A surface profile of any arbitrary convex geometry, $S(x_\beta)$ versus x_β, can be directly reconstructed from its interferogram by recognizing that it is possible to retrieve accurate inclination angles, β^j, from the smoothed $\Delta S^{Pj}/\Delta x^j$ values (see Fig. 4.5b), so that equations (C2) provide a series of finite height, ΔS^j, and positional, $\Delta x_\beta{}^j$, increments that describe the object's geometry.

$$\Delta x_\beta^j = x_\beta^{j+1} - x_\beta^j = \Delta x^j - \Delta S^j \tan(\beta^j + \theta_R^j) \tag{E1a}$$

$$\Delta S^j = S(x_\beta^{j+1}) - S(x_\beta^j) = \Delta S^P \frac{\cos(\beta^j + \theta_R^j)}{\cos^2(\theta_R^j)} \tag{E1b}$$

This discrete formulation of the problem, though similar to conventional surface reconstruction methods based on inverse cosine transform of intensities[45,46,49], is a significant improvement as it applies to more general situations by incorporating non-planar effects and non-normal incidence light. In fact, the contour reconstruction equations for the simplified planar model are recovered from equations (E1) in the limiting case where $\beta^j = \theta_R^j = 0$ (planar parallel interfaces and normal incidence light).

$$\Delta x_\beta^j = \Delta x^j \tag{E2a}$$

$$\Delta S^j = \Delta S^P \tag{E2b}$$

Equations (E2) indicate that the interferogram from any arbitrary convex geometry can be interpreted as being originated from a series of wedge geometries, each one corresponding to a given $\Delta S^{Pj}/\Delta x^j$ value, which implies the following geometric approximation.

$$\tan(\beta^j) = \frac{dS(x_\beta^j)}{dx_\beta^j} \approx \frac{\Delta S^j}{\Delta x_\beta^j} \tag{E3}$$

Although the case of one wedge per intensity point illustrated in Appendix B, Fig. B1, produces very good results, this geometric approximation of one wedge β^j per calculated $\Delta S^{pj}/\Delta x^j$ sounds reasonable but it is expected to have important limitations. For instance, the size of the increments can be relatively large (that is as determined by fringe spacing) when compared to object size, limiting the resolution by which the surface profile can be discretized (a critical issue for geometries with slopes that quickly change). This is better visualized in Fig. E1, where the surface profile of a spherical object is reconstructed using a discrete approach by means of equations (E1). First, the original x positions involved in the first and second transformations along with the corresponding increments and retrieved inclination angles are used to perform the contour reconstruction (labeled as "Original" resolution in Fig. E1). As expected, systematic deviations from the real contour add up after each step is performed, especially after the increments are determined by fringe spacing (at around 1.5 μm).

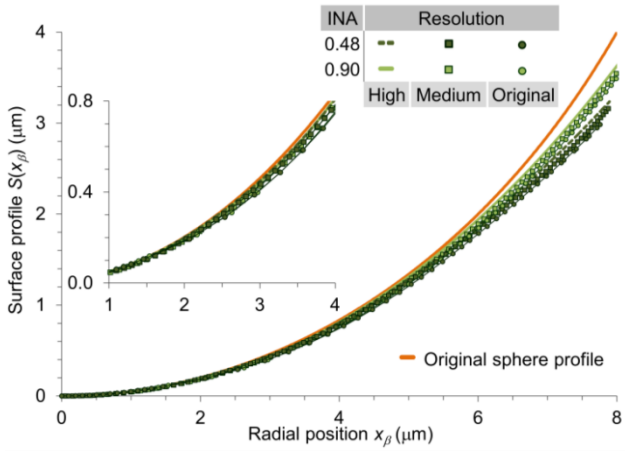

Figure E1. Surface profile reconstruction using a discrete approach. When a discrete approach to surface profile reconstruction is followed, the geometry is directly reconstructed using the information of the β versus x mapping and better results are obtained as the size of the finite increments becomes smaller (increasing resolution). Calculations correspond to a 10 μm radius sphere in water contacting a glass substrate; simulations were performed with NA = 1.25, and glass/water/particle refractive indices of 1.53/1.33/1.55, respectively.

Following this discrete approach, better resolution and accuracy can be achieved if the reconstruction procedure is not constrained by the spacing between intensities and between fringes in the interferogram. Therefore, arbitrary x values (with a constant spacing Δx, for

convenience) are defined within the range of positions determined by the mapping from x to β (Fig. 4.5b), so that interpolation can be performed to calculate their corresponding β values. Then, equation (4.4) is used to compute ΔS^{P} and equations (E1) provide the corresponding ΔS and Δx_{β} increments. Figure E1 illustrates that these simple calculations with 100 (medium resolution) and 10000 (high resolution) increments significantly improve the reconstructed surface profile when compared with the original resolution directly given by spacing in the interferogram. However, this improvement is limited (with about 10000 increments the maximum improvement is reached), indicating that a non-discrete approach must be followed to obtain even better results.

APPENDIX F

SURFACE PROFILE RECONSTRUCTION USING A CONTINUOUS APPROACH

Here the approach is based on the construction of a continuous mapping from x to β by using discrete values β^j versus x^j (Fig. 4.5b) and piecewise polynomial functions (splines). Our analysis focus on the mathematical problem of going from $\beta(x)$ to $S(x_\beta)$, which, knowing that $\tan(\beta) = dS(x_\beta)/dx_\beta$, can be achieved if the bijective mapping between x and x_β is established. The steps described in the following allow finding $x_\beta(x)$ (see Fig. F1) so that the surface profile can be reconstructed from equation (4.2). First, the geometric relationship in equation (4.2) is reorganized, for convenience all variables are considered a function of x, with $\beta + \theta_R = \theta_2^{L1}$, and the derivative with respect to x is calculated:

$$S(x_\beta(x))\tan(\theta_2^{L1}(x)) = x - x_\beta(x) \tag{F1a}$$

$$\frac{d\left[S(x_\beta(x))\right]}{dx}\tan(\theta_2^{L1}(x)) + S(x_\beta(x))\frac{d\left[\tan(\theta_2^{L1}(x))\right]}{dx} = 1 - \frac{dx_\beta(x)}{dx} \tag{F1b}$$

Then, the chain rule is applied and equation (F1a) is substituted into equation (F1b)

$$\left[\frac{dS(x_\beta(x))}{dx_\beta(x)}\frac{dx_\beta(x)}{dx}\right]\tan(\theta_2^{L1}(x)) + \left[\frac{x - x_\beta(x)}{\tan(\theta_2^{L1}(x))}\right]\frac{d\left[\tan(\theta_2^{L1}(x))\right]}{dx} = 1 - \frac{dx_\beta(x)}{dx} \tag{F1c}$$

Recognizing that $dS(x_\beta(x))/dx_\beta(x) = \tan(\beta(x_\beta(x))) = \tan(\beta(x))$ and reorganizing

$$\begin{aligned}&\left[1 + \tan(\theta_2^{L1}(x))\tan(\beta(x))\right]\frac{dx_\beta(x)}{dx} - \frac{1}{\tan(\theta_2^{L1}(x))}\frac{d\left[\tan(\theta_2^{L1}(x))\right]}{dx}x_\beta(x) \\ &= 1 - \frac{x}{\tan(\theta_2^{L1}(x))}\frac{d\left[\tan(\theta_2^{L1}(x))\right]}{dx}\end{aligned} \tag{F1d}$$

Finally, the final form of the ODE in equation (4.5) is obtained ($\theta_2^{L1}(x) = \beta(x) + \theta_R(x)$)

$$\frac{dx_\beta(x)}{dx} + \left[- \frac{\frac{d\left[\tan(\beta(x)+\theta_R(x))\right]}{dx}}{\tan(\beta(x)+\theta_R(x)) + \tan^2(\beta(x)+\theta_R(x))\tan(\beta(x))} \right] x_\beta(x) = \frac{\tan(\beta(x)+\theta_R(x)) - x\frac{d\left[\tan(\beta(x)+\theta_R(x))\right]}{dx}}{\tan(\beta(x)+\theta_R(x)) + \tan^2(\beta(x)+\theta_R(x))\tan(\beta(x))} \quad \text{(F1e)}$$

It is recommended to solve equation (4.5) in two steps: first, for the NRL regime (if any), and, second, for the non-NRL regime (if any) using the NRL result as initial condition. Also, it is important to mention that the bijective condition for the mapping between x and x_β has to be double checked once the ODE in equation (4.5) is solved and all values larger than the first (x, x_β) for which this condition is not satisfied (if any) must be excluded from the solution.

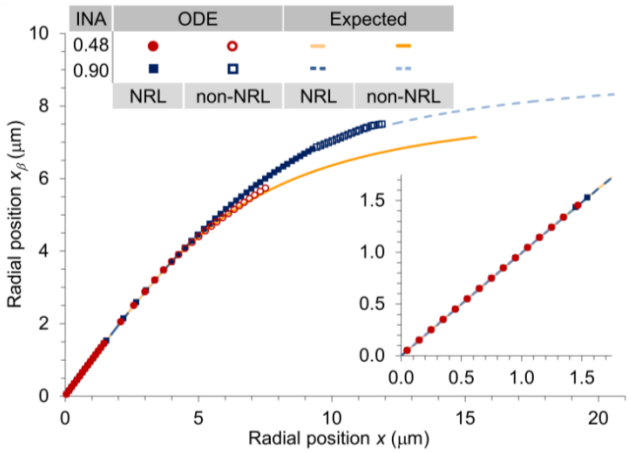

Figure F1. Surface profile reconstruction using a continuous approache. Information of the β versus x mapping is used to obtain continuous bijective mappings from x to x_β, which accurately follow the expected mappings according to the spherical geometry under consideration and the normal/non-normal reflected light regimes. Calculations correspond to a 10 μm radius sphere in water contacting a glass substrate; simulations were performed with NA = 1.25, and glass/water/particle refractive indices of 1.53/1.33/1.55, respectively.

APPENDIX G
INITIAL CONDITION IN SURFACE PROFILE RECONSTRUCTION

All methods described require the determination of an initial condition (x_β^0, $S(x_\beta^0)$) to perform the reconstruction of the surface profile. In order to account for double-layer systems, an additional phase shift of $-(\pi/\Delta S^{\mathrm{P}}_{\mathrm{f}})S^*$ [48] has to be considered in equation (4.1). Therefore, the most general formulation for this initial condition is given by equation (4.2) and a slightly modified equation (4.3).

$$S(x_\beta^0) = \frac{\cos(\beta^0 + \theta_{\mathrm{R}}^0)}{\cos^2(\theta_{\mathrm{R}}^0)}\left[S^* + \frac{l\Delta S^{\mathrm{P}}_{\mathrm{f}}}{\pi}\cos^{-1}\left(\frac{A - I(x^0)}{B} \right)\right] \tag{G1a}$$

$$x_\beta^0 = x^0 - S(x_\beta^0)\tan(\beta^0 + \theta_{\mathrm{R}}^0) \tag{G1b}$$

Here β^0 and θ_{R}^0 are the values corresponding to the first data point at position x^0 in the mapping from x to $\Delta S^{\mathrm{P}}/\Delta x$; therefore, $I(x^0)$ is either an average intensity (if x^0 lies in the middle of the first two intensities analyzed using the first transformation) or intensity extrema (if x^0 corresponds to the first intensity analyzed in terms of the second transformation); $l = 1, 2\ldots$, is the branch of the theoretical intensity versus height curve related to $I(x^0)$; $\Delta S^{\mathrm{P}}_{\mathrm{f}}$ is calculated from the theory for stratified planar structures (accounting for INA and multiple layers effects), given that it provides a valid correction in the limiting case of planar parallel interfaces which is typically a good approximation for the starting point in most applications; and A and B are calculated from the maximum and minimum intensities (typically they correspond to the closest intensity extrema). A particular situation occurs when a double-layer system is involved and $I(x^0)$ happens to be on what has been called a 0$^{\mathrm{th}}$ branch[48] ($S(x_\beta^0) < S^*$) in which case $l = -1$ in equation (G1a).

APPENDIX H
ERROR IN SURFACE PROFILES RECONSTRUCTED FROM SIMULATED INTERFEROGRAMS

Figure H1a illustrates reconstructed surface profiles using the discrete and continuous approaches described in Chapter IV and Appendix E (for INA values of 0.48 and 0.90 up to 23 and 56 fringe spacing values are analyzed, respectively, from simulated interferograms in Appendix B, Fig. B1). The error in the reconstructed profiles is obtained by comparison with the known spherical geometry originally used to simulate the intensity profiles. Figure H1b presents the absolute error as a function of the reconstructed heights, clearly indicating that the continuous approach of the ODE method produces the best results with an error that does not have a tendency to increase as height increases and, in general, is smaller than 30 nm (black dashed line). The same cannot be said about the discrete approaches where the error can grow quickly and even exponentially, as shown for the planar method when errors are larger than 100 nm (black dotted line). Notice that the discrete non-planar method, with non-planar effects included in equations (E1) and the use of arbitrary small finite increments, represents a significant improvement with respect to the conventional planar method in equations (E2). However, the improved non-planar computation still under-predicts the contour of the original geometry and only the continuous ODE approach offers an accurate solution, even for large INA values.

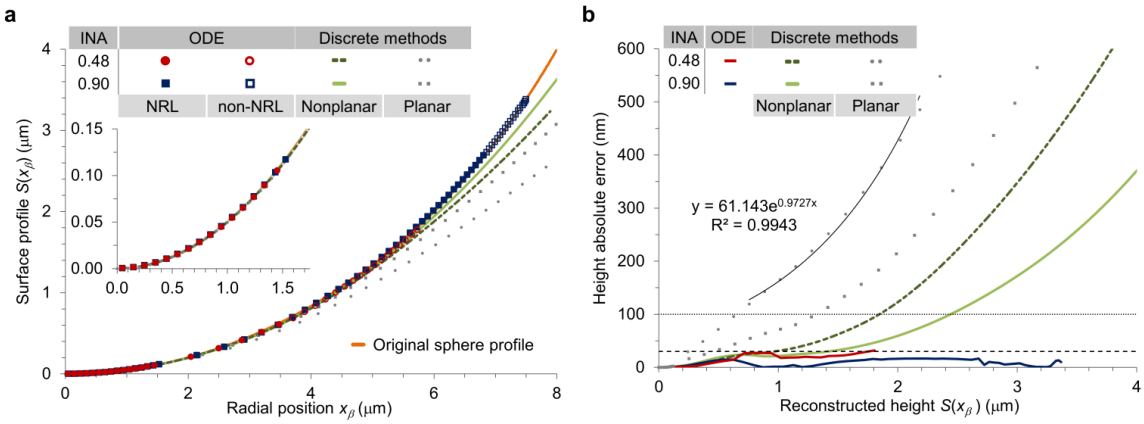

Figure H1. Analysis of the error in surface profiles reconstructed from simulated interferograms. (**a**) Surface profiles reconstructed using three methods that offer different degrees of accuracy. (**b**) Because the original spherical geometry is known, the error existent in each one of the reconstructed contours can be quantified as a function of the reconstructed height. All calculations correspond to a 10 μm radius sphere in water contacting a glass substrate. Simulations were performed with NA = 1.25, and glass/water/particle refractive indices of 1.53/1.33/1.55, respectively.

APPENDIX I

DETAILED SURFACE PROFILE RECONSTRUCTION OF SELECTED SYSTEMS

Three selected experimental systems presented in Fig. I1 (first row) are used to perform a detailed RICM analysis (including all intensities inside selections in the second row). Their reconstructed surface profiles (presented in Fig. 4.6a-c with important parameters given in Table I1) and results from simulated interferograms (presented in Appendix H) are determined using both discrete and continuous approaches. Results from discrete formulations (from Appendix E) based on equations (E1) and equations (E2) are labeled as "discrete non-planar method" (only high resolution results are presented) and "discrete planar method", respectively. When the planar model is implemented, the exact ΔS^{P}_{f} calculated from the theory for stratified planar structures is used because it is well known to improve the accuracy of the reconstructed geometries; in addition, smoothed Δx_f increments are also used. Results from the continuous formulation obtained after solving the ordinary differential equation in equation (4.5) are referred to as "ODE" and, although the results are continuous functions, they are presented as discrete values corresponding to the original data points of the mapping from x to $\Delta S^{P}/\Delta x$, which facilitates using closed/open symbols to identify where normal/non-normal reflected light (NRL/non-NRL) regimes are employed. Furthermore, by using the complete non-planar RICM image formation theory[95], a non-planar fit to the experimental data (partially shown in Fig. I1) provides a surface profile and additional information such as the position of closest proximity, $x_{\beta}^{\min}$, and the corresponding minimum separation distance, $S(x_{\beta}^{\min})$, between the object and the substrate.

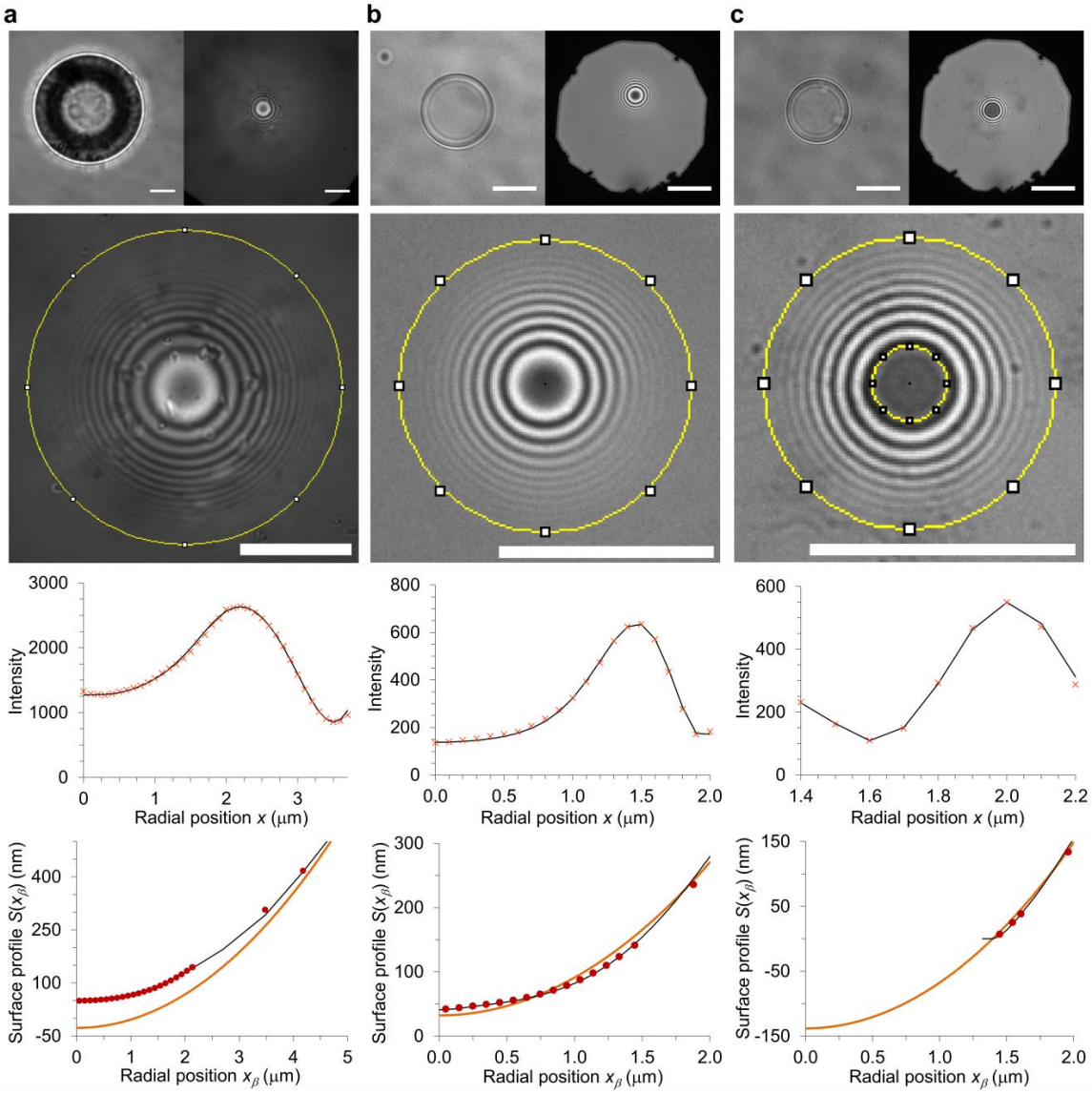

Figure I1. Experimental systems used for detailed analysis. Top row shows images (left: bright field; right: RICM) of a glass bead in air (**a**) and polymer vesicles in aqueous medium hovering next to the substrate (**b**) and in contact with the substrate (**c**). Images in the second row display the central pixel (set to black) and selections enclosing the intensities successfully considered in the surface profile reconstruction analysis (display of selections is limited by pixel resolution); notice that the inner selection approximately defines the contact area in (c). Third and fourth rows show the non-planar fit (thin black line) to experimental intensities (light red exes) corresponding to positions where the reconstructed surface profiles using the ODE method (red circles) and the non-planar fit (thin black line) diverge from spherical contours (thick orange line). 10 μm scale bars.

Table I1. Important parameters involved in the surface profile reconstruction of selected systems

Parameters	Glass bead	Polymer vesicle (hovering near substrate)	Polymer vesicle (in contact with substrate)
Construction of the mapping from x to $\Delta S^{P}/\Delta x$			
1^{st} transformation			
Δx (nm)	100	100	100
ΔS^{P}_{f} (nm)	145.2	103.8	103.8
2^{nd} transformation			
$\Delta S^{P} = \Delta S^{P}_{f} = \lambda/4n_1$ (nm)	136.5	102.3	102.3
Initial condition			
S^* (nm)	0	37.4	37.4
l	1	1	-1
x^0 (nm)	50	50	1450
β^0 (°)	0.19	1.29	9.89
$S(x_\beta{}^0)$ (nm)	49.2	41.8	6.8
$x_\beta{}^{min}$ (nm)	0	0	1400
$S(x_\beta{}^{min})$ (nm)	49	41	<1

When the ODE reconstructed contours (taken as a collection of discrete heights, each one corresponding to a $\Delta S^{P}/\Delta x$ value) for the glass bead and vesicles are analyzed in terms of spherical profiles, it is observed that an optimum spherical fit is obtained by excluding some reconstructed heights resulting from the second transformation (that is, heights corresponding to fringe spacing), in addition to excluding all previous heights from the first transformation, see Table I2. This is due to the objects' non-sphericity at their bottom, attributable to deformation in the case of the polymer vesicles, and nano-scale deviations from a perfect spherical shape in the case of the glass bead, as seen in Fig. I1. In RICM images, the effect of such nano-scale features is expected to be enhanced at the positions of closest approach between the surfaces and

smoothed out as radial position and separation increases, where light is reflected back from larger areas on the particle surface. These observations explain why it is convenient to neglect information between the center of the interferogram and one or more intensity extrema when the measurements assume that the particle is perfectly spherical down to the nanometer scale (as done here and previously[40]).

Table I2. Optimum spherical profile fit (shaded) after excluding all heights from the first transformation

Excluded heights from second transformation	S_0^{sphere} (nm)	R^{sphere} (μm)	Coefficient of determination (R^2)
Glass bead			
None	-7.4	21.278	0.9997986
1st	-15.4	21.215	0.9998640
1st to 2nd	-22.3	21.162	0.9999117
1st to 3rd	-27.2	21.125	0.9999303
1st to 4th	-28.9	21.113	0.9999236
1st to 5th	-28.1	21.119	0.9999127
Polymer vesicle (hovering near substrate)			
None	28.9	8.492	0.9998465
1st	32.2	8.513	0.9998650
1st to 2nd	34.4	8.527	0.9998543
1st to 3rd	33.6	8.522	0.9998229
Polymer vesicle (in contact with substrate)			
None	-140.6	7.106	0.9999387
1st	-138.2	7.122	0.9999501
1st to 2nd	-136.3	7.133	0.9999496
1st to 3rd	-137.1	7.129	0.9999344

APPENDIX J
ANALYTICAL TREATMENT OF ENSEMBLE AVERAGE INTENSITIES

To make the formulated model in Fig. 5.1a and equation (5.1) more suitable for practical implementation, an ensemble average approach is followed. Starting from equation (5.1), two *OPLD* terms representing the smooth, Δ^{smooth}, and the rough, Δ^{rough}, components are identified and the argument of the cosine function is denoted as *A*, for convenience:

$$I(x) = I_1 + I_2 + 2\sqrt{I_1 I_2}\cos\left(\frac{2\pi}{\lambda}\left(\left[2n_1 S(x_\beta)\frac{\cos^2(\theta_R)}{\cos(\theta_R+\beta)}\right] + \left[2n_1\left(Z(x_\beta)\cos(\theta_R)\right)\right]\right) + \delta\right) \quad \text{(J1a)}$$

$$I(x) = I_1 + I_2 + 2\sqrt{I_1 I_2}\cos\left(\frac{2\pi}{\lambda}\left(\Delta^{\text{smooth}} + \Delta^{\text{rough}}\right) + \delta\right) = I_1 + I_2 + 2\sqrt{I_1 I_2}\cos(A) \quad \text{(J1b)}$$

The cosine term is now written in terms of exponential functions,

$$I(x) = I_1 + I_2 + \sqrt{I_1 I_2}[\cos(A) + \cos(A) + i\sin(A) - i\sin(A)] \quad \text{(J1c)}$$

$$I(x) = I_1 + I_2 + \sqrt{I_1 I_2}\left[\left(\cos(A) + i\sin(A)\right) + \left(\cos(-A) + i\sin(-A)\right)\right] \quad \text{(J1d)}$$

$$I(x) = I_1 + I_2 + \sqrt{I_1 I_2}\left[e^{iA} + e^{-iA}\right] \quad \text{(J1e)}$$

A is substituted back and the summations within the exponential terms are written as products to separate Δ^{smooth} and Δ^{rough}:

$$I(x) = I_1 + I_2 + \sqrt{I_1 I_2}\left[e^{i\left(\frac{2\pi}{\lambda}(\Delta^{\text{smooth}}+\Delta^{\text{rough}})+\delta\right)} + e^{-i\left(\frac{2\pi}{\lambda}(\Delta^{\text{smooth}}+\Delta^{\text{rough}})+\delta\right)}\right] \quad \text{(J1f)}$$

$$I(x) = I_1 + I_2 + \sqrt{I_1 I_2}\left[e^{i\left(\frac{2\pi}{\lambda}(\Delta^{\text{smooth}})+\delta\right)}e^{i\left(\frac{2\pi}{\lambda}(\Delta^{\text{rough}})\right)} + e^{-i\left(\frac{2\pi}{\lambda}(\Delta^{\text{smooth}})+\delta\right)}e^{-i\left(\frac{2\pi}{\lambda}(\Delta^{\text{rough}})\right)}\right] \quad \text{(J1g)}$$

At this point, the ensemble average intensity is computed:

$$\langle I(x)\rangle = I_1 + I_2 + \sqrt{I_1 I_2}\begin{bmatrix} e^{i\left(\frac{2\pi}{\lambda}(\Delta^{\text{smooth}})+\delta\right)}\left\langle e^{i\left(\frac{2\pi}{\lambda}(\Delta^{\text{rough}})\right)}\right\rangle \\ + e^{-i\left(\frac{2\pi}{\lambda}(\Delta^{\text{smooth}})+\delta\right)}\left\langle e^{-i\left(\frac{2\pi}{\lambda}(\Delta^{\text{rough}})\right)}\right\rangle \end{bmatrix} \quad \text{(J1h)}$$

An expression for the distribution of surface heights Z is required to continue; according to the main text, a Gaussian probability density function, PDF, with mean zero and standard deviation σ is considered:

$$\text{PDF}(Z) = \frac{1}{\sigma\sqrt{2\pi}} e^{-\frac{Z^2}{2\sigma^2}} \quad \text{(J2)}$$

So the ensemble averages for the remaining terms in equation (J1h) are given by:

$$\left\langle e^{i\left(\frac{2\pi}{\lambda}(\Delta^{\text{rough}})\right)}\right\rangle = \left\langle e^{-i\left(\frac{2\pi}{\lambda}(\Delta^{\text{rough}})\right)}\right\rangle = \frac{\int_{-\infty}^{\infty} e^{\pm i\left(\frac{2\pi}{\lambda}(2n_1\cos(\theta_{\text{R}})Z)\right)}\text{PDF}(Z)dZ}{\int_{-\infty}^{\infty}\text{PDF}(Z)dZ} = e^{-2\left(\frac{2\pi}{\lambda}n_1\cos(\theta_{\text{R}})\sigma\right)^2} \quad \text{(J3)}$$

Finally, equation (5.2) is obtained by substituting the equalities in equation (J3) into equation (J1h), factorizing the exponential that contains σ and writing the remaining exponentials as the corresponding cosine function:

$$\langle I(x)\rangle = I_1 + I_2 + \sqrt{I_1 I_2}\begin{bmatrix} e^{i\left(\frac{2\pi}{\lambda}(\Delta^{\text{smooth}})+\delta\right)}e^{-2\left(\frac{2\pi}{\lambda}n_1\cos(\theta_{\text{R}})\sigma\right)^2} \\ + e^{-i\left(\frac{2\pi}{\lambda}(\Delta^{\text{smooth}})+\delta\right)}e^{-2\left(\frac{2\pi}{\lambda}n_1\cos(\theta_{\text{R}})\sigma\right)^2} \end{bmatrix} \quad \text{(J4a)}$$

$$\langle I(x)\rangle = I_1 + I_2 + \sqrt{I_1 I_2}e^{-2\left(\frac{2\pi}{\lambda}n_1\cos(\theta_{\text{R}})\sigma\right)^2}\left[e^{i\left(\frac{2\pi}{\lambda}(\Delta^{\text{smooth}})+\delta\right)} + e^{-i\left(\frac{2\pi}{\lambda}(\Delta^{\text{smooth}})+\delta\right)}\right] \quad \text{(J4b)}$$

APPENDIX K
FRINGE VISIBILITY ANALYSIS

Here we describe how to obtain information embedded in ensemble average intensities by means of fringe visibility analysis. First, the visibility is computed for an intensity profile given by equation (5.2) (that is, corresponding to a surface with roughness σ), where the maximum and minimum intensities are:

$$\langle I\rangle_{\max} = I_1 + I_2 + 2\sqrt{I_1 I_2}\, e^{-2\left(\frac{2\pi}{\lambda} n_1 \cos(\theta_R)\sigma\right)^2} \tag{K1a}$$

$$\langle I\rangle_{\min} = I_1 + I_2 - 2\sqrt{I_1 I_2}\, e^{-2\left(\frac{2\pi}{\lambda} n_1 \cos(\theta_R)\sigma\right)^2} \tag{K1b}$$

And, therefore:

$$\langle v\rangle_{\text{Rough}} = \frac{\langle I\rangle_{\max} - \langle I\rangle_{\min}}{\langle I\rangle_{\max} + \langle I\rangle_{\min}} = \frac{2\sqrt{I_1 I_2}\, e^{-2\left(\frac{2\pi}{\lambda} n_1 \cos(\theta_R)\sigma\right)^2}}{I_1 + I_2} \tag{K2}$$

By writing similar equations for a smooth surface (that is, $\sigma = 0$), an expression for $\langle v\rangle_{\text{Smooth}}$ is determined and $\langle v\rangle_{\text{Rel}} = \langle v\rangle_{\text{Rough}}/\langle v\rangle_{\text{Smooth}}$ is obtained as shown in equation (5.3).

As mentioned in the main text, a Monte Carlo approach based on intensity computations from equation (5.1) is used to verify equation (5.3). The computations performed over the surface are for the planar parallel case considering that s-polarized light cannot interfere with p-polarized light and vice versa, as follows:

$$I(x,y) = \left(I^{\text{s}}(x,y) + I^{\text{p}}(x,y)\right)/2 \tag{K3a}$$

$$I^{\text{s,p}}(x,y) = I_1^{\text{s,p}} + I_2^{\text{s,p}} + 2\sqrt{I_1^{\text{s,p}} I_2^{\text{s,p}}}\cos\left(\frac{2\pi}{\lambda}\left[2n_1\left(S_0 + Z(x,y)\right)\right] + \delta\right) \tag{K3b}$$

with $I_1^{s,p} = \left(r_{01}^{s,p}\right)^2 I_0$ and $I_2^{s,p} = \left(1 - r_{01}^{s,p}\right)^2 \left(r_{12}^{s,p}\right)^2 I_0$, where $I_0 = 1$ and the reflection coefficients are determined by the Fresnel equations and the refractive indices of the substrate, layer 1 and object, according to Fig. 5.1a:

$$r_{ij}^{s} = \frac{n_i - n_j}{n_i + n_j} \tag{K4a}$$

$$r_{ij}^{p} = \frac{n_j - n_i}{n_i + n_j} \tag{K4b}$$

The ensemble of conditions given in Table K1 is used in the Monte Carlo simulations (consequently $\delta = \pi$).

Table K1. Ensemble of conditions used to verify equation (5.3) in a single-layer system.

n_0	n_1	n_2
1.530	1.333 1.000	1.470 1.510 1.550 1.590 1.630

APPENDIX L

MICROSPHERE SIZE AND LOCAL RADIUS OF CURVATURE MEASUREMENTS

Equation (5.4) is easily obtained from geometric relationships that consider the non-planar effect of the spherical surface. From Fig. 5.1a and assuming that the object is a microsphere of radius R with a separation distance S_0^{sphere} from the substrate, we can write:

$$\cos(\beta) = \left(R + S_0^{\text{sphere}} - S\left(x_\beta\right)\right)/R \tag{L1a}$$

$$\tan(\beta + \theta_{\text{R}}) = \left(x - x_\beta\right)/S\left(x_\beta\right) \tag{L1b}$$

After combining equations (L1) to eliminate $S\left(x_\beta\right)$ and performing algebraic simplifications, equation (5.4) is obtained when $R = D/2$ is used.

For the local radius of curvature (R^{local}) determination, only normal reflected light is considered ($\theta_{\text{R}} = 0$) so equation (5.4) simplifies to:

$$x = \left(R^{\text{local}} + S_0^{\text{sphere}}\right)\tan(\beta) \tag{L2}$$

Table L1 summarizes additional parameters (to those presented in Table 5.1) related to size measurements obtained when two monodisperse samples of different types of microspheres are analyzed.

Table L1. Additional parameters relevant to size and local curvature measurements in monodisperse samples

Particle (sample size)	Smooth R^{local} (μm)	S_0^{sphere} (nm)
PSL15 (193)	16.18 ± 5.93	22.9 ± 14.7
Glass15 (122)	13.82 ± 4.91	20.9 ± 23.3